Orbital Ordering and Multiferroics

Gwilherm Nénert

University of Groningen
Zernike Institute
for Advanced Materials

Rijksuniversiteit Groningen

Orbital Ordering and Multiferroics

Proefschrift

ter verkrijging van het doctoraat in de
Wiskunde en Natuurwetenschappen
aan de Rijksuniversiteit Groningen
op gezag van de
Rector Magnificus, dr. F. Zwarts,
in het openbaar te verdedigen op
vrijdag 16 maart 2007
om 16.15 uur

door

Gwilherm Nénert

geboren op 08 September 1979
te Rennes, Frankrijk

Promotor: Prof. dr. T. T. M. Palstra

Beoordelingscommissie: Prof. dr. M. Pérez-Mato
                        Prof. dr. P. Radaelli
                        Dr. L.-P. Regnault

A mes parents...

Contents

Chapter 1

Introduction

1.1 Transition metal oxides

Transition metal oxides form a series of compounds with a uniquely wide range of electronic properties from insulator (e.g. Cr_2O_3) to metallic (e.g. TiO). Some of these properties have been known since antiquity. Other properties, especially the "high-temperature" superconductivity of mixed oxides containing copper have been discovered only recently. Serious attempts to characterize and understand the electronic structure of transition metal oxides began in the late 1930's, but as the discovery of high-temperature superconductors and magnetoresistive materials illustrate, these compounds continue to surprise us in many ways.

The chemistry and thus the electronic and physical properties of transition metal oxides can be understood only when we have a sound knowledge of their crystal chemistry. Crystal chemistry represents not only the crystal structures of the oxides, but also the nature of bonding in them. Crystal chemistry is indeed a crucial constituent of solid state chemistry and provides the basis for designing and synthesizing new materials. Transition metal oxides are by far the most fascinating class of materials when it comes to crystal chemistry. Associated with the changes in bonding, transition metal oxides show also a gamut of fascinating properties. In recent years, it has been possible to determine the structures of complex transition metal oxides by employing some of the new techniques of crystallography. Today, we can obtain detailed structures not only of oxides in single-crystal form, but also of powders employing methods of X-ray and neutron diffraction. These two techniques have become really powerful because of the availability of synchrotron X-rays and intense pulsed neutron sources [1]. The phase diagram upon doping of $La_{1-x}Sr_xMnO_3$ is a good illustration of the rich variety of properties that one can encounter while studying transition metal oxides (see figure 1.1).

We used diffraction technique through out this thesis. Synchrotron and neutron radiations were specifically of use in our study of the hexagonal rare-earth manganates and rare-earth titanates. One of the long term interest in the field of transition metal oxides has been dedicated to the study of orbital ordering (see below section 1.2 and chapter 3) in relationship or not with the presence of the colossal magnetoresistance [1, 1]. In this thesis, we bring our contribution to the study of orbital ordering in the rare-earth titanates family (see chapter 3). A very recent or rather a revival in the field of transition metal oxides has been the study of the interplay between dielectric properties and magnetic properties. This interplay has been mostly investigated in recent years in spinels [3], orthorhombic and hexagonal related perovskites [4, 5]. The study of the interplay between dielectric and magnetic properties in transition metal oxides concerns the main core of this thesis both experimentally (see chapters 4 and 5) and theoretically (see chapter 6). We describe in section 1.3 in more details the notions associated with this interplay.
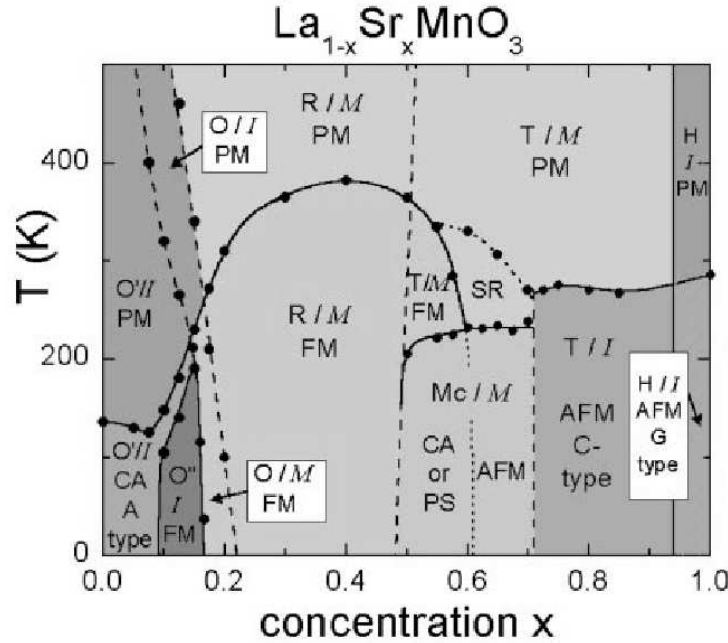
Figure 1.1: *Phase diagram of $La_{1-x}Sr_xMnO_3$ for the complete concentration regime.   The crystal structures (Jahn-Teller distorted orthorhombic: O', orthorhombic O; orbital-ordered orthorhombic: O'', rhombohedral: R, tetragonal: T, monoclinic: Mc, and hexagonal: H) are indicated as well as the magnetic structures [paramagnetic: PM, short-range order (SR), canted (CA), A-type antiferromagnetic structure: AFM, ferromagnetic: (FM), phase separated (PS), and AFM C-type structure] and the electronic state [insulating: I, metallic: M]. The phase diagram is reproduced from [6].*

1.2 Orbital Ordering: Cooperative versus dynamical Jahn-Teller effect

The theorem by Jahn-Teller was originally formulated to describe the instability of symmetric molecules in the presence of orbital electronic degeneracy [7]. They enumerated all the possible ionic (or molecular) symmetries and showed that in all cases there is at least one vibrational mode for which a splitting is allowed by symmetry. The only exception they found was the linear molecule.

The understanding of many properties of solids is based on the assumption that the motion of electrons localized in unfilled shells of ions is independent of the motion of the atomic nuclei. This is known as the Born-Oppenheimer approximation and it may be expressed algebraically as:

$$\Psi(\mathbf{q}, \mathbf{Q}) = \phi_{\mathbf{Q}}(\mathbf{q})\chi(\mathbf{Q}) \tag{1.1}$$

Here $\Psi(\mathbf{q}, \mathbf{Q})$ is the exact coupled wavefunction which is a function of the electronic coordinates $\mathbf{q}$ and the nuclear coordinates $\mathbf{Q}$. It is expressed approximately as the product of the nuclear wavefunction $\chi(\mathbf{Q})$ and the electronic wavefunction $\phi_{\mathbf{Q}}(\mathbf{q})$ which depends parametrically on $\mathbf{Q}$. $\phi_{\mathbf{Q}}(\mathbf{q})$ is an eigenfunction of the electronic hamiltonian which includes a potential energy term $V_{\mathbf{Q}}(\mathbf{q})$ [8]. The Born-Oppenheimer approximation amounts to assuming that the electronic motion is so rapid compared with the nuclear motion that this potential $V_{\mathbf{Q}}(\mathbf{q})$ is a function of $\mathbf{q}$ only and is almost independent of $\mathbf{Q}$. If there is an orbital degeneracy of the electronic states then this approximation is no longer valid. This is why the statement is often made that Jahn-Teller effects are corrections to the Born-Oppenheimer approximation. Under these circumstances it is not strictly correct to refer to the modes as electronic or lattices modes. We will use the term vibronic coupling to describe that mode which is mostly electronic in character but has some vibrational character too. In other words vibronic coupling describes the bridge between electronic and nuclear motions. The consequences of the corrections to the Born-Oppenheimer approximation can be expressed by a Jahn-Teller contribution to the hamiltonian in the form:

$$H_{JT} = A\mathbf{Q}S^z \tag{1.2}$$

where S^z is some electronic operator, which, in the case of an electronic doublet, can have the eigenvalues ± 1. The constant A measures the strength of the coupling [8].

If a crystal is formed from molecules that interact by stericlike forces, the energy of their interaction in the lattice U depends on the mutual orientation of these molecules. In such cases the minimum of the free energy F = U- TS (S is the entropy) requires at T = 0 an ordering of the interacting

molecules in which their mutual orientations make U minimal. At higher temperatures the entropy term TS becomes large, and at a certain temperature a phase transition to the disordered state for which the entropy is a maximum takes place (*order-disorder transitions*). In inorganic and coordination compounds, in addition to such order-disorder transitions, *displacive phase transitions* may take place. In them, as distinct from order-disorder transitions, the atomic arrangement in the coordination center center itself changes. Displacive transitions are related directly to the electronic structure, demonstrating the fact that in crystal stereochemistry of transition metal coordination compounds, the electronic structure of the coordination center plays a key role and cannot be ignored [9]. Thus if the different Jahn-Teller centers can interact, we will have an ordering of the local distortions which will lead to a macro-deformation of the crystal as a whole. New properties of the crystal arising from the correlation (ordering) of the Jahn-Teller center distortions, including the formation of new crystal structures and structural phase transitions, are called the *cooperative Jahn-Teller effect*. One important point is that the structural phase transition resulting from a cooperative Jahn-Teller effect is one of the most important features of the cooperative vibronic effects [9]. Many structural phase transitions in many classes of materials have been attributed to cooperative vibronic effects. In particular, in a series of tetragonal rare-earth zircons of general formula RXO_4, where R is a rare-earth (R=Tm, Dy and Tb) and X = V, As, P, a direct correspondence between electronic structure parameters of the Jahn-Teller rare-earth ion and the temperatures of structural phase transitions in the cooperative Jahn-Teller approach was established. Other crystals, such as spinel (e.g., $NiCr_2O_4$, $FeCr_2O_4$, $CuCr_2O_4$, FeV_2O_4, $FeCr_2S_4$), perovskites ($KCuF_3$, $KMnF_3$), and other structures ($CsCuCl_3$, K_2CuF_4) were also studied using the vibronic approach (see [8, 10] and references therein).

However, one question may arise from the discussion above concerning the degeneracy of the electronic states. Are the corrections to the Born-Oppenheimer approximation and the Jahn-Teller effect related to the exact degeneracy of the electronic states, or may the latter be just close in energy? In short, the answer is that electronic states with sufficiently close energy levels are similar in behavior to exact degenerate states. The case of sufficiently close energy states is called the *pseudo Jahn-Teller effect* [9]. We will not discuss further this point. We refer the reader to the literature for further details [11]. The most recent example of cooperative pseudo Jahn-Teller effect is probably the case of $LaMnO_3$ which experiences an isostructural phase transition around $T_{PJT} \simeq 750K$ [12]. In recent years, the term of orbital ordering has been preferred to the denomination of cooperative Jahn-Teller effect.

In opposition to the static pseudo Jahn-Teller and cooperative Jahn-

Teller effects, averaged effects can be observed and are called dynamic Jahn-Teller effects. Typically, a Jahn-Teller systems will exhibit at least 2 possible states below T_{JT}. However due to dynamic effects, these two states or more may be very difficult to probe. In such cases, we will observe an average. Dynamic Jahn-Teller effects can arise for a number of different reasons. The rather trivial one is thermal fluctuations. If $kT \gtrsim E_{JT}$ where E_{JT} is the energy gained by the system due to the distortion, there will be rapid, thermally induced fluctuations between the 2 states. Thus no static distortion will be observed. For other possible reasons, we refer the reader to the literature [8, 13]. These dynamical effects may bring serious difficulties in deciding whether a system is orbital ordered (static or dynamic) or not.

1.3 Multiferroic materials

Multiferroic materials can be considered as being materials presenting at least two ferroic states. These ferroic states are ferroelasticity, ferroelectricity and ferromagnetism. Thus, as a logical definition to the term multiferroic, we could use the term multiferroic to any material presenting two of these three properties. However, the most interesting combination was thought to be materials presenting ferroelectricity and ferromagnetism. Hill discussed the conditions required for ferroelectricity and ferromagnetism to be compatible in transition metal oxides, and declared them to be rarely met [14]. Thus, the current trend is that any material presenting simultaneously a polar state and a long range magnetic order is considered as a multiferroic. A recent resurgence of interested has been observed in the recent years which is driven by long-term technological applications [15].

In parallel to the work on multiferroics, a significant work has been done especially in the 1950's and 1960's on the magnetoelectric effect [16]. The magnetoelectric effect is the possibility to induce a polarization by application of a magnetic field (linear effect) or by application simultaneously of an electric and a magnetic field, for instance (non-linear effect) (see ref. [12] and chapter 2). The reverse effect is that a magnetization can be induced by an electric field (linear effect) or by application simultaneously, for instance, of an electric and a magnetic field (non-linear effect). While the non-linear effect is allowed in most of the multiferroic compounds, the ones presenting a linear effect are rather rare (see figure 1.2). Consequently, the strong interplay between dielectric and magnetic properties (linear magnetoelectric effect) is rare. For more details on the magnetoelectric effect, we refer to the recent review of Fiebig [18]. The linear magnetoelectric effect in multiferroics is important since it enhances the interplay between dielectric and magnetic properties. This interplay is of prime importance for technological applications.
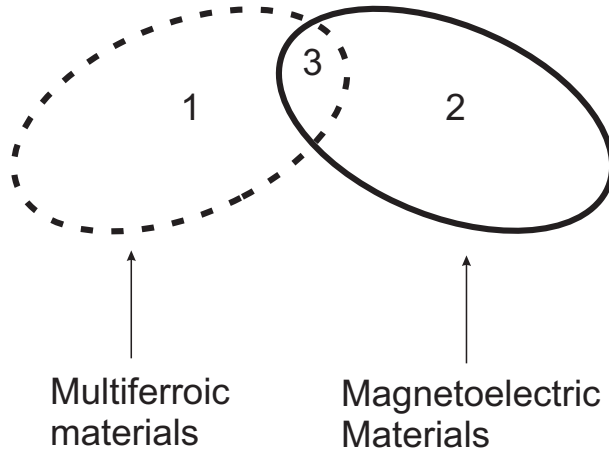
Figure 1.2: *Relationship between multiferroic and linear magnetoelectric materials. Multiferroic materials (area 1) and linear magnetoelectric materials (area 2) may overlap giving rise to an enhancement of the interplay between dielectric and magnetic properties (area 3).*

In chapter 5 of this thesis, we study the linear and non-linear magneto-electric effects in a multiferroic and non-multiferroic materials illustrating the cases of areas 2 and 3 (see figure 1.2). We show that the magnetoelectric coupling is significantly stronger in the case of area 2 than in area 1 for our studied material. In addition, we predict based on symmetry arguments the existence of new multiferroic and/or magnetoelectric materials in chapter 6.

References

[1] C. N. R. Rao and B. Raveau, Transition Metal Oxides, VCH Publishers Inc. (1995)

[2] Colossal Magnetoresistive Manganites, Edited by T. Chatterji, Kluwer Academic Publishers (2004)

[3] S. Weber *et al.*, Phys. Rev. Lett. **96**, 157202 (2006); J. Hemberger *et al.*, condmat/0608113 and references therein

[4] G. R. Blake *et al.*, Phys. Rev. B **71**, 214402 (2005); L. C. Chapon *et al.* Phys. Rev. Lett. **93**, 177402; N. Aliouane *et al.* Phys. Rev. B **73**, 20102 (2006); T. Goto *et al.* Phys. Rev. B **72**, 220403 (2005); T. Kimura *et al.*, Nature **426**, 55 (2003); N. Hur *et al.* **429**, 392 (2004)

[5] T. Lottermoser *et al.* Nature **430**, 541 (2004); M. Fiebig *et al.* Nature **419**, 818 (2002)

[6] J. Hemberger *et al.*, Phys. Rev. B **66**, 94410 (2002)

[7] H. A. Jahn and E. Teller, Proc. R. Soc. A **161**, 220 (1937)

[8] G. A. Gehring and K. A. Gehring, Co-operative Jahn-Teller effects in Reports on Progress in Physics, Vol. 38, part I, Edited by J. M. Ziman, Institute of Physics (1975).

[9] I. B. Bersuker, Electronic Structure and Properties of Transition Metal Compounds, Wiley-Interscience Publication (1996)

[10] I. B. Bersuker, The Jahn-Teller effect and Vibronic Interactions in Modern Chemistry, Plenum Press, New-York (1984); I. B. Bersuker, The Jahn-Teller effect: A Bibliographic Review, IFI/Plenum, New-York (1984); I. B. Bersuker and V. Z. Polinger, Vibronic Interactions in Molecules and Crystals, Springer-Verlag, Berlin (1989)

[11] U. Opik and M. H. L. Pryce, Proc. Roy. Soc., A**238**, 425 (1957)

[12] T. Chatterji et al. Phys. Rev. B **68**, 052406 (2003); T. Maitra, P. Thalmeier, and T. Chatterji Phys. Rev. B **69**, 132417 (2004); L. Martín-Carrón and A. de Andrés Eur. Phys. J. B **22**, 11-16 (2001).

[13] F. S. Ham, Electron Paramagnetic Resonance, edited by S. Geschwind, Plenum Press, New-York (1972)

[14] N. A. Hill, J. Phys. Chem. B **104**, 6694 (2000)

[15] W. Eerenstein, N. D. Mathur and J. F. Scott, Nature **442**, 759 (2006)

[16] A. J. Freeman, H. Schmid, Magnetoelectric interaction phenomena in crystals, London, Gordon and Breach (1975)

[17] International Tables for Crystallography, Vol. D, Physical Properties of crystals, Edited by A. Authier, Kluwer Academic Publishers, 2003

[18] M. Fiebig, J. Phys. D: Appl. Phys. **38** R123 (2005)

Chapter 2

A double approach

2.1 Experimental approach

2.1.1 Powder Diffraction versus Single crystal diffraction

Introduction

Since the discovery of diffraction, single crystal data collection has been generally used to collect integrated intensity whereas powder diffraction has been regarded as a more applied technique for phase identification and quantitative phase analysis. The development of the Rietveld method has changed this statement. Powder diffraction is nowadays a powerful tool for structure determination. Moreover, often polycrystalline samples (powders) are easier to obtain than single crystals, especially in the case of incongruent melting compounds.

Comparison

The great advantage of powder diffraction is that it does not require the growing and mounting of a single crystal. For neutron diffraction, a technique that requires larger samples than X-Ray diffraction, this is a more important consideration than for its X-ray equivalent. Powders are very much the standard for neutron diffraction, and single crystal work the exception. While powder diffraction allows better statistics, single crystal work one strongly depends on the single tiny crystal that is selected, to do all analysis. The great disadvantage of powder diffraction is that the three dimensional information of the reciprocal space of a crystal is projected into a one dimensional diffractogram. Nevertheless, powder diffraction is a widely used technique. Powder diffraction allows various in situ experiments to be carried out, and also the characterization of mixed phase samples, which is clearly impossible with single crystals. We can summarize the advantages and inconveniences of powder and single crystal diffraction in table 2.1.

Single crystal diffraction	Powder diffraction
Determination of the crystal structure with high precision and accuracy	Identification of compounds or mixtures of different compounds
Information on ordering in crystals	Investigations on homogeneity
Information on thermal motion and dynamics in crystals	Information on stress, strain and crystal size
Very precise bond lengths	Quantitative phase analysis
Imprecise for cell parameters Precise in fractional coordinates	Determination of the crystal structure (Usually not as precise as from single crystal structure analysis)

Table 2.1: *Advantages and inconveniences of powder and single crystal diffraction*

2.1.2   Single crystal growth

Introduction

The fabrication of single crystals is very important for both fundamental research and industrial purposes [1]. Single crystals can be obtained via various methods. They can be classified in three main categories: crystal growth from the melt, crystal growth from solution and chemical vapor transport. Each of these methods covers several kinds of particular techniques. However there are four main techniques used for growing transition metal oxides: flux (high temperature solution), the Bridgman method, the Czochralski method or by the "floating zone technique" (growth from the melt). All the single crystals presented in this thesis were grown by the floating zone technique.

Growth using Floating Zone Furnace

The floating zone technique is based on the zone melting principle. It is the same principle which is used also for the Bridgman and Czochralski methods. Zone melting has been developed initially for purification. Thus the Floating Zone Furnace gives rise to very pure single crystals. Moreover, as an advantage to the other zone melting method, there is no use of crucibles reducing possible contamination. In addition, a flux can be used for incongruent melting materials. While most of the optimal growth rates for metals lie between 0.5 and 15 cm/h, this value is reduced to 5 mm/h for transition metal oxides.

   The floating zone mirror furnace that we have used for the single crystal growth is presented in figure 2.1. It is a four mirror floating zone furnace from Crystal Systems Inc. with halogen lamps having a power of 1500W each.
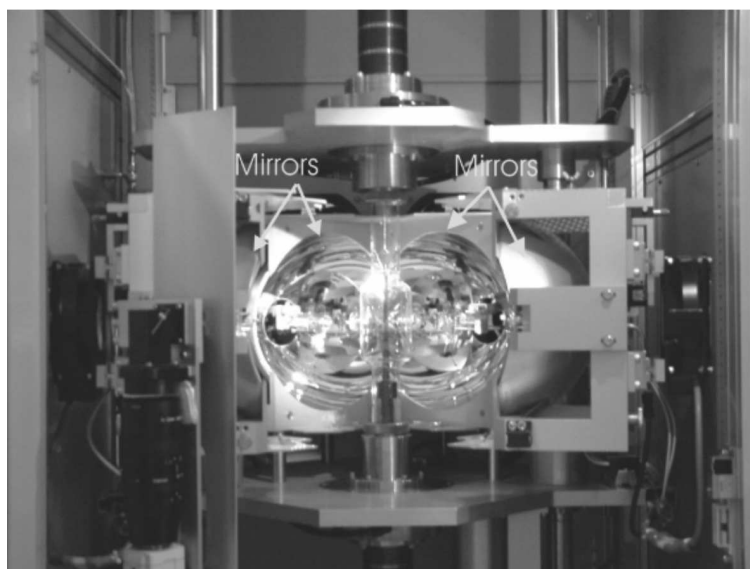
Figure 2.1: *The four mirror floating zone furnace that we used (Crystal Systems Inc., model n°FZ-T-1000-H-VI-VP).*

2.1.3 X-ray and neutron diffraction

Synchrotron versus laboratory sources for X-ray diffraction

All the standard laboratory sources used for X-ray diffraction experiments generate radiation using the same physical principles but can vary in their technical details. In our case, we have been using a Bragg-Brentano geometry using a sealed tube generator. The tube of X-rays is made from a source of electrons and a metallic cathode put in the chamber under high vacuum. The source of electrons is a filament of tungsten heated by an electric current, which expels electrons by the thermic effect. A high voltage from 40kV to 60kV is applied between the source of electrons (cathode) and the metallic anode and accelerates the electrons. Due to the way in which radiation is produced, only a discrete number of wavelengths and a broad background are available. For conventional X-ray diffraction, we have been using K_α of copper.

The generation of X-rays in a synchrotron radiation source involves a different technology. From mechanics and the Maxwell equations, it is well known that charged particles moving under the influence of an accelerating field emit electromagnetic radiation. This radiation can be used for diffraction purpose if the charged particles have a high acceleration corresponding to a speed close to the speed of light. This is realized in a synchrotron radiation facility where the charged particles (electrons or positrons) are kept circulating within an evacuated cavity on a closed path (the ring) by a num-

ber of curved magnets (the bending magnets). The different beamlines used for the different experiments are tangential to the particle trajectory. The advantage of such facility is the very bright source which is available and the possibility to tune the wavelength to the value required for a particular experiment.

Neutron diffraction

Neutron beams are produced by nuclear reactions, such as nuclear fission or fusion, or by spallation of nuclei by accelerated particles. Since for the moment nuclear fusion cannot be controlled sufficiently to produce stable neutron sources, all neutron centers use nuclear reactors (fission) and spallation sources. Spallation is the process in which a heavy nucleus emits a large number of nucleons as a result of being hit by a high-energy proton.

A number of properties of the neutron make it very useful for the study of solids. Since, neutrons are uncharged particles and of small dimensions (about 10^{-4} the size of an atom), they have a very penetrating power. The atomic scattering factors for X-rays increase throughout the periodic table (increase of the number of electrons) while it is not the case for neutrons. For neutrons, although there is a small increase of nuclear scattering factor with the mass number of the element, it is largely hidden by resonance effects which vary in a seemingly arbitrary fashion from atom to atom. As a result, the neutron scattering factors for different nuclei are in general all of the same order within a factor 4. The difference between the relative size of cross-sections (scattering factor) for X-ray and neutron is illustrated in figure 2.2.
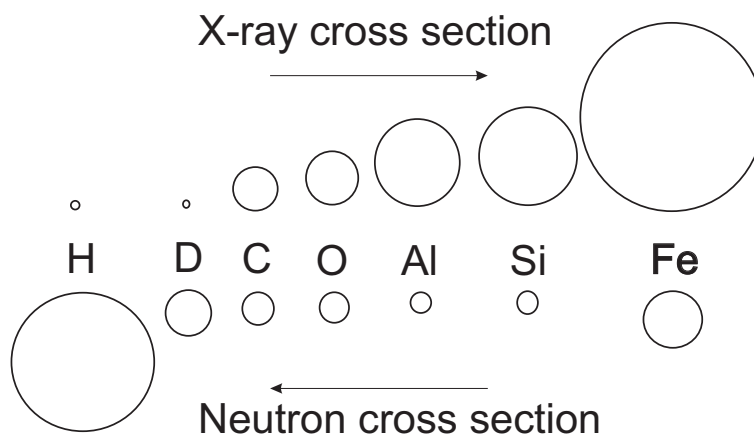
Figure 2.2: *Difference between the relative sizes of the cross-sections between X-ray and neutron for some elements.*

As a consequence, neutron diffraction is more sensitive to the light atoms like oxygen or hydrogen than X-ray diffraction. In this respect, these two

techniques are complementary. Another main difference between X-ray and neutron is related to the size of the electron cloud/nucleus. While the electron cloud has dimensions of about 1 Å, which is comparable with the X-ray wavelength, the radius of a nucleus is about 4 orders of magnitude smaller. It results that the nucleus may be considered as a point scatterer and there will be no decrease with θ of the neutron scattering factor. An additional property of the neutron is that it carries a spin and, consequently, once it interacts with the nuclei of the sample studied, it gives information about the magnetic properties.

2.1.4 Magnetometer SQUID

SQUIDs ("Superconducting Quantum Interferometer Device") enable to measure very small magnetic fields; SQUIDs are very sensitive sensors for magnetic fluxes. SQUIDs are used in the fields of electronics to biomagnetism; in addition to magnetic fluxes other physical values can be measured if they can be adapted to the magnetic flux. Attainable sensitivities of flux densities (10^{-14}T), of electrical current (10^{-12} A) and of electrical resistance ($10^{-12}\Omega$) reflect the high accuracy of a SQUID. The working principle of a SQUID is based on the quantum interference of wave functions that describe the state of the superconducting charge carriers, the so-called Cooper pairs. Each Cooper pair can be treated as a single particle with a mass and charge twice that of a single electron, whose velocity is that of the center of mass of the pair. A SQUID is based on an interferometer loop in which two weak links (Josephson contacts) are established. A weak link is realized by interrupting a superconductor by a very thin insulating barrier. The function of the SQUID is to link the quantum mechanical phase difference of the Cooper pairs wave functions over a weak link with the magnetic flux penetrating the interferometer loop.

Figure 2.3: *Scheme of a SQUID magnetometer.*

The components of a SQUID magnetometer (Fig. 2.3) typically consist of the following: a detection coil, which senses changes in the external magnetic field and transforms them into an electrical current; an input coil which transforms the resulting current into a magnetic flux in the SQUID sensor; electronics which transform the applied flux into a room temperature

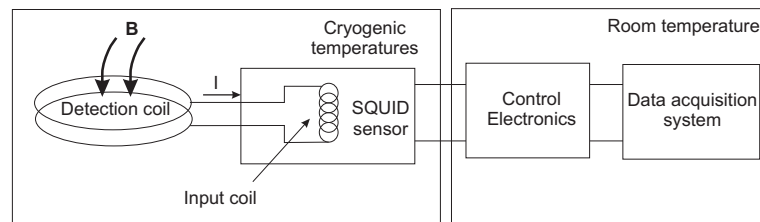voltage output; and acquisition hardware and software for acquiring, storing and analyzing data. Both the SQUID amplifier and the detection coils are superconducting devices. Thus some type of refrigerant (liquid helium or liquid nitrogen) or refrigeration device (cryocooler) is needed to maintain the SQUID and detection coil in the superconducting state. Additional signal conditioning electronics may be needed to improve signal-to-noise. We use a MPMS (Magnetic Property Measurement System based on SQUID) from Quantum Design having the following characteristics: H_{max}=7T and ΔT=1.8K-350K.

2.1.5   Dielectric Properties

Capacitance measurement

The absolute complex permittivity of a material is represented by the symbol ε, where $\varepsilon = \varepsilon^{'}$ - j$\varepsilon^{''}$ [2]. This is related to the dimensionless relative complex permittivity ε_r, where $\varepsilon_r = \varepsilon_r^{'}$ - j$\varepsilon_r^{''}$, by the expression $\varepsilon=\varepsilon_0\varepsilon_r$, ε_0 being the permittivity of free space, a fixed constant given approximately by ε_0 = 8.85×10^{-12}F.m^{-1}. In general, ε depends on temperature and, to a lesser extent, pressure. It is also frequency dependent, although $\varepsilon^{'}$ and $\varepsilon^{''}$ cannot vary independently with frequency, since their frequency variations are connected through the Kramers-Krönig relationship ($\varepsilon^{'}(\omega) = \frac{1}{\pi} \int_{-\infty}^{\infty} \frac{\varepsilon^{''}(x)}{x-\omega} dx$): a drop in $\varepsilon^{'}$ with increasing frequency is necessarily associated with a peak in $\varepsilon^{''}$. Except for exceedingly high applied fields, ε is independent of the magnitude of the applied electric field for all dielectric materials used in practice, excluding ferroelectrics.

A capacitor filled with a dielectric material has a real capacitance $\varepsilon_r^{'}$ times greater than would have a capacitor with the same electrodes in vacuum. The dielectric filled capacitor would also have a power dissipation W per unit volume at each point when, resulting from an applied voltage, a sinusoidal electric field of frequency f and root mean square value E exists at that point. This power dissipation is given by W = 2πfE$^2\varepsilon^{''}$. Thus $\varepsilon^{''}$ is a measure of the energy dissipation per period, and for this reason it is known as the loss-factor.

The complex permittivity is often represented in the Argand plane with $\varepsilon^{'}$ as abscissa and $\varepsilon^{''}$ as ordinate, giving a curve with frequency as parameter. This curve represents the complex conjugate ε^* of the complex permittivity where $\varepsilon^* = \varepsilon^{'} + $ j$\varepsilon^{''}$. The segment to the origin makes an angle δ with the abscissa, such that $\tan(\delta)$= $\varepsilon^{''}/\varepsilon^{'}$. Thus W may be rewritten as W = 2πfE$^2\varepsilon^{'}\tan(\delta)$. Hence δ is known as the loss angle, and $\tan(\delta)$ is known as the loss tangent.

Capacitance is a measure of the amount of electric charge (Q) stored (or separated) for a given electric potential (V).
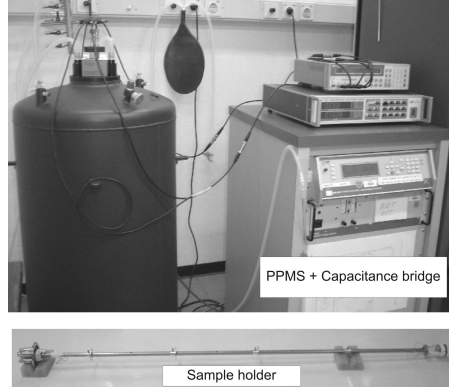
Figure 2.4: *Experimental set-up used to measure capacitance.*

$$C = \frac{Q}{V} \tag{2.1}$$

In a capacitor, there are two conducting electrodes which are insulated from one to another. The charge on the electrodes is +Q and -Q, and V represents the potential difference between the electrodes. Capacitance is measured in the SI unit of the Farad, 1F=1C/V. The capacitance can be calculated if the geometry of the conductors and the dielectric properties of the insulator between the conductors are known. For example, the capacitance of a parallel plate capacitor constructed of two parallel plane electrodes of area A separated by a distance d is approximately equal to the following:

$$C = \varepsilon \frac{A}{d} \tag{2.2}$$

where C is the capacitance in farads, ε is the permittivity of the insulator used, A is the area of each plane electrode, measured in m² and d is the separation between the electrodes, measured in m. The equation 2.2 is a good approximation if d is small compared to the other dimensions of the electrodes. This is this geometry that we have used to measure the capacitance and thus the dielectric constant of our different samples (see chapter 5). The set-up used was a home-made sample holder consisting of four stainless steel coaxial wires on a stick. This set-up was made by Umut Adem and Agung Nugroho. The measurement were carried out using programs written using the software Labview. The different programs were written by Nandang Mufti. We used two kinds of capacitance bridges. For regular measurements, we used a PPMS (Physical Properties Measurement System) of Quantum Design model 6000 (H_{max}=9T; ΔT=1.8K-350K) coupled to an Andeen-Hagerling 2500 capacitance bridge using a frequency of 1kHz. For frequency dependence, we used an Agilent 4284A (Δf=20Hz-1MHz).

Pyroelectric current measurement

The pyroelectric effect, whereby a change in temperature in a material en-
genders a release of electric charge, has been known as a physically observ-
able phenomenon for many centuries, being described by Theophrastus in
315 BC [3]. The effect occurs in any material which possesses a polar point
symmetry. Thus, of the 32 possible group symmetries, there are 10 for
which the materials possessing them are pyroelectric. These are, grouped
according to crystal system and using International notation: triclinic (1),
monoclinic (2, m), orthorhombic (2mm), tetragonal (4, 4mm), trigonal (3,
3m) and hexagonal (6, 6mm). Microscopically, the pyroelectric effect occurs
because of the asymmetric environment experienced by electrically charged
species within the crystal structure of the material. In materials the dipole
moment can arise as a consequence of the packing in an ionic crystal, be-
cause of the alignment of polarized covalent bonds in molecular crystals or
crystalline polymers or because of atomic displacements controlled by the
position of hydrogen ions in a hydrogen bonded crystal.

Quantitatively, the pyroelectric effect is described in terms of a vector,
the pyroelectric coefficient $\overrightarrow{p}$, given by the rate of change of $\overrightarrow{P}_s$ with tem-
perature (T). Thus:

$$\Delta \overrightarrow{P}_s = \overrightarrow{p} \Delta T \qquad (2.3)$$

If a thin piece of pyroelectric is electroded as shown in figure 2.5, such
that there is a component (p') of p perpendicular to the electroded surfaces
(which have area A) then these charges can be detected as a current, i_p,
flowing in an external circuit such that:

$$i_p = Ap'dT/dt \qquad (2.4)$$

Usually, the geometry is chosen such that p is oriented perpendicular to
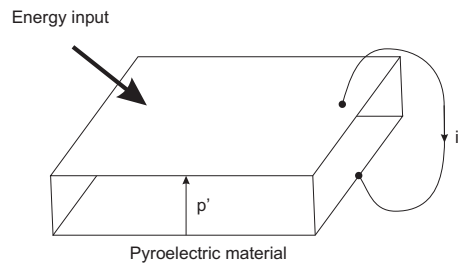the element electrodes, i.e. p=p'.

Figure 2.5: *Electroded pyroelectric element showing flow of pyroelectric current
due to change in temperature.*

While a random assembly of crystals (polycrystalline/ceramic) cannot
exhibit the polar symmetry necessary for pyroelectricity, the application of

an electrical field will re-orient the polar axes of the crystallites so that they have a component parallel to it, producing a net polarization. The size of the maximum $\overrightarrow{P}_s$ which can be achieved for a random assembly of crystallites is simply related to the possible number of polar axes in the low symmetry phase which can be derived from the high symmetry phase. Thus after poling, $\overrightarrow{P}_s$ would generally not reach the mono-domain bulk value.

From eqn 2.3 and 2.4, we can see that the determination of the polarization is done by integrating the changes of the current flowing through the material as function of temperature. This is how we effectively measure the polarization in our material (see chapter 5). For this purpose, we have used the same sample holder as previously described in figure 2.4. We measured the pyroelectric current using a electrometer Keithley 617. The poling process was done using a source unit Keithley 236 with V_{max}=1100V. The implementation for polarization measurement of the home-made set-up presented in figure 2.4 was done by Nandang Mufti.

2.2 Theoretical approach: Use of group-theory

The following section deals with symmetry arguments in the analysis of relevant materials. In the first part, we recall the main definitions, that one needs to know to do symmetry analysis. We illustrate the different definitions with the example of a group containing six elements which, as an abstract group we call $\mathbf{G}_6^2$. In one of its realizations, this group is the symmetry group of an equilateral triangle. These group theoretical methods are used in the study of orbital ordering in $RTiO_3$ (see chapter 3). Further use of these tools/notions is done in the analysis of the mechanism leading to ferroelectricity in hexagonal $RMnO_3$ (see chapter 4). After extending the notions of group theory to magnetic space groups, we treat the case of the linear magnetoelectric effect. The use of magnetic symmetry is emphasized in chapters 5 and 6. The later chapter is presented to illustrate the importance of group theory as a powerful tool to identify new materials of importance.

2.2.1 Group theoretical techniques in magnetic structure analysis

General group theory concepts

We will first introduce notations/definitions in group theory which will be used later in this chapter and more generally in this thesis [4, 5].

<u>Definition of a group:</u>

A group **G** is a set of elements together with a binary composition called a product such that:

- the product of any two elements in the group is defined and is a member of the group: if A,B $\in$ **G** then AB $\in$ **G**

- the product is associative: A(BC)=(AB)C for all A, B, C $\in$ **G**

- there exists a unique identity E in the group: EA = AE = A for all A $\in$ **G**

- every element has a unique inverse element: given A $\in$ **G** there exists a unique element A^{-1} such that $AA^{-1}=A^{-1}A = E$

From the definition of a group, it follows that a group is completely defined by its multiplication table. In fact, it is sufficient to give a set of relations involving certain elements from which the whole multiplication table can be constructed. The minimum set of elements allowing to generate the group is the set of generators. A set of generators is usually not unique. The user may choose the one which is the most handy for the purpose of a given study. In the International Tables of Crystallography [6], the crystallographic space groups are classified by their symbol. This symbol contains always a set of generators. However, sometimes it might not be the most convenient one. In the remaining part of this thesis, we will use both possibilities: the symbol or another set of generators.

E	P	P^2	Q	PQ	P^2Q
P	P^2	E	PQ	P^2Q	Q
P^2	E	P	P^2Q	Q	PQ
Q	P^2Q	PQ	E	P^2	P
PQ	Q	P^2Q	P	E	P^2
P^2Q	PQ	Q	P^2	P	E

Table 2.2: *Multiplication table of the group $\boldsymbol{G}_6^2$.*

A geometrical realization of a group is the set of symmetry operations that carry an equilateral triangle, $\triangle ABC$, into itself. If the intersection of the medians of $\triangle ABC$ is denoted O then the operation P may be thought of as the $120°$ anticlockwise rotation about a line through O perpendicular to the plane ABC and Q may be thought of as the reflection in the line AO. Equally well we could have taken P to be a $120°$ clockwise rotation and Q to be the reflection in BO or for that matter in CO. In each case we would

obtain the same group but with its elements labelled differently. This is a simple example of the non-uniqueness of a set of generators.

Now, we will give several definitions which are necessary to introduce the notions of group representations.

Homomorphism and Isomorphism

Given 2 groups $\mathbf{G}$ and $\mathbf{G}$', a mapping θ of $\mathbf{G}$ onto $\mathbf{G}$' which preserves multiplication is called a homomorphism. Thus for a homomorphism θ it follows that, for all $g_1, g_2 \in \mathbf{G}$,

$$(\theta g_1)(\theta g_2) = \theta(g_1 g_2) \tag{2.5}$$

If in addition θ is a one-to-one mapping, it is called an isomorphism: $\mathbf{G}$ and $\mathbf{G}$' are then said to be isomorphic. If θ is an isomorphism and $\mathbf{G} = \mathbf{G}$' then θ is called an automorphism.

Let $\mathbf{G} = \mathbf{G}_6^2$ and $\mathbf{G}' = \mathbf{G}_2^1$, the cyclic group of order 2 composed of elements E and P' with $P'^2 = E$ (E being the identity). Then if θ is defined so that $\theta E = E, \theta P = E, \theta P^2 = E, \theta Q = P'$, and $\theta(P^2 Q) = P'$, then θ is a homomorphism of $\mathbf{G}_6^2$ onto $\mathbf{G}_2^1$. On the other hand, if it is given that θ is a homomorphism of $\mathbf{G}_6^2$ onto $\mathbf{G}_2^1$ then, by virtue of eqn. 2.5, it is sufficient in order to define θ to specify its action only on the generators of $\mathbf{G}_6^2$.

Kernel

If $\theta\mathbf{G} = \mathbf{G}$' is a homomorphism of $\mathbf{G}$ onto $\mathbf{G}$' then the kernel of θ is the set of elements of $\mathbf{G}$ that is mapped onto the identity of $\mathbf{G}$'.

For instance the kernel of the homomorphism θ defined in the previous example between the groups $\mathbf{G} = \mathbf{G}_6^2$ and $\mathbf{G}' = \mathbf{G}_2^1$ consists of the elements E, P and P^2.

Subgroup

A subset $\mathbf{H}$ of a group $\mathbf{G}$ that is itself a group under the same binary composition as in $\mathbf{G}$ is called a subgroup of $\mathbf{G}$.

The following are subgroups of $\mathbf{G}_6^2$:

- $\mathbf{G}_6^2$ itself

- $\mathbf{G}_3^1$, consisting of E, P and P^2

- $\mathbf{G}_1^2$, consisting of E and Q

- $\mathbf{G}_1^{2'}$, consisting of E and PQ

- $\mathbf{G}_1^{2''}$, consisting of E and P^{2}Q

- $\mathbf{G}_1^1$, consisting of the identity E alone

A group has always at least two subgroups, namely the group itself and the group consisting of the identity alone. Such subgroups are called improper subgroups. Other subgroups besides these two are called proper subgroups. Thus $\mathbf{G}_6^2$ has 4 proper subgroups.

Group Representations

Now that we have given several definitions about the abstract group theory, we need to introduce the tools that we will use in the remainder of this thesis. These tools are inclosed in what we call group representations. We will continue also here by illustrating when necessary using the case of the group $\mathbf{G}_6^2$ [4, 5].

Matrix group

A matrix group Δ is a group of non-singular ($\equiv$ invertible) matrices. If all the matrices of the group are unitary then it is said to be an unitary matrix group. A unitary matrix is a n×n complex matrix U satisfying the condition UU*=U*U=E where E is the identity matrix and U* is the conjugate transpose (also called the Hermitian adjoint) of U. Note this condition says that a matrix U is unitary if and only if it has an inverse which is equal to its conjugate transpose U*. In what follows we shall be concerned with matrix groups of finite order and with matrices of finite dimension.

Two matrices D$_1$ and D$_2$ are said to be conjugate if there exists a non-singular matrix S such that D$_1$=SD$_2$S^{-1}. Two matrix groups Δ_1 and Δ_2 are said be equivalent if there exists a non-singular matrix S such that Δ_1=SΔ_2S^{-1}.

Every matrix group is equivalent to an unitary matrix group. The following symbols will be used in dealing with matrices:

- D^T for the transpose of D

- D* for the complex conjugate of D

- D† [=(D*)^T] for the Hermitean conjugate of D

- $\widetilde{D}$ [=(D^{-1})^T] for the contragredient of D

- dim D for the dimension of D

Trace-Character

The trace of a matrix D is the sum of its diagonal elements written Tr D. The character of a matrix group Δ is the function χ defined on all elements D$\in \Delta$ such that $\chi(D)$=Tr D.

Representation of a group

A representation of a group **G** is a homomorphism γ of **G** onto a group **T** of non-singular linear operators acting on a finite-dimensional vector space **V** over the complex field. We write γ**G**=**T$_\mathbf{G}$**, for all g$\in$**G**.

From this definition, it follows that when γ is a representation then:

- $T_{g_1}(T_{g_2}\mathbf{x})$=$T_{g_1 g_2}\mathbf{x}$ for all G$_1$, G$_2$ $\in$**G** and for all **x** $\in$**V**

- $T_E\mathbf{x}$=**x** for all **x**$\in$ **V**; that is, T$_E$ is the identity operator

- $T_g^{-1}\mathbf{x}$=$T_{g^{-1}}\mathbf{x}$ for all g $\in$ **G** and for all **x** $\in$ **V**

If γ is an isomorphism the representation is said to be faithful.

Suppose now that we choose a basis $<\mathbf{x}|$ consisting of linearly independent vectors $\mathbf{x}_1,\mathbf{x}_2,...,\mathbf{x}_d$ spanning the space **V**, and let us define matrices $\Gamma_\mathbf{x}$(g) by the equations

$$T_g\mathbf{x}_i = \sum_{j=1}^{d} \mathbf{x}_j\Gamma_\mathbf{x}(g)_{ij} \quad (i=1 \quad to \quad d) \tag{2.6}$$

then $\Gamma_\mathbf{x}$(g) is said to be the matrix representing G with respect to the basis $<\mathbf{x}|$ in the representation γ. The set of all distinct matrices $\Gamma_\mathbf{x}$(G) is a matrix group and it is the homomorphic image of **G** under the mapping G$\longrightarrow \Gamma_\mathbf{x}$(G), the kernel of the homomorphism being the elements of **G** mapped onto the unit matrix.

Let **G** be the group **G**$_6^2$, the multiplication table of which is given in table 2.2. A geometrical realization of this group was described in the previous illustration. This involved an equilateral triable ABC with centroid O. Let $\overrightarrow{OA}=\overrightarrow{a}$, $\overrightarrow{OB}=\overrightarrow{b}$ and $\overrightarrow{OC}=\overrightarrow{c}$; then $\overrightarrow{a}+\overrightarrow{b}+\overrightarrow{c}=\overrightarrow{0}$, and the plane of the triangle forms a vector space **V** of dimension 2. This, we take to be the underlying vector space of the representation γ. Take as basis for this vector space $\overrightarrow{x}_1 = \overrightarrow{b}$ and $\overrightarrow{x}_2=\overrightarrow{c}$. The representation γ maps P and Q onto elements T$_P$ and T$_Q$ which are respectively an anti-clockwise rotation of 120° about O and a reflection in the line AO. The operators T$_P$ and T$_Q$

are operators acting on $\mathbf{V}$ and from their definition $\mathrm{T}_P \overrightarrow{b} = \overrightarrow{c}$, $\mathrm{T}_P \overrightarrow{c} = \overrightarrow{a} = -\overrightarrow{b} - \overrightarrow{c}$, $\mathrm{T}_Q \overrightarrow{b} = \overrightarrow{c}$ and $\mathrm{T}_Q \overrightarrow{c} = \overrightarrow{b}$. From eqn. 2.6 it follows that

$$\mathbf{\Gamma_x(P)} = \begin{pmatrix} 0 & -1 \\ 1 & -1 \end{pmatrix} \quad and \quad \mathbf{\Gamma_x(Q)} = \begin{pmatrix} 0 & 1 \\ 1 & 0 \end{pmatrix} \qquad (2.7)$$

Since γ is a homomorphism the rest of the matrix group follows from multiplication. Thus, for example,

$$\mathbf{\Gamma_x(P^2)} = \mathbf{\Gamma_x(P)}\mathbf{\Gamma_x(P)} = \begin{pmatrix} -1 & 1 \\ -1 & 0 \end{pmatrix} \qquad (2.8)$$

and so on. It can easily be checked that γ is a faithful representation. However it contains non-unitary matrices. γ is of dimension 2. Thus if χ_γ is the character of γ it follows that $\chi_\gamma(\mathrm{E})=2$, $\chi_\gamma(\mathrm{P})=\chi_\gamma(\mathrm{P^2})=-1$ and $\chi_\gamma(\mathrm{Q})=\chi_\gamma(\mathrm{PQ})=\chi_\gamma(\mathrm{P^2Q})=0$.

Let $< \mathbf{x}|$ and $< \mathbf{y}|$ be two bases of $\mathbf{V}$ defined so that

$$\mathbf{y}_k = \sum_{i=1}^{d} \mathbf{x}_i S_{ik} \quad (k = 1 \quad to \quad d) \qquad (2.9)$$

where S is non-singular, then

$$\mathbf{\Gamma_y(G)} = S^{-1}\mathbf{\Gamma_x(G)}S \quad for \quad all \quad G \quad \in \quad \mathbf{G}. \qquad (2.10)$$

That is to say, a change of basis leads to matrix groups $\mathbf{\Gamma_x}(G)$ and $\mathbf{\Gamma_y}(G)$, which are equivalent. Hence, it is possible to choose a basis $< \mathbf{z}|$ in $\mathbf{V}$ such that $\mathbf{\Gamma_z}(G)$ is a unitary matrix group.

Irreducible Representation

Let γ be a representation of $\mathbf{G}$ so that $\mathbf{T}=\gamma\mathbf{G}$ is a group of non-singular linear operators acting on a vector space $\mathbf{V}$. $\mathbf{U}$ is said to be an invariant subspace of $\mathbf{V}$ under $\mathbf{T}$ if

- $\mathbf{U}$ is a vector subspace of $\mathbf{V}$

- $\mathrm{T}_G\mathbf{x} \in \mathbf{U}$ for all $\mathbf{T}_G \in \mathbf{T}$ and all $\mathbf{x} \in \mathbf{U}$

If $\mathbf{V}$ has no proper invariant subspace under $\mathbf{T}$ (that is, no subspace invariant under $\mathbf{T}$ except $\mathbf{V}$ itself and the zero-vector) then γ is said to be an irreducible representation. If there exists a proper invariant subspace under $\mathbf{T}$ than γ is said to be reducible. If $\mathbf{V}$ can be split up into the direct sum of subspaces each of which is invariant under $\mathbf{T}$ and each of which is the carrier space for an irreducible representation of $\mathbf{G}$ then γ is said to be completely reducible.

There are a number of properties for irreducibility which are useful. In many quantum mechanical applications each irreducible representation will display the transformations properties of a set of degenerate eigenfunctions. Thus, they are preferable than the reducible representations. A representation is irreducible if, and only if, the only matrices which commute with all matrices of the representation are scalar multiples of the unit matrix. Moreover, let $\mathbf{G}$ be a group of order $|\mathbf{G}|$ with elements g_1, g_2,...,$g_{|\mathbf{G}|}$. Then $\Gamma(\mathbf{G})$ is an irreducible representation if and only if

$$\frac{1}{|\mathbf{G}|} \sum_{i=1}^{|g|} |\chi_\gamma(G_i)|^2 = 1 \tag{2.11}$$

Another important result from the above properties is the decomposition of a representation in irreducible representations. Let Γ be an arbitrary matrix representation of $\mathbf{G}$ with character χ then when Γ has been completely reduced by suitable equivalence transformations to block-diagonal form it becomes a direct sum of irreducible representations $\sum_{i=1}^r c_i\Gamma^i$, where

$$c_i = \frac{1}{|\mathbf{G}|} \sum_{i=1}^{r} r_i\chi(C_i)\chi^{i*}(C_i) \tag{2.12}$$

Subduced representations:

We shall give here the definition of a subduced representation. It is of prime importance in the study of a phase transition. It is on this principle that we have based part of our analysis for hexagonal $RMnO_3$ (see chapter 4).

Let Γ be an irreducible representation of $\mathbf{G}$, character $\chi^\Gamma(g)$; then the number of times that Γ appears in the decomposition of $\Gamma^j \uparrow \mathbf{G}$ into irreducible representations of $\mathbf{G}$ is equal to the number of times the irreducible representation Γ^j appears in $\Gamma \downarrow \mathbf{H}$, where $\mathbf{H}$ is a subgroup of $\mathbf{G}$. Here $\Gamma \downarrow \mathbf{H}$ denotes the restriction of Γ to elements of $\mathbf{H}$ and is commonly called the representation of $\mathbf{H}$ subduced by Γ; since $\mathbf{H}$ is a subgroup of $\mathbf{G}$ it is clear that $\Gamma \downarrow \mathbf{H}$ is a representation of $\mathbf{H}$ of the same dimension as Γ. $\Gamma^j \uparrow \mathbf{G}$ is called the induced representation of Γ^j in $\mathbf{G}$.

Magnetic symmetries

Antielements: Polar versus Axial vectors

We discuss in this part the main features of the representation analysis of magnetic structures [5]. We should keep in mind that the spins are axial vectors or pseudovectors. This means that they transform like a (polar) vector under rotations but are invariant under spatial inversion. This is not

the case for polar vectors (e.g. the polarization) which are not invariant under spatial inversion. The mathematical expression of the time inversion operator is defined by $R^2 = E$, where E is the identity operator. The difference between a spin (axial vector) and a polarization for instance (polar vector) is that a symmetry element acts on the current loop which generates the spin. We illustrate this statement in figure 2.6 where we look at the action of an inversion center on a current loop.
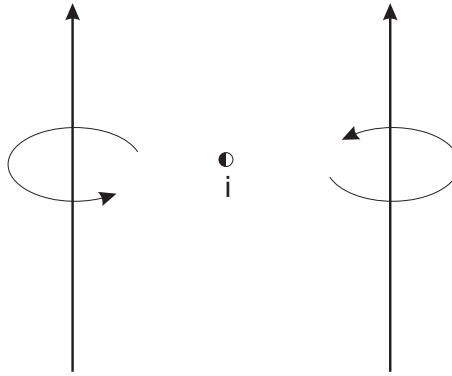

Figure 2.6: *Effect of the inversion center i on a current loop generating a spin*

We can see that contrary to a polar vector (e.g. polarization), the direction of the spin is not reversed under the inversion center. In figure 2.6, we see that we have a ferromagnetic coupling between the two spins. Consequently, for an antiferromagnetic coupling the inversion center will be broken. In order to describe properly the special properties of the spins, we need to define new symmetry elements. Historically, they have been introduced as new symmetry operators (so-called antielements) which are the product of the conventional symmetry elements g with the time inversion operator R. These new operators are denoted with a prime with respect to the conventional operators.

$$g' = gR = Rg \quad with \quad R^2 = E \tag{2.13}$$

These new symmetry elements enlarge the number of possible groups from the conventional 230 space groups from the International Tables of Crystallography [6]. Indeed, there are 32 crystalline classes which yield to 90 magnetic classes including the paramagnetic ones (which are in fact the above 32). These 90 magnetic classes give rise to 1651 magnetic space groups. These 1651 magnetic space groups contain also the paramagnetic space groups, which are the known 230 space groups from the International Tables of Crystallography [6]. They will be usually denoted e.g. *P*nma1' for the paramagnetic phase of a compound crystallizing in the space group *P*nma.

The magnetic symmetry of a crystal coincides with the group of symmetry operations which leave invariant the mean density of electric current invariant. This group can be obtained by combining the rotations, reflections and translations forming the crystallographic group **G** of the crystal, with the time-reversal operator R. They are mainly 3 kinds of magnetic groups:

- "Black and white" magnetic groups **M** resulting from the combination of R with half of the symmetry operations of the ordinary point group **G**. Such groups can be written:
  M=**H**+(**G**-**H**)R

- "White" groups which also describe a magnetic structure:
  M=**G**

- "Grey groups" labelled **G**1$'$ which contain the operations of **G** plus their combination with R:
  M=**G**+R**G**

We note that RE=R is by itself a symmetry operation of the group **G**$'$. Thus, these groups describe a paramagnetic structure. Black and White groups and also White groups describe either an antiferromagnetic or ferromagnetic structures.

Star and little group G$_{\overrightarrow{k}}$ of $\overrightarrow{k}$

In most of the transitions between a high temperature phase **G** and a low temperature phase **H**, one of the modes of **G** will become soft (its frequency goes to zero at T$_C$). This mode is characterized by a wave-vector $\overrightarrow{k}$. One can define the little-group of $\overrightarrow{k}$ denoted **G**$_{\overrightarrow{k}}$. The little-group of **G**$_{\overrightarrow{k}}$ is the set of symmetry elements which leave invariant the wave-vector $\overrightarrow{k}$. If g is a symmetry element of **G**, $\overrightarrow{k}$ is said to be invariant by g if g$\overrightarrow{k}$ - $\overrightarrow{k}$ = 0 or $\overrightarrow{n}$, $\overrightarrow{n}$ being a translation of the lattice.

One can define the star of $\overrightarrow{k}$. It is the set of inequivalent vectors $\overrightarrow{k}$ which are generated by the application of all the elements g of **G**. Each $\overrightarrow{k}$ is an arm of the star. The number of arms in the star of $\overrightarrow{k}$ is equal to the index of the subgroup **G**$_{\overrightarrow{k}}$ with respect to the group **G**.

Axial and permutation representations

The effect of symmetry element is two-fold: it will act to change the position of an atom, and reorientate the magnetic moment, e.g. atom 1 moves to the position of atom 2, and its moment is reversed. The combination of

these two results are described by the magnetic representation, Γ. We will examine these two effects separately.

A symmetry operator g=$\{h|\tau\}$ acts on both the position r_j of the atom and on the components α of the axial vector that describes the moment. h is the rotational part of the symmetry element and τ the translational part (Seitz notation). The operation that sends r_j in the zeroth cell to r_i in the pth cell can be symbolically stated as:

$$g(j0) \longrightarrow (ia_p) \tag{2.14}$$

In other terms, the effect of a symmetry operation g is to permute the column matrix of atom labels, $\mathbf{P}$:

$$g(\mathbf{P}) \longrightarrow \mathbf{P}' \tag{2.15}$$

This operation is governed by a permutation representation, Γ_{perm}, which has matrices of order N_A, where N_A is the number of equivalent positions of the crystallographic site. It is important to note that when a symmetry operation results in an atomic position that is outside the zeroth cell, a phase factor must be included that relates the generated position to that in the zeroth cell. This phase is simply given by:

$$\theta = -2\pi \mathbf{k}.\mathbf{T} \tag{2.16}$$

where $\mathbf{T}$ is the translation vector, that relates the original and generated atoms.

The second effect of this symmetry operation is to transform the spin components with index α, (α=x,y,z) of the reference spin j into the index α' of the atom r_i. These transformations are described by the axial vector representation, $\widetilde{V}$, the character of which is given by:

$$\chi_{\widetilde{V}}^h = \sum_{a=b} R_{ab}^h det(h) \tag{2.17}$$

where R_{ab}^h refers to a specific element a,b of the rotation matrix h, and det(h) represents the determinant of the rotation matrix R^h, and has the value of +1 for a proper and -1 for an improper rotation.

The magnetic representation Γ describes both the result of the symmetry operation on the atomic positions, and on the axial vectors that describe the magnetic moment. As these effects are independent, the magnetic representation is given by their direct product:

$$\Gamma = \widetilde{V} \times \Gamma_{perm} \tag{2.18}$$

Or, in terms of the matrices for the representations themselves

$$D^{\Gamma}_{h,\tau_h} = D^{\widetilde{V}}_h \times D^{\Gamma_{perm}}_{h,\tau_h} \tag{2.19}$$

The Γ representation of eqn. 2.18 is usually reducible. To reduce this representation, we have to use the formula of eqn. 2.12.

Remark: Whereas for a unitary group there are representations and irreducible representations, for a non-unitary group in which half the elements are unitary and the other half are anti-unitary, there are corepresentations and irreducible corepresentations. Grey and Black and White magnetic groups contain both unitary and anti-unitary operations. One has then to consider the problem of the representations containing anti-unitary elements. If we write a anti-unitary group $\mathbf{M} = \mathbf{G}+\mathrm{R}\mathbf{G}$ as for the grey paramagnetic groups, where g_i are the elements of $\mathbf{G}$ and $a_i=\mathrm{R}g_i$. If $\mathrm{D}(g_i)$ and $\mathrm{D}(a_i)$ are the matrices associated with the g_i and a_i respectively, it is not possible to construct matrix representations of $\mathbf{M}$ following the usual composition rule for representations of unitary groups: $\mathrm{D}(h_i)\mathrm{D}(h_j)=\mathrm{D}(h_ih_j)$, but one can form a corepresentation of $\mathbf{M}$ using the alternative composition rules:

$$
\begin{aligned}
D(g_i)D(g_j) &= D(g_ig_j) \\
D(g_i)D(a_j) &= D(g_ia_j) \\
D(a_i)D^*(a_j) &= D(a_ig_j) \\
D(a_i)D^*(a_j) &= D(a_ia_j)
\end{aligned}
\tag{2.20}
$$

It has been shown that the irreducible corepresentations of a magnetic non-unitary group $\mathbf{M}$, can be deduced from the irreducible representations of the associated crystallographic subgroup $\mathbf{G}$ [7]. Three situations are distinguished depending if the matrices of the considered irreducible representations are real or imaginary, and also on the nature of the anti-unitary operations pertaining to $\mathbf{M}$. If we only consider here the question of essential interest in the interpretation of magnetically ordered systems, namely the description of transitions from a paramagnetic to a magnetically ordered phase, then we can restrict ourselves to the problem of constructing the irreducible corepresentations of paramagnetic groups. As the time reversal operator R belongs by itself to the grey groups, it is possible to show that no degeneracies take place for the energy eigenvalues of the Hamiltonian of the system. So the representation space has the same dimensionality for the irreducible corepresentations and for the corresponding irreducible representations.

Determination of primed and unprimed elements

In order to determine the magnetic space group and also its magnetic point group, one needs to know when a symmetry element should be primed or not. In other words, when the current loop is invariant: by application of a symmetry element or by its corresponding antielement?

We will illustrate this point by taking the example of the point group 222 (D_2, table 2.3).

	1	2_z	2_y	2_x	Magnetic point group
A	1	1	1	1	222
B_1	1	1	-1	-1	$22'2'$
B_2	1	-1	1	-1	$2'22'$
B_3	1	-1	-1	1	$2'2'2$

Table 2.3: *Irreducible representations for point group D_2.*

Each line in table 2.3 corresponds to an irreducible representation (IR). To each IR, we can associate a magnetic point group by keeping the same elements when the character is +1 and changing them to antielements when the character is -1 (in the case of real values). For the case of complex values, there always exists a unitary transformation which can transform the elements of IRs to real values.

We will consider here and in the remainder of the thesis only the cases where the magnetic structure is commensurate with the lattice. The corresponding magnetic point groups are given in the last column of table 2.3. Mathematically, it means that we have two possibilities. If g sends atom 1 on atom 2 thus:

$$\widetilde{V}(g)S_1 = -S_2 \quad or \quad + S_2$$

If one obtains -S_2, g has to be primed otherwise not. In the investigation for magnetic symmetry determination, there is in fact another possibility: $\widetilde{V}(g)S_1 \neq -S_2 \quad or \quad \neq +S_2$. In that case, it means that the symmetry element g is lost in the magnetically ordered phase.

2.2.2   The magnetoelectric effect

Compounds presenting coexistence of several possible ferroic states have attracted a lot of attention since several decades due their interesting properties. Among them, materials presenting simultaneously ferroelectric and magnetic orders were the subject of intensive studies in recent years [8]. They have interesting properties allowing the manipulation of electric and magnetic moments by magnetic and electric fields, respectively. We refer to multiferroics, as compounds presenting ferroelectric order and anti or

ferromagnetic order. The d^0 configuration that is favored for typical ferro-electrics as $BaTiO_3$ is incompatible with magnetism. This feature explains the interest generated by these compounds.

However there is another way to generate polarization which is through the magnetoelectric effect. This effect has been first predicted by Curie in 1894 [9]. He stated that materials that develop an electric polarization in a magnetic field or a magnetization in an electric field may exist. Later, based on the prediction of Dzyaloshinskii [10], Astrov showed the existence of magnetoelectric effect in Cr_2O_3 [11]. The general expression for the free-energy of such materials (we will consider here only the linear effect) can be written in the form:

$$\Phi = \Phi_0 - \alpha_{ij} E_i H_j \tag{2.21}$$

α_{ij} refers to the components of the magnetoelectric tensor. If an electric field $\mathbf{E}$ is applied to a crystal with potential 2.21, a magnetization will be produced:

$$M_j = -\frac{\partial \Phi}{\partial H_j} = \alpha_{ij} E_i \tag{2.22}$$

And the conjugate expression, one can produce polarization while applying a magnetic field:

$$P_i = -\frac{\partial \Phi}{\partial E_i} = \alpha_{ij} H_j \tag{2.23}$$

Experimentally, since most of the research for new magnetoelectrics is concentrated on bulk, this is often how is evidenced the magnetoelectric coupling in these materials. Indeed since, the electric field necessary to polarize the bulk is usually beyond the reachable value of the experimental set-ups. While a lot of effort has been put into the search and design of new magnetoelectric compounds, there is no systematic approach to look for new materials. However, from the equations 2.22 and 2.23, a systematic symmetry approach seems to be sufficient in the search for new materials. Historically, it has been this approach which has been privileged. However at the revival of the research on multiferroic/magnetoelectric compounds, this approach has been more or less forgotten.

$\mathbf{M}$ like $\mathbf{H}$ is an axial vector and $\mathbf{P}$ like $\mathbf{E}$ is a polar vector. As a consequence of the equations 2.22 and 2.23 (one can express $\mathbf{P}$ function of $\mathbf{H}$ and $\mathbf{M}$ function of $\mathbf{E}$), a linear magnetoelectric effect will be allowed under the application of a magnetic field when terms like $L_i M_j P_k$ or $M_i M_j P_k$ are allowed in the free-energy of the system. In these terms, L_i is an antiferromagnetic component and M_j a ferromagnetic component. Indeed if one looks at the minima of the free-energy (eq. 2.22 and 2.23), one can replace $\mathbf{E}$ as a function of $\mathbf{M}$ and $\mathbf{H}$ as a function of $\mathbf{P}$. However, due to

the time inversion which reverse the sign of the spins, terms like L_iP_k or M_jP_k won't be invariant. Consequently, if the free energy of the system contains terms like $L_iM_jP_k$ or $M_iM_jP_k$, the system will be able to present a linear magnetoelectric effect (chapter 6). Later on, we will either derive the full free-energy of the system by considering the terms which are allowed by symmetry, either just look for terms like above to predict a possible linear magnetoelectric effect. We present our results and give examples of predicted magnetoelectric materials using systematic symmetry investigation (chapter 6).

In the remainder of this chapter, we will discuss only the linear magnetoelectric effect since it is the one presenting the most promising for applications and the easier to probe experimentally. While speaking about the existence of magnetization, it is obvious that the magnetoelectric effect is forbidden in all dia and paramagnetic compounds. In terms of symmetry, it means that the symmetry of these compounds possess R (the time inversion element) which causes the reversal of the magnetic moment density. The magnetoelectric effect is also forbidden if the magnetic space group contains translations multiplied by R because in these cases the point group also possesses R as a separate element which is equivalent to a dia or paramagnetic group. We remind the reader that the vector **H** is an axial vector while the **E** vector is a polar vector and in consequence they behave differently under R. There are in total 122 magnetic point groups which describe 1651 magnetic space groups. These numbers may look very big if one wants to do a systematic approach. However, we will see that in several magnetic space groups, the situation regarding the eventual presence of magnetoelectricity is simplified a lot.

From eqn. 2.21, we can see that α_{ij} is a tensor of second rank and its components change sign under the application of R. The magnetic centrosymmetric space groups do not allow a magnetoelectric effect. However the ones which possess the element $\overline{1}'$ resulting from the application of spatial inversion and time inversion can present a magnetoelectric effect. If one does a systematic analysis of the 122 magnetic point groups, one can see that the magnetoelectric effect is allowed only in 58 magnetic point groups. Among these ones, there are only 11 possible forms for the tensor α_{ij}. The general expression of the magnetoelectric tensor is [12]:

$$\begin{pmatrix} \alpha_{11} & \alpha_{12} & \alpha_{13} \\ \alpha_{21} & \alpha_{22} & \alpha_{23} \\ \alpha_{31} & \alpha_{32} & \alpha_{33} \end{pmatrix} \tag{2.24}$$

The different forms of the tensor α_{ij} are presented in table 2.4 [12].

Magnetic crystal classes	Non zero tensor components α_{ij}
1 and $\bar{1}$'	α_{ij} for (i,j) $\in$ [1,2,3]
2, m' and 2/m'	α_{11}, α_{13}, α_{22}, α_{31}, α_{33}
m, 2'and 2'/m	α_{12}, α_{21}, α_{23}, α_{32}
222, m'm'2 and m'm'm'	α_{11}, α_{22}, α_{33}
mm2, 2'2'2, 2'mm' and mmm'	α_{12}, α_{21}
4, $\bar{4}$', 4/m', 3, $\bar{3}$', 6, $\bar{6}$' 6/m'	α_{11}=α_{22}, α_{12}=-α_{21}, α_{33}
$\bar{4}$, 4', 4'/m'	α_{11}=α_{22}, α_{12}=-α_{21}
422, 4m'm', $\bar{4}$'2m', 4/m'm'm', 32, 3m', $\bar{3}$'m', 622, 6m'm', $\bar{6}$'m'2, 6/m'm'm'	α_{11}=α_{22}, α_{33}
42'2', 4mm, $\bar{4}$'2'm, 4/m'mm, 32', 3m, $\bar{3}$'m, 62'2', 6mm, $\bar{6}$'m2', 6/m'mm	α_{12}=-α_{21}
4'22', 4'm'm, $\bar{4}$2m, 4'/m'm'm, $\bar{4}$2'm'	α_{11}=-α_{22}
23, m'$\bar{3}$', 432, $\bar{4}$'3m',m'$\bar{3}$'m'	α_{11}=α_{22}=α_{33}

Table 2.4: *Expressions of the tensor α_{ij} in the case of the linear magnetoelectric effect [12].*

References

[1] Technique of inorganic chemistry, Vol. IV, Edited by H. B. Jonassen and A. Weissberger, Interscience Publishers, 1965

[2] Dielectric relaxation in solids, A. K. Jonscher, Chelsea Dielectrics Press, 1983

[3] Reports on Progress in Physics, vol. **49**, part 4, Edited by M. Prutton, 1986

[4] The Mathematical Theory of Symmetry in Solids, C. J. Bradley and A. P. Cracknell, Clarendon Press, Oxford, 1972; Group theory and Quantum Mechanics, M. Tinkham, Dover Publications, Inc., 2003

[5] The Mathematical Theory of Symmetry in Solids, C. J. Bradley and A. P. Cracknell, Clarendon Press, Oxford, 1972; Group theory and Quantum Mechanics, M. Tinkham, Dover Publications, Inc., 2003; E. F. Bertaut, Acta Cryst. A**24**,217(1968); E. F. Bertaut, J. Magn. Magn. Mat. **24**,267 (1981); Y. A. Izyumov and V. E. Naishi, J. Magn. Magn. Mat. **12**, 239 (1979); Y. A. Izyumov and V. E. Naishi, J. Magn. Magn. Mat. **12**, 249 (1979); Neutrons et Magnétisme, Journal de Physique IV, Edited by C. Fermon and F. Tasset;

The Landau Theory of Phase Transitions, J.-C. Tolédano and P. Tolédano, World Scientific, 1987

[6] International Tables for Crystallography, Vol. A, Space group Symmetry, Edited by T. Hahn, Second Revised Edition, D. Reidel Publishing Company, 1987

[7] E. P. Wigner, Group theory and its application to the quantum mechanics of atomic spectra, Academic Press, New-York, 1959

[8] J. Wang *et al.*, Science **299**, 1719 (2003);Kimura *et al.*, Nature **426**, 55 (2003) and Hur *et al.*, Nature **429**, 392 (2004)

[9] P. Curie, J. de Phys. 3ème série,**3**, 393 (1894)

[10] I. E. Dzialoshinskii, Sov. Phys. JETP, **10**, 628 (1960)

[11] D. N. Astrov, Sov. Phys. JETP, **11**, 708 (1960)

[12] International Tables for Crystallography, Vol. D, Physical Properties of crystals, Edited by A. Authier, Kluwer Academic Publishers, 2003

Chapter 3

Orbital Ordering in RTiO$_3$

3.1 Introduction

The transition metal perovskite oxides ABO$_3$ with partially filled d-orbitals have been intensively investigated in order to understand the nature of their electronic states. In cases where the partially occupied orbitals are degenerate, the degeneracy is usually lifted and long-range ordering of the occupied orbitals occurs below a transition temperature. However, the local degeneracy may already be lifted above T$_C$. Such ordering is accompanied by a coherent Jahn-Teller (JT) distortion, which often results in a change of crystal symmetry. The most widely studied of such systems is La$_{1-x}$A$_x$MnO$_3$ series (A = Ca, Sr, Ba), where the JT effect due to degeneracy of the e$_g$ orbitals, is known to play an important role in the mechanism of the colossal magnetoresistance phenomenon, emerging in these materials upon doping [1]. Of more recent interest is the quantum effect in the orbital ordering dominated by electron correlations. With respect to e$_g$ systems, t$_{2g}$ systems have a larger degeneracy and weaker coupling to the lattice.

Here, we report on the rare-earth titanates RTiO$_3$, which belong to the t$_{2g}$ degenerate systems. RTiO$_3$ has an orthorhombically distorted perovskite structure (space group: Pbnm) (see figure 3.1). The RTiO$_3$ system is fascinating and has generated a tremendous amount of work. The debate focuses on the possible interactions lifting the threefold degeneracy of the t$_{2g}$ orbitals in the ground state. The TiO$_6$ octahedra in LaTiO$_3$ exhibit small GdFeO$_3$ related distortions [2]. One would expect, at first sight, quadruply degenerate single-ion ground states, represented by fictitious angular momentum due to spin-orbit (SO) interaction, with unquenched orbital moment. This scenario is consistent with the observed reduced magnetic moment [3]. However, Keimer *et al.* suggested that the SO interaction is not dominant in this system, because they observed an isotropic spin-wave dispersion [4]. They therefore proposed a model of strongly fluctuating orbital states [4, 5], followed by a calculation of the orbital excitations [6].
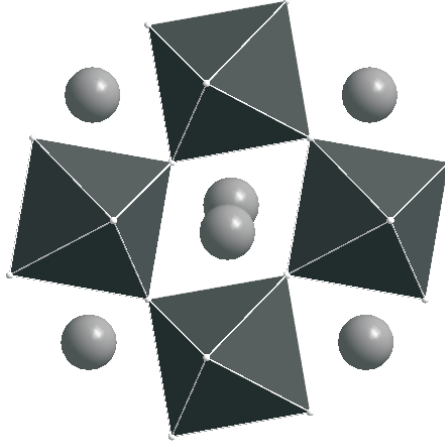
Figure 3.1: *Crystal structure of LaTiO$_3$ in space-group Pbnm in the (a,b) plane.*

On the other hand, Mochizuki and Imada have successfully explained the physical properties of LaTiO$_3$ by an orbital state expressed approximately as $\frac{1}{\sqrt{3}} \times (d_{xy} + d_{yz} + d_{zx})$[7]. Subsequently, corresponding distortions of the TiO$_6$ octahedra have been reported from detailed structural data [8] with a T$_{OO}$ (temperature of orbital ordering)$\sim$T$_N$. The orbital state in RTiO$_3$ with R = La-Nd proposed by Mochizuki and Imada can result from a crystal field and is supported by NMR experiments [9]. The reduced moment of Ti^{3+} and the different arguments given to explain this unexpected observation [4, 5, 6, 10, 11] motivated us to perform further experiments in comparison with known orbital ordered and disordered systems.

We have investigated two compounds of the RTiO$_3$ family, LaTiO$_3$ and YTiO$_3$ looking for possible lowering of symmetry due to orbital ordering. Several studies have concluded that YTiO$_3$ exhibits an orbital ordering from both experimental [12, 13] and theoretical results [10, 13]. We expect that the orbital ordering pattern is reflected in the crystal structure, as for orbital ordered systems like RMnO$_3$, RVO$_3$ and ACuX$_3$ (A = alkali, X = halogen) [14, 15, 5]. Here, the orbital ordering resulting from a cooperative JT effect, gives rise to a lowering of the symmetry expressed by the JT theorem [17]. This lowering of the symmetry in the JT active systems is often the signature of the orbital ordering. We can also observe a pseudo-JT effect which would give rise to a distortion of the octahedra but without change of symmetry as in orthorhombic RMnO$_3$ [14, 18]. We discuss our results in the light of already proposed theories and the GdFeO$_3$ distortion type that is present in the RTiO$_3$ family.

3.2 Experimental

Single-crystal samples of $RTiO_3$ have been synthesized in one step by direct reaction of Ti metal (99.9%, metal basis), R_2O_3 (99.99%) and TiO_2 (99.9%, metal basis) by the floating zone technique using a four-mirror furnace in a flow of 5% H_2/95% Ar gas. The oxide starting materials were predried overnight at 1000°C before use. The magnetic properties of $RTiO_3$ are very sensitive to the content of oxygen [19]. The high quality of the $YTiO_3$ and $LaTiO_3$ crystals is evidenced by narrow diffraction peaks (FWHM = 0.0087±0.00031) and the values of the magnetic transition temperatures of T_C~30 K and T_N~145 K respectively. Powder diffraction was performed on beamline ID31 at ESRF. We used a X-ray energy of 40 keV and a step size of 0.003° in 2θ. The temperature was controlled with a liquid-helium-cooled cryostat with spinning quartz capillary. Data sets were collected at 5K, 100K and 295K for $YTiO_3$ and at 5K, 100K, 175K and 295K for $LaTiO_3$. The data were analyzed by the Rietveld method implemented in the GSAS software package [20]. The background levels of the X-ray diffraction profiles were modelled using a simple linear interpolation of the seventh kind (in GSAS nomenclature) with 12 and 24 parameters, for $LaTiO_3$ and $YTiO_3$ respectively. The peak shape of the profiles was described by a convolution of a pseudo-Voigt function with an instrumental asymmetry (peak profile function 4 in GSAS). The data have been corrected for both compounds by taking into account the anomalous scattering factors (f' and f''). The values of these factors were derived by using the program Fprime [21].

3.3 Results

3.3.1 Refinements

We obtain a good refinement for both compounds $YTiO_3$ and $LaTiO_3$ in the Pbnm symmetry as illustrated in figure 3.2. The good refinements are confirmed by the good statistics that we obtained R_{wp} = 6.05% and R_p = 4.99% for $LaTiO_3$ and R_{wp} = 7.72% and R_p = 6.43% for $YTiO_3$ at 5K. We did not observe any signature of a possible splitting of reflections which could be the signature of a lowering of the Pbnm symmetry.
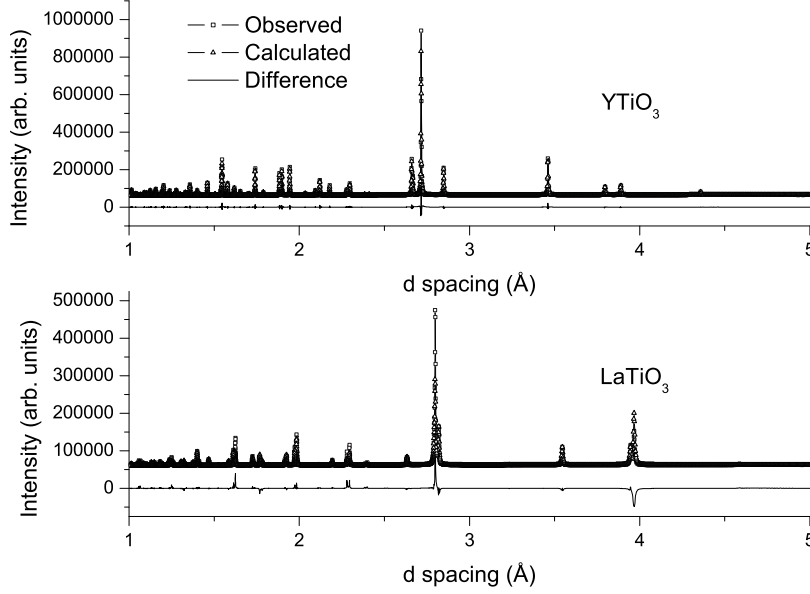
Figure 3.2: *Comparison of the fit of the recorded pattern of LaTiO$_3$ (bottom) and of YTiO$_3$ (top) at 5K. Similar quality of the refinements is obtained at all the measured temperatures for both compounds. The squares represent the observed pattern, the triangles represent the calculated pattern and the straight line represents the difference between both.*

We observe as a function of temperature in LaTiO$_3$ between 5K and 295K that while the *b* and *c* cell parameters increase by 0.482% and 0.187% respectively, the *a* cell parameter contracts by 0.161% resulting in an increase of the volume (cf. figure 3.3). As reported by Cwik *et al.* [8], one can see that this temperature effect on the cell parameters is particularly pronounced around the magnetic transition temperature. This can be interpreted either as a pure magnetostrictive effect or as a mixture of the strictions due to the magnetic ordering and a possible orbital ordering. This issue will be discussed in the next section.
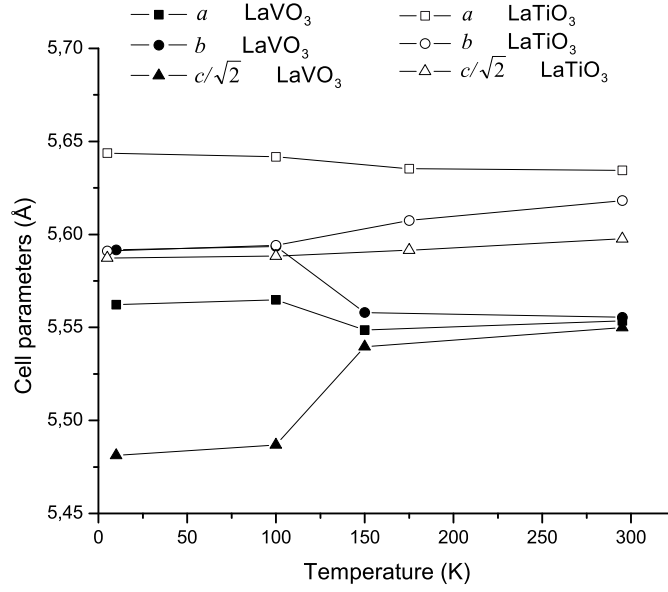
Figure 3.3: *Comparison of the cell parameters of LaTiO₃ and of LaVO₃ extracted from [22] versus temperature.*

In figure 3.4, we present the evolution of the cell parameters versus temperature of $YTiO_3$. One can see that the temperature dependence of $YTiO_3$ is different than in the case of $LaTiO_3$. Indeed while the cell parameter b is increasing versus temperature in $LaTiO_3$, it is decreasing in $YTiO_3$ by 0.064% around the magnetic ordering temperature between 5K and 100K (T_C=30K). The other cell parameters a and c are increasing by 0.0802% and 0.0113%, respectively. One of the other main differences between $YTiO_3$ and $LaTiO_3$ is the cell parameters variations versus temperature. This difference is very significant since there is about one order of magnitude of difference between $LaTiO_3$ and $YTiO_3$. This difference in the variation of the cell parameters can be explained by the difference in the strength of the magnetic exchange between $LaTiO_3$ and $YTiO_3$.
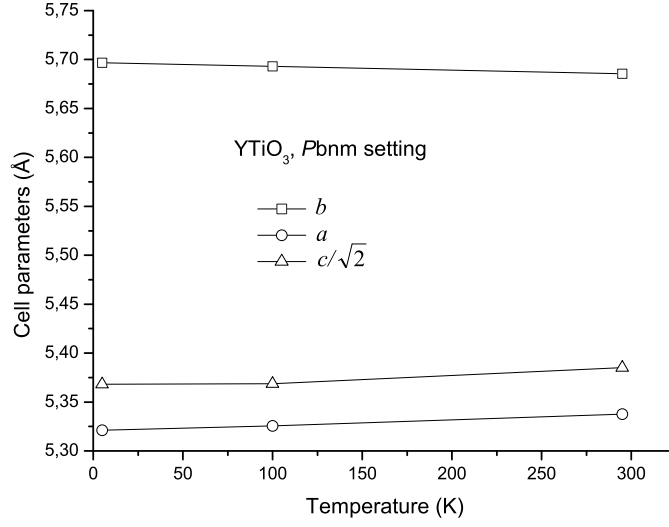
Figure 3.4: *Evolution of the cell parameters of YTiO$_3$ as a function of temperature.*

In tables 3.1 and 3.2, we present the results of the refinements of both compounds LaTiO$_3$ and YTiO$_3$ at all temperatures in the Pbnm setting. Although these compounds do not present any obvious monoclinic distortion at any temperature, they still may present orbital ordering with conservation of the Pbnm symmetry as in the case of the orthorhombic RMnO$_3$ [14, 18]. We will discuss the possible ordering in section 4.8.

Sample	5K	100K	175K	295K
a (Å)	5.64368(2)	5.64179(2)	5.63534(2)	5.63468(2)
b (Å)	5.59114(2)	5.59424(2)	5.60740(2)	5.61838(3)
c (Å)	7.90163(3)	7.90322(3)	7.90761(3)	7.91659(3)
Ti-O$_1$(Å)	2.0289(6)	2.0279(6)	2.0289(7)	2.0319(8)
Ti-O$_{21}$(Å)	2.038(2)	2.035(2)	2.033(2)	2.026(3)
Ti-O$_{22}$(Å)	2.0478(2)	2.052(2)	2.055(3)	2.064(3)
La				
x	0.99318(6)	0.99323(6)	0.99307(7)	0.99311(8)
y	0.04919(4)	0.04860(4)	0.04735(5)	0.04509(5)
z	0.25	0.25	0.25	0.25
O$_1$				
x	0.0818(5)	0.0806(5)	0.0806(5)	0.0812(6)
y	0.4935(4)	0.4931(4)	0.4920(5)	0.4916(6)
z	0.25	0.25	0.25	0.25
O$_2$				
x	0.7080(4)	0.7081(4)	0.7087(4)	0.7103(5)
y	0.2940(4)	0.2947(4)	0.2947(5)	0.2948(5)
z	0.0426(2)	0.0425(2)	0.0422(3)	0.0420(3)
U$_{iso}$				
La	0.00215(5)	0.00322(5)	0.00443(5)	0.00696(6)
Ti	0.0011(1)	0.0016(1)	0.0019(1)	0.0032(1)
O$_1$	0.0043(7)	0.0041(7)	0.0097(8)	0.0084(9)
O$_2$	0.0041(5)	0.0039(5)	0.0059(5)	0.0059(6)

Table 3.1: *Results of the synchrotron powder diffraction study at different temperatures of LaTiO$_3$ using Pbnm symmetry. Lattice constants are given in Å and thermal parameters in Å^2 at different temperatures.*

Sample	5K	100K	295K
a (Å)	5.32120(1)	5.32547(1)	5.33741(1)
b (Å)	5.69676(1)	5.69312(1)	5.68529(1)
c (Å)	7.59151(2)	7.59237(2)	7.61562(2)
Ti-O_1	2.0224(9)	2.0208(9)	2.0252(9)
Ti-O_{21}	2.027(2)	2.027(2)	2.031(2)
Ti-O_{22}	2.070(2)	2.072(2)	2.073(2)
Y			
x	0.97791(7)	0.97804(7)	0.97913(8)
y	0.07432(6)	0.07429(6)	0.07311(6)
z	0.25	0.25	0.25
O_1			
x	0.1228(5)	0.1219(5)	0.1211(5)
y	0.4565(5)	0.4571(5)	0.4572(5)
z	0.25	0.25	0.25
O_2			
x	0.6903(4)	0.6903(4)	0.6901(4)
y	0.3075(4)	0.3080(4)	0.3080(4)
z	0.0577(3)	0.0580(3)	0.0586(3)
U_{iso}			
Y	0.00344(7)	0.00460(7)	0.00716(9)
Ti	0.0034(1)	0.0043(1)	0.0059(1)
O_1	0.0049(6)	0.0051(6)	0.0063(6)
O_2	0.0063(4)	0.0069(5)	0.0100(5)

Table 3.2: *Results of the synchrotron powder diffraction study at different temperatures of YTiO$_3$ using Pbnm symmetry. Lattice constants are given in Å and thermal parameters in Å^2 at different temperatures.*

3.3.2 Asymmetric peak shape below T_N

Despite of the good refinements done with Pbnm symmetry, we observe some asymmetry in some reflections during the refinements on LaTiO$_3$. We remind the reader that a pseudo-Voigt peak profile function convoluted to an instrumental asymmetry has been used to describe the peak shape. But in addition to this instrumental asymmetry, we observe for LaTiO$_3$ an extra asymmetry of experimental (sample) origin. This asymmetry starts to develop under T_N. This asymmetry is characterized by a tail on the left side of (hkl) reflections having a high value of h (see figure 3.5). On the contrary for reflections having a high value of k, the tail starts to develop on the right side (see figure 3.6). However, no asymmetry could be observe on the reflections having a high l value irrespective of the temperature.
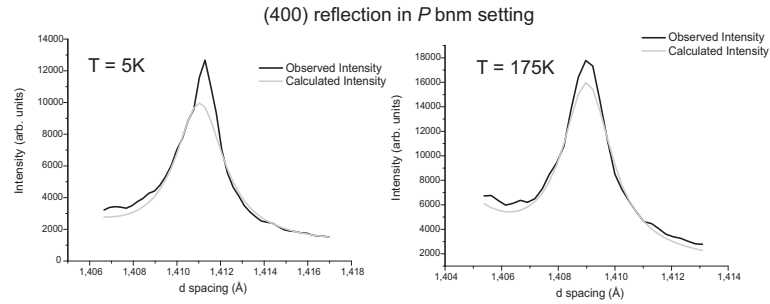

Figure 3.5: *Refinement of LaTiO$_3$ in Pbnm setting. An asymmetry (left tail) is observed under T_N of the (400) reflection (T=5K, left panel) which is not present above T_N (T=175K, right panel).*

The asymmetries in the peak shape observed in the refinements of LaTiO$_3$

are not present for the refinements done on YTiO$_3$. The main difference between these two compounds is the type of magnetic ordering. While LaTiO$_3$ orders antiferromagnetically under T$_N \approx$145K, YTiO$_3$ orders ferromagnetically with a magnetic moment along the c axis (Pbnm setting) below T$_C \approx$30K. The experimental asymmetry follows the trends in lattice parameters through T$_N$. The response of the lattice below T$_N$ is different in different parts of the sample. There is a continuous range of lattice parameters. This asymmetry could result from the magnetostriction which would involve new strain components giving rise to this asymmetry. YTiO$_3$ presents a different magnetic ordering and thus one can expect a different behavior than in LaTiO$_3$. However further and more thorough investigations are necessary in order to clarify the origin of this asymmetry in LaTiO$_3$.
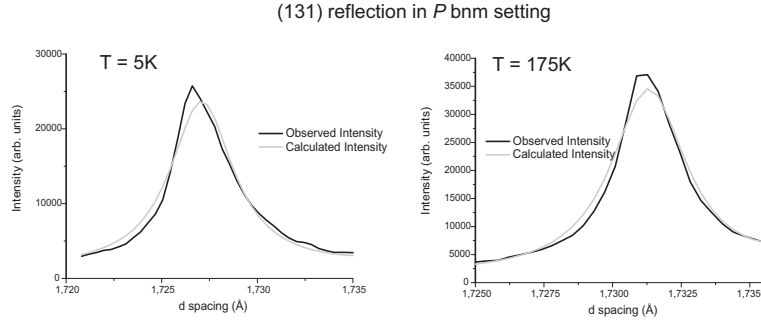

Figure 3.6: *Refinement of LaTiO$_3$ in P bnm setting. An asymmetry (right tail) is observed under T$_N$ of the (131) reflection (T=5K, left panel) which is not present above T$_N$ (T=175K, right panel).*

3.4   Discussion

3.4.1   Possible structural signature of Orbital Ordering

LaTiO$_3$

One should notice that the anomaly in the cell parameters in LaTiO$_3$ is much smaller than in the related compound LaVO$_3$ (which is also a t$_{2g}$ system with T$_N \sim$ 140K) where the a, b and c cell parameters change by a factor of 2.1, 2.6 and 16.7 times more than in LaTiO$_3$, respectively, between 100 K and 150 K [22] (see figure 3.3).

The orbital ordering is often probed structurally by an anisotropy in the metal-oxygens bond distances (M-O) resulting from a particular distortion mode. In the Pbnm space-group, the symmetry already allows a differentiation in the different M-O bonds since only the inversion center remains compared to the O$_h$ symmetry. In figure 3.7, we show the evolution versus temperature of the different Ti-O bond distances. O$_1$ is the apical oxygen

while O_{21} and O_{22} form the basal plane of the octahedra. As stated already, we see that we have 3 different bond distances. As a function of temperature, one of the basal plane Ti-O distance (Ti-O_{22}) and Ti-O_1 increase continuously while the bond distance Ti-O_{21} decreases. Around T≈225K, we observe that Ti-O_1≈Ti-O_{21}. We notice that our results are significantly different than the ones of Cwik *et al.* [8]. They found that one of the basal plane Ti-O is independent of temperature. The other Ti-O bond distance belonging to the basal plane is almost temperature independent. This is in contradiction with our results where we observe that one is contracting while the other one is expanding. Moreover we can notice that it is unexpected to have no variations in bond length over almost 300K.

In order to investigate the possible structural signature of any orbital ordering, we compare our data with another t_{2g} system which is not orbital ordered: LaCrO$_3$ (*P*bnm symmetry, Cr^{3+}, $t_{2g}^3 e_g^0$). At room temperature, the M-O bond distances are 1.957Å, 1.930Å and 2.009Å [23]. In LaCrO$_3$, as in LaTiO$_3$, the variations in bond length M-O in the basal plane versus temperature are similar [24]. Moreover the distortion scheme is strictly similar. While M-O_1 and M-O_{22} increase with temperature, M-O_{21} decreases. Thus we believe that the temperature behavior of LaTiO$_3$ is simply the typical temperature behavior for a t_{2g} populated system having *P*bnm symmetry. Moreover, recent spin-resolved photoelectron spectroscopy experiment claims the absence of orbital ordering in LaTiO$_3$ [25]. Thus, from these simple structural parameters, LaTiO$_3$ does not present any structural signature of a possible Jahn-Teller ordered state below its Néel temperature.
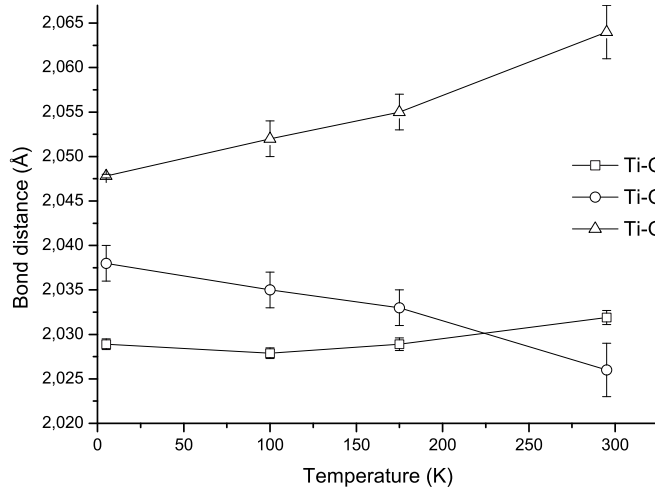

Figure 3.7: *Evolution of the Ti-O bond distances in LaTiO$_3$ versus temperature in the *P*bnm setting.*

$YTiO_3$

Since the critical temperatures of both studied compounds have a factor 5 of difference (145K versus 30K), we think that the difference of exchange striction can be explained by the difference of the magnitude of the magnetic dipole. As in LaTiO$_3$, we present in figure 3.8 the temperature behavior of the Ti-O bond distances. As in LaTiO$_3$ due to the Pbnm symmetry, we observe 3 different bond distances. However, on the contrary of LaTiO$_3$, we notice that one of the basal plane Ti-O distance is significantly larger than the two others. This has been one of the reasons for which several works reported orbital ordering in YTiO$_3$. This differentiation in the bond distances is also present at room temperature suggesting that the orbital order exists already at room temperature. This is very surprising. Indeed since the t$_{2g}$ orbitals are much less coupled to the lattice and due to the higher degeneracy, the orbital ordered/disordered transition is expecting to take place at much lower temperature than in the e$_g$ system. It is consistent with the study of orbital ordering in RVO$_3$ where the transition temperatures are well below room temperature [15, 26]. Thus we would expect the same for titanates.

As stated already the orbital ordering is reflected in the asymmetry of the distribution of the bond distances. It is effectively what is observed for YTiO$_3$. However, it is not sufficient. If there is an orbital ordered state, the anisotropy of the bond distances disappears or at least is reduced versus temperature. And it is not what we observe in figure 3.8. We see that the difference between the 2 short bonds and the long Ti-O bond remains constant as a function of temperature. This indicates that the existence of 2 short and 1 long bond distances is not related to a possible orbital order. This has been already observed in YCoO$_3$ which presents similar structural properties (Pbnm symmetry, 2 long and 1 short M-O bond distances). A study from room temperature until 1000K demonstrated that the difference between the short and the long bond distances was more or less constant between room temperature and 1000K [27]. Thus, we can say that the structural features of YTiO$_3$ can not be ascribed to an orbital ordered state.
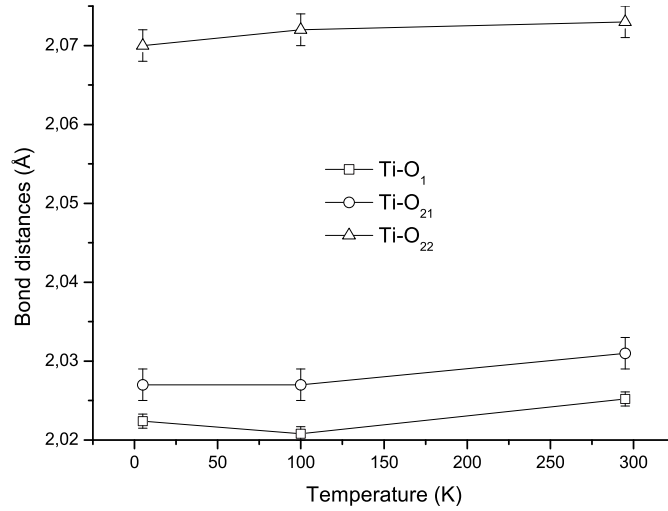
Figure 3.8: *Evolution of the Ti-O bond distances in YTiO$_3$ versus temperature in the* P*bnm setting.*

3.4.2 GdFeO$_3$ distortion versus Orbital Ordering

About the in-plane distortion

Cwik and collaborators have investigated using neutron powder diffraction, the distortions of the octahedra network of LaTiO$_3$. Making a comparative study with other rare-earths, they observed a strong variation in the basal plane edge lengths for the large rare-earths. They use the parameter r$_{O_2-O_2}$=(O$_2$-O$_2$long/O$_2$-O$_2$short) to quantify this distortion. Contrary to the large rare-earths, the variation of the Ti-O distances for small rare-earth was found to be large with small distortion of the basal plane of the octahedron. The two distinct deformations of the octahedron were interpreted as two different orbital ordering schemes. Following the approach taken by Cwik *et al.*, we have investigated the variations in the Ti-O distances as well of the basal plane edges defined respectively by r$_{O_2-O_2}$ and r$_{M-O}$=(Ti-Olong/Ti-Oshort). We plot in figure 3.9 the basal plane edge lengths of LaTiO$_3$ and YTiO$_3$ as obtained from our refinements. We observe as Cwik *et al.* that the difference between the two basal plane edges is significantly smaller in YTiO$_3$ compared to LaTiO$_3$.
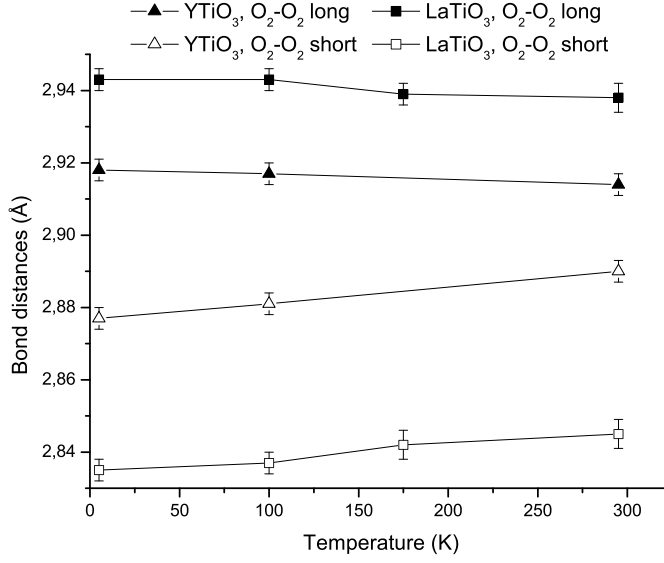
Figure 3.9: *Distortion of the basal plane of octahedron TiO$_6$ in RTiO$_3$ as a function of temperature.*

The existence of a difference between the M-O distances and O-O distances of the basal plane is directly related to the pseudo-cubic structure adopted by the RTiO$_3$ family. To investigate the structural signature of orbital ordering in RTiO$_3$, we compare the available data on RTiO$_3$ with a very well known non orbital ordered system RFeO$_3$. This family presents like the RTiO$_3$ a pseudo-cubic structure (space-group Pbnm) but no orbital ordering. We plot in figure 3.10 the r$_{O_2-O_2}$ parameter and the r$_{M-O}$ parameter in figure 3.11 of the RFeO$_3$ and RTiO$_3$ families. For this purpose, we use the different reported structures in the literature [2, 28].
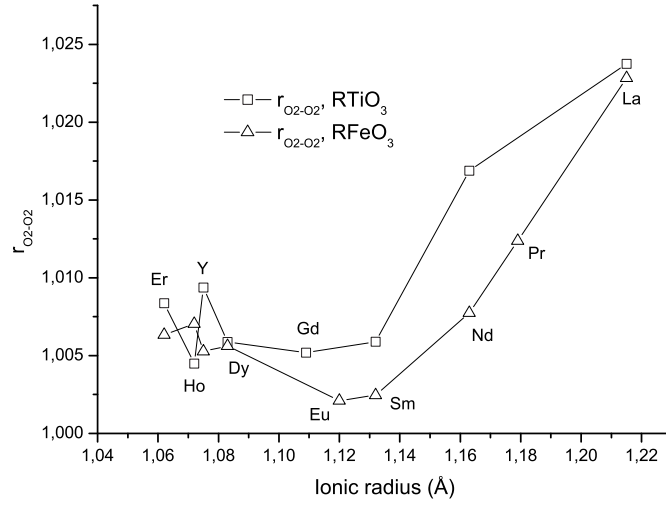
Figure 3.10: *Comparison of the distortion of the basal plane of MO_6 octahedron between the $RFeO_3$ and $RTiO_3$. We use the same parameter $r_{O_2-O_2}=O_2$-O_2long/O_2-O_2short as Cwik [8]. We use structural parameters reported in literature for comparison [2, 28]*

.

As noticed by Cwik *et al.*, we observe a change in the trend of both parameters $r_{O_2-O_2}$ and r_{M-O} around an ionic radius corresponding to Sm. However, this trend is also present in the $RFeO_3$ system. For the $r_{O_2-O_2}$ parameter, we see that the value of the parameter and the trend is very similar between the $RTiO_3$ and $RFeO_3$ systems. Concerning the r_{M-O} parameter, the trend is also similar between the $RTiO_3$ and $RFeO_3$ systems. The difference in the value of r_{M-O} parameter is decreasing when increasing the size of the rare-earth to finally vanish for the bigger rare-earth. We conclude that the two distinct deformations ($r_{O_2-O_2}$ and r_{M-O}) are determined by the rare-earth ionic radius variation. These deformations are intrinsic to the pseudo-cubic structure of the $RTiO_3$ system. Consequently, the deformations observed in $RTiO_3$ can not be ascribed to an orbital ordering scheme.
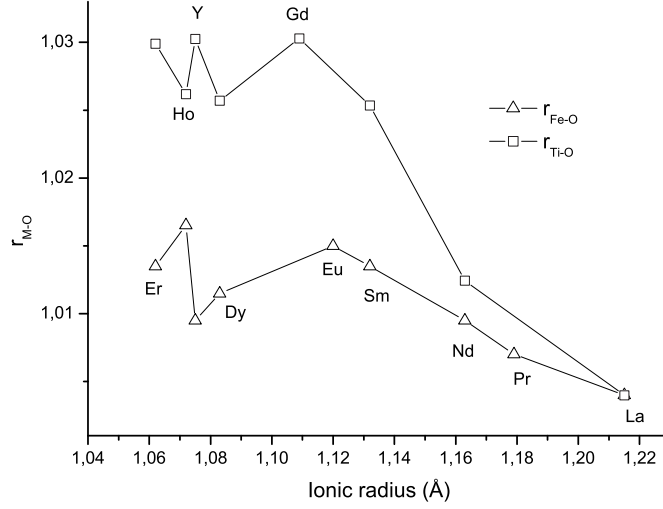
Figure 3.11: *Comparison of the distortion of the of MO₆ octahedron using the parameter r_{M-O} between the RFeO₃ and RTiO₃. We use the same parameter r_{M-O}=(Ti-Olong/Ti-Oshort) as Cwik et al. [8]. We use structural parameters reported in literature for comparison [2, 28]*

Trigonal Distortion

Starting from the ideal cubic perovskite ABO₃, which has the space-group $P\mathrm{m}\bar{3}\mathrm{m}$, it is possible to derive the space-groups of the distorted perovskites (hettotypes). These hettotypes are produced by tilts of the octahedra and limited to multiplication by 2 in any direction of the unit-cell. Based on the different possible tilting of the octahedra, Glazer identified 23 tilt systems [29] which have been reduced to 15 recently by Howard and Stokes [30]. Mochizuki *et al.* claimed that a crystal field having the symmetry D_{3d} (trigonal distortion) was sufficient to lift the degeneracy of the t_{2g} orbitals [7]. The resulting orbital state can be expressed approximately as $\frac{1}{\sqrt{3}} \times (d_{xy} + d_{yz} + d_{zx})$ which has been confirmed experimentally by NMR experiment [9]. The authors claimed that the shift of La ions creates a crystal field having a trigonal symmetry. In this picture, the crystal field due to the eight nearest La ions gives a nearly equidistant splitting scheme between the three t_{2g} orbitals which is only a first approximation. This has been pointed out by Schmitz *et al.* [31]. By taking into account the exchange Hamiltonian, Schmitz *et al.* have been able to describe better the origin of the magnetic ordering and to complete the model proposed by Mochizuki *et al.*.
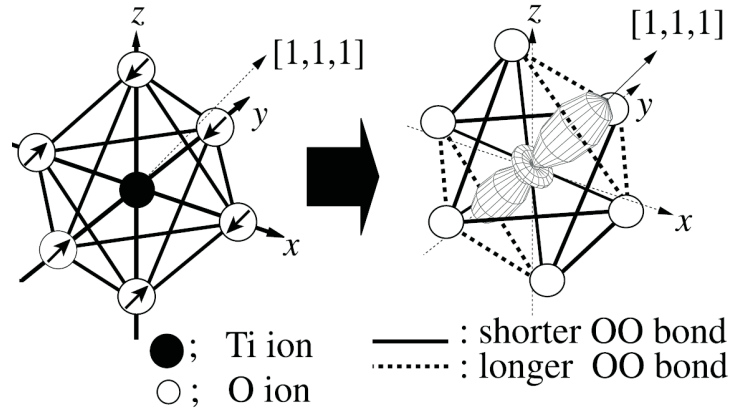
Figure 3.12: *D_{3d} type distortion responsible for the lifting of the degeneracy of the t_{2g} orbitals in RTiO$_3$ according to the scenario proposed by Mochizuki et al. [7].*

The difference in the distortion between the model elaborated by Mochizuki *et al.* and the one of Schmitz *et al.* has been ascribed to the Jahn-Teller effect present in LaTiO$_3$. However one can show that a crystal field of D$_{3d}$ symmetry on the transition metal ion site (Wyckoff position a) will not give the space-group Pnma (other setting of Pbnm) starting from Pm$\bar{3}$m, even through the corner shared octahedra network. Indeed, Howard and Stokes have shown that the distortion which gives the space-group Pnma starting from Pm$\bar{3}$m belongs to the six-dimensional reducible representation M$^{3+}\bigoplus$R^{4+}; the direct sum of M^{3+} and R^{4+} [30]. The distortions due to the IR M^{3+} are along 2-fold axis parallel to the (100) direction of Pm$\bar{3}$m. The ones due to the irreducible representation IR R^{4+} are along the 2-fold axis parallel to the (011) direction. Both distortions due to the different irreducible representations have the E$_u$ symmetry. The distortion along the (100) direction due to IR M^{3+} lowers the symmetry from O$_h$ to C$_{2v}$. The distortion due to R^{4+} along the (011) direction lowers also to C$_{2v}$. The simultaneous distortions of the two irreducible representations lower the symmetry finally to C$_s$. Consequently, we can see that the crystal field resulting from the lanthanum ion shift does not have a trigonal symmetry which would correspond to a distortion along one of the three fold axes of the O$_h$ symmetry. Consequently, one can see that the hypothesis of having a D$_{3d}$ distortion type is incorrect and it will not reduce the local symmetry of Ti to C$_s$ starting from O$_h$. However, if we consider the correct distortion pattern, one can reach the correct local symmetry of Ti. The C$_s$ crystal field does not require any nearly equidistant splitting scheme between the three t$_{2g}$ orbitals. On the other hand, if one applies a trigonal distortion on the Ti site to the Pm$\bar{3}$m symmetry, it will give rise to a trigonal distortion on the

transition metal site through the corner shared octahedra network. This trigonal distortion will lower the symmetry to R$\bar{3}$c (n°167) due to the IR R^{4+} alone [30]. However, R$\bar{3}$c is not the symmetry adopted by the RTiO$_3$ family. In other words, the Pnma symmetry of RTiO$_3$ is not due to the Jahn-Teller effect but due to rigid-unit modes which are characterized by a tilting of the oxygen octahedra rather than other effects.

3.4.3   A reduced magnetic moment

RTiO$_3$ and LaTiO$_3$ in particular have attracted attention when an ordered magnetic moment of $0.45\mu_B$ was reported [3]. This experimental value is surprisingly small for a single electron with quenched orbital moment, for which one would have expected $1\mu_B$. Cwik *et al.* were the first to notice that quantum fluctuations could explain about 15% of reduction of the magnetic moment [8, 32]. Later Schmitz *et al.* mention that this moment could be further reduced by about 14% due to on-site spin-orbit coupling leading to an overall estimate of $0.72\mu_B$ [31]. Completing the model proposed by Mochizuki *et al.* and including a Jahn-Teller distortion, they claimed that LaTiO$_3$ was orbital ordered. In addition, they could reproduce the NMR measurement of Kiyama [9]. However, it is well known that the magnetic moment is strongly correlated to the stoichiometry of the sample [19]. Cwik *et al.* reported an experimental magnetic moment of $0.57\mu_B$ which is significantly higher than the $0.45\mu_B$ reported by Meijer *et al.* [3, 8]. Moreover the reported 10% error on the measurement is not negligible [8]. In addition, it is very well known that covalency can reduce the magnetic moment due to spin transfer to the ligands of a given ion. This was already observed by Alperin in NiO [33]. The form factors for neutron are also altered by covalent effects. For instance, in LaCrO$_3$ it was reported that the spin transfer is about 5% [34]. Consequently, if one takes into account all the possible effects (crystal field, spin-orbit, quantum fluctuations, covalency) and the experimental errors, one can easily find a fair agreement between experimental and theoretical values for the magnetic moment without considering any orbital ordering. This conclusion is supported by the calculations of Radwanski and Ropka on YTiO$_3$ [35]. Using a single-ion picture and taking into account the low symmetry of the crystal they are able to reproduce the value of the magnetic moment and its characteristics without involving any orbital ordering.

3.5   Conclusions

We have investigated with high resolution X-ray diffraction the possible presence of a lowering of symmetry in LaTiO$_3$ and YTiO$_3$ resulting from an

allowed Jahn-Teller type of distortion. We show that at any temperature, the best model is given using the Pbnm space-group. Based on symmetry arguments and by comparing to very-well known non Jahn-Teller active systems, we provided evidence that the structures of $LaTiO_3$ and $YTiO_3$ do not exhibit any signature of orbital ordering. This supports the interpretation of Keimer *et al.* and of Haverkort *et al.* [4, 25] and contradicts the recent calculations by Schmitz *et al.* [31]. This work demonstrates the importance of symmetry when considering possible distortion patterns of a compound.

References

[1] A. J. Millis, B. I. Shraiman and R. Mueller, Phys. Rev. Lett. **77**, 175 (1996)

[2] M. Marezio, J. P. Remeika and P. D. Dernier, Acta Cryst. B**26**, 300 (1970)

[3] G. I. Meijer *et al.*, Phys. Rev. B **59**, 11832 (1999).

[4] B. Keimer *et al.*, Phys. Rev. Lett. **85**, 3946 (2000).

[5] G. Khaliullin and S. Maekawa, Phys. Rev. Lett. **85**, 3950(2000).

[6] K. Kikoin *et al.*, Phys. Rev. B **67**,214418 (2003).

[7] M. Mochizuki and M. Imada, J. Phys. Soc. Jpn. **70**, 2872 (2001); M. Mochizuki and M. Imada, Phys. Rev. Lett. 91, 167203 (2003).

[8] M. Cwik *et al.*, Phys. Rev. B **68**, 60401 (2003).

[9] T. Kiyama and M. Itoh, Phys. Rev. Lett. **91**, 167202 (2003).

[10] G. Khaliullin and S. Okamoto, Phys. Rev. Lett. **89**, 167201 (2002).

[11] C. Ulrich *et al.* Phys. Rev. Lett. **89**, 167202.

[12] M. Itoh *et al.*, J. Phys. Soc. Jpn. **68**, 2783 (1999).

[13] J. Akimitsu *et al.*, J. Phys. Soc. Jpn. **70**, 3475(2001).5

[14] J. Rodríguez-Carvajal, M. Hennion, F. Moussa, A. H. Moudden, L. Pinsard and A. Revcolevschi, Phys. Rev. B **57**, R3189 (1998)

[15] G. Blake *et al.* Phys. Rev. Lett. **87**, 245501 (2001)

[16] M. T. Hutchings, E. J. Samuelsen, G. Shirane and K. Hirakawa, Phys. Rev. **188**, 919 (1969)

[17] H.A.Jahn and E. Teller, Proc. R. Soc. London A, **161**, 220, (1937).

[18] T. Chatterji *et al.* Phys. Rev. B. **68**, 052406 (2003); T. Maitra, P. Thalmeier, and T. Chatterji Phys. Rev. B 69, 132417 (2004); L. Martin-Carron and A. de Andres, Eur. Phys. J. B 22, 11-16 (2001)

[19] Y.Taguchi *et al.* Phys.Rev.B **59**, 7917 (1999).

[20] A. C. Larson and R. B. Von Dreele, Los Alamos National Laboratory Report No. LAUR 86-748, 1994.

[21] D. T. Croner and D. A. Liberman, Acta Cryst. B **47**, 267 (1981)

[22] P. Bordet *et al.*, Journal of Sol. State Chem. **106**, 253 (1993)

[23] K. Tezuka *et al.*, Journal of Sol. State Chem. **141**, 404 (1998)

[24] K. Oikawa *et al.*, Journal of Sol. State Chem. **154**, 524 (2000)

[25] M. W. Haverkort *et al.*,Phys. Rev. Lett. **95**, 196404 (2005).

[26] J. Q. Yan *et al.*, Phys. rev. Lett. **93**, 235901 (2004); Y. Ren *et al.*, Phys. Rev. B **67**, 14107 (2003), F. Zhong *et al.*, Phys. Rev. Lett. **93**, 176404 (2004); A. A. Tsvetkov *et al.*, Phys. Rev. B **69**, 75110 (2004)

[27] K. Knizek *et al.*, Phys. Rev. B **73**, 214443 (2006)

[28] M. Eitel, J. E. Greedan, J. Less Com. Metals **116**, 95 (1986); J. E. Greedan J. Mag. Mag. Mat. **44**, 299 (1984); D. A. MacLean, H.-N. Ng, J. E. Greedan J. Solid State Chem. **30** 35 (1979); C. W. Turner, M. F. Collins, J. E. Greedan, J. Mag. Mag. Mat. **23**, 265 (1981); C. W. Turner, J. E. Greedan, J. Mag. Mag. Mat. **20**, 165 (1980); J. P. Goral, J. E. Greedan, J. Mag. Mag. Mat. **37**, 315 (1983); J. E. Greedan, C. W. Turner, D. A. Goodings, J. Mag. Mag. Mat. **42**, 255 (1984); C. W. Turner, J. E. Greedan, J. Solid State Chem. **34**, 207 (1980)

[29] A. M. Glazer, Acta Cryst. B **18**, 3384 (1972) and Acta Cryst. A **31**, 756 (1975)

[30] C. J. Howard and H.T. Stokes, Acta Cryst. B**54** 782 (1998)

[31] R. Schmitz, O. Entin-Wohlman, A. Aharony, A. B. Harris and E. Müller-Hartmann, Phys. Rev. B **71** 144412 (2005); R. Schmitz, O. Entin-Wohlman, A. Aharony, A. B. Harris and E. Müller-Hartmann, Phys. Rev. B **71** 214438 (2005)

[32] P. W. Anderson, Phys. Rev. **86**, 694 (1952); R. Kubo, Phys. Rev. **87**, 568 (1952)

[33] Alperin, H. A., Phys. Rev. Lett., **6**, 55 (1961)

[34] Nathans, R.; Alperin H. A., Pickart, S. J. and Brown P. J.; J. Appl. Phys. **34**, 1182 (1963)

[35] R. J. Radwanski and Z. Ropka, unpublished, cond-mat/0601005

Chapter 4

Mechanism for ferroelectricity in hexagonal RMnO$_3$

4.1 Introduction

Coexistence of ferroelectricity and magnetism presents a rapidly growing and fascinating field in solid state physics. The hexagonal manganites RMnO$_3$ exhibit such coexistence with T$_{FE}{\sim}1000$ K and T$_N{\sim}100$ K. They undergo a ferroelectric transition between a non-centrosymmetric room temperature (RT, see figure 4.1) phase and a high-temperature (HT, see figure 4.2) centrosymmetric structure. Recent studies of RMnO$_3$ show that the ferroelectric and antiferromagnetic order parameters are coupled [1, 2, 3, 4]. This allows the manipulation of electric and magnetic moments by magnetic and electric fields, respectively. While all the multiferroic compounds without lone pairs exhibit low saturation polarization [5], the hexagonal RMnO$_3$ have a high saturation polarization [6] of 5.5 μC/cm^2. In the search for new multiferroics with high performance, it is of much interest to understand the microscopic mechanisms of ordering in hexagonal RMnO$_3$.

While the interplay between electric and magnetic order in the low temperature phase is becoming clearer, the origin of the ferroelectric state is being actively debated [7, 8, 9, 10, 11, 12]. In several publications, ferroelectricity is suggested to be generated by a temperature dependent tilt of the MnO$_5$ bipyramids and a buckling of the R-layers. Over the years, reports on YMnO$_3$ mention several critical temperatures (see section 4.2 for a review). The ferroelectric transition temperature (T$_{FE}$) has been consistently reported near 930K by various authors [7, 8, 13]. Another even higher transition has been identified as a tripling of the unit-cell around 1270K [7]. However, recent diffraction experiments up to 1000 K did not observe any phase transition [9]. Due to the different nature of the two transitions, few studies have linked them to understand the onset of ferroelectricity [9, 14]. Moreover, the existence of a possible intermediate phase

(IP) has been questioned due to contradicting results.

In this chapter, we study the mechanism of ferroelectricity in YMnO$_3$, which we consider as a typical example for the entire hexagonal RMnO$_3$ family. We start by giving a literature overview of the subject referring to previous studies. Prior to any experimental work, we have carried out group theoretical analysis in order to design more adequately our experiments. Based on this analysis and the literature results, we expect the existence of an intermediate phase (IP). This IP should exist within a temperature range defined by T$_{C1}$ and T$_{C2}$. Consequently, we have carried out several powder neutron and synchrotron diffraction experiments. Both kinds of experiments show a clear transition towards the HT phase at T$_{C2}$ and the neutron experiment indicates an IP. We made further investigations with single crystals instead of powder samples. We were able to demonstrate the existence of an IP in a single experiment by means of synchrotron diffraction, DTA and TMA on a single crystal. These results confirm the indications for an IP observed in powder neutron data. The powder neutron data indicate a ferroelectric state of the IP. In contrast, band structure calculations show that the IP is likely paraelectric, in contradiction with previous analysis [10, 11] and our powder neutron results (see section 4.5).

In figure 4.1, we present the ferroelectric structure of YMnO$_3$ at RT. The structure can be described by layers of edge-sharing trigonal bipyramids of oxygen surrounding Mn atoms. These layers are separated by layers of Y. The rare-earth atoms have a non-conventional 7-fold coordination. A cooperative buckling of the MnO$_5$ trigonal bipyramids below T$_{FE}$ displaces the Y^{3+} ions along the c axis giving rise to a ferrielectric state. The atomic coordinates are presented in table 4.1. The cell parameters are $a = 6.1387$Å and $c = 11.4071$Å.
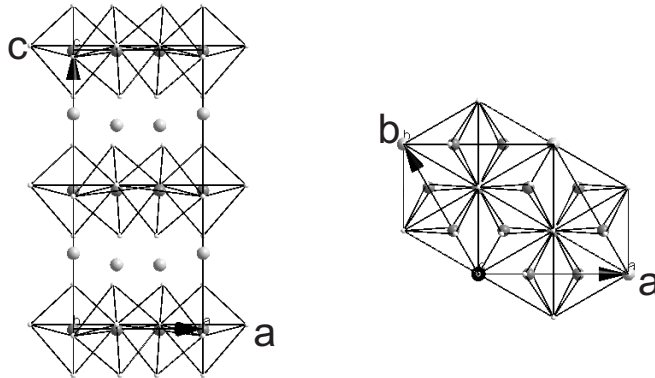

Figure 4.1: *Crystal structure of YMnO$_3$ at room temperature. Mn ions are in black, Y atoms in light grey and the oxygens in white.*

P6₃cm RT≤T_{C1}		
Atoms	Wyckoff positions	(x,y,z)
R_1	2a	(0,0,0.7802)
R_2	4b	(1/3, 2/3,0.7148)
Mn	6c	(0.6672,0,0.49760)
O_{11}	2a	(0,0,0.9730)
O_{12}	4b	(1/3,2/3,0.5150)
O_{21}	6c	(0.6975,0,0.6611)
O_{22}	6c	(0.3530,0,0.8352)

Table 4.1: *Atomic coordinates of YMnO₃ in the ferroelectric space group P6₃cm (n° 185) as observed at RT below T_{C1} according to ref. [15]. The cell parameters are a = 6.1387Å and c = 11.4071Å at RT.*

In the HT paraelectric phase, the lattice parameter a is reduced by a factor of $\sqrt{3}$. The resulting lattice parameters are $a_{HT} \sim a_{FE}/\sqrt{3} = 3.61$Å and $c_{HT} \sim c_{FE} = 11.39$Å [7]. The atomic positions are given in table 4.2 and a representation of the structure is presented in figure 4.2.

P6₃/mmc T≥T_{C2}		
Atoms	Wyckoff positions	(x,y,z)
R	2a	(0,0,0)
Mn	2d	(1/3, 2/3, 1/4)
O_1	2b	(0, 0, 1/4)
O_2	4f	(1/3, 2/3, 0.083)

Table 4.2: *Atomic coordinates of YMnO₃ in the paraelectric space group P6₃/mmc (n° 194) as observed above T_{C2} adapted from ref. [7]. The cell parameters are $a_{FE}/\sqrt{3} = 3.61$Å and $c_{HT} \sim c_{FE} = 11.39$Å at T≃1273K.*
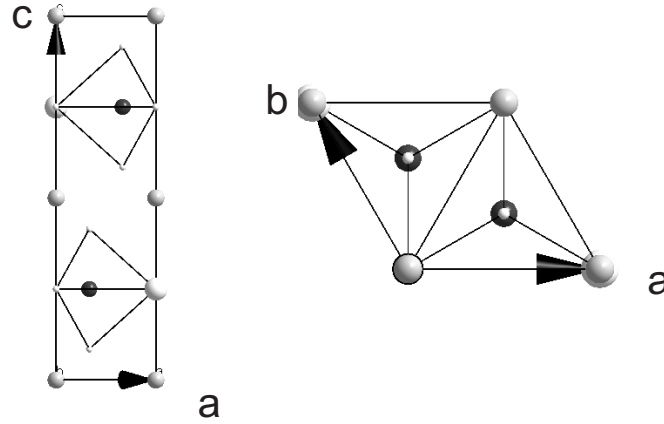
Figure 4.2: *Crystal structure of YMnO$_3$ at high temperature. Mn ions are in black, Y atoms in light grey and oxygens in white.*

4.2   Historical perspective

Bertaut and coworkers [16] were the first to discover ferroelectricity in several compounds of the hexagonal RMnO$_3$ family (R = Er, Lu and Y). They measured the P-E hysteresis and polarization on a single crystal grown from Bi$_2$O$_3$ flux. The same year, Bokov *et al.* confirmed the observations of Bertaut *et al.* and measured the magnetic properties down to 77K of a single crystal of R = Y and Yb also grown from Bi$_2$O$_3$ flux. They were the first to mention the antiferromagnetic order of these compounds [17]. They reported a saturated polarization at room temperature of 5.5μC/cm^2. One year later, Smolenskii *et al.* confirmed the ferroelectricity and the antiferromagnetic ordering of the Mn^{3+} spins of YMnO$_3$ and YbMnO$_3$ [18]. They also report that no ferroelectric transition could be observed below 823K. They also grew their single crystals from a Bi$_2$O$_3$ flux.

The first experimental observation of the ferroelectric transition in YMnO$_3$ was the work of Ismailzade and Kizhaev [8]. They reported the pyroelectric current of single crystals of YMnO$_3$ and YbMnO$_3$. They observed a peak in these measurements at 933K and 973-998K respectively. These observations were confirmed by anomalies in the cell parameters at 933K for YMnO$_3$ and at 998K for YbMnO$_3$. However, the temperature dependence of the cell parameters is different from all later reports. In addition, they observed anomalies in the thermal expansion at 498K and 623K for YMnO$_3$ and YbMnO$_3$, respectively. Also these observations were never reproduced in later reports. The single crystals were also grown from Bi$_2$O$_3$ flux. They were the first to propose P6$_3$/mcm symmetry for the phase above the ferroelectric transition. However they did not provide any evidence. Soon afterwards, Peuzin *et al.* reported a dielectric constant of 20 on YMnO$_3$

single crystal [6]. The dielectric constants and $\tan(\delta)$ were independent of frequency between 50Hz and 50MHz for their crystals. Moreover they found that the resistivity of $YMnO_3$ followed an Arrhenius law with an activation energy of 1.4eV between room temperature and 923K. Coeure *et al.* have reported a ferroelectric transition at 913K in $YMnO_3$ confirming the results of Ismailzade and Kizhaev [13]. Much later, Lukaszewicz and Karut-Kalicinska investigated $YMnO_3$ by high temperature single crystal X-ray diffraction. They reported in the region 893-953K small anomalies in the lattice constants that they ascribed to the ferroelectric phase transition [7]. In addition, they observed a change in symmetry to the space group $P6_3/mmc$ for T>1273K. However they failed to refine their data below 1273K with the $P6_3/mcm$ symmetry proposed earlier by Ismailzade. We notice from this literature review that there have been reports of two different transition temperatures. However these two phase transitions have never been observed in a single experiment, questioning the existence of an IP. Moreover it was consistently reported that the ferroelectric transition of $YMnO_3$ is at 933K. This is in contrast to the interpretation of the literature by Abrahams who claims that the literature is not consistent [19]. However, the symmetry of the intermediate phase (IP) has not been established.

In recent years, two structural studies have been carried out in the high temperature regime either by synchrotron or neutron diffraction on hexagonal $RMnO_3$ powder [9, 11]. Both experiments failed to observe any structural phase transitions even though they measured up to 1000K for R = Y (synchrotron), up to 1300K for Lu, 1100K for Yb and 1400K for Tm (neutron). Lonkai *et al.* realized the necessity for two high temperature phase transitions, based on symmetry arguments [11]. Therefore, they proposed an antiferroelectric IP having the same symmetry as the room temperature phase. Moreover, recent calculations by Fennie *et al.* [12] suggest that the IP would have $P6_3cm$ symmetry, however with a finite polarization.

The absence of observation of any phase transitions in these two recent studies, contradicting older results, caused confusion. The aim of this chapter is three-fold: first using group theory to investigate the possible nature of the IP, second to demonstrate experimentally the existence of an IP (section 4.6), third to give insight into the nature of the IP and consequently the mechanism of ferroelectricity (sections 4.3, 4.7 and 4.8). Finally, we discuss the differences between powder and single-crystal experiments which could justify the different results in the high temperature regime of hexagonal $RMnO_3$ (sections 4.5 and 4.8).

4.3   Contribution of group theory

4.3.1   Introduction

As stated in the introduction and from the literature, we expect two phase transitions. However, we were not the first ones to investigate the possible different phases by means of group theory. Lonkai *et al.* also pointed out that two separate phase transitions are expected in the transition from the HT phase (P6$_3$/mmc) to the RT phase (P6$_3$cm) [11]. Using the program ISOTROPY (for more details, see ref. [11, 20, 21]), we derive four possible pathways from the high temperature (HT) phase to the RT phase via an IP as shown in table 4.3. These results are the same as those of Lonkai *et al.* [11]. We indicate in table 4.3 the physical meaning of the different irreducible representations (IR's). We pass through two critical temperatures T$_{C1}$ and T$_{C2}$ going from RT to HT. However, we notice that 2 transitions are not necessary from group theoretical arguments to reach the RT phase from the HT one. A single IR K$_3$ could be the active IR giving rise to a single transition.

   The space groups P6$_3$/mmc and P6$_3$mc can be excluded for the IP because these pathways involve a tripling of the unit cell only at T$_{C1}$, in disagreement with the experimental observations [7]. Lonkai *et al.* excluded P6$_3$/mcm as IP because they claimed that the corresponding order parameter generates only tiny additional peaks to the diffractogram indexed by P6$_3$/mmc and would be nearly impossible to detect at T>1000K. Thus they conclude that the IP should have space group P6$_3$cm with an antiferroelectric nature (see figure 8 of ref [11]). While in practice it may be difficult to distinguish between P6$_3$/mcm and P6$_3$/mmc, it is not a sufficient reason to disregard the possibility of having an IP with P6$_3$/mcm.

P6$_3$/mmc			
Γ$_1^+$(strain)	K$_1$(tripling)	K$_3$ (tripling)	Γ$_2^-$ (Polarization)
P6$_3$/mmc	**P6$_3$/mcm**	**P6$_3$cm**	**P6$_3$mc**
K$_3$ (tripling)	Γ$_2^-$ (Polarization)	Γ$_1$ (strain + polarization)	K$_1$(tripling)
P6$_3$cm			

Table 4.3: *Description of all group-theoretically allowed phase transitions from P6$_3$/mmc to P6$_3$cm with one intermediate phase. Only the primary order parameters are displayed. The associated wave vectors **k** are Γ$_i^j$ (**k** = 0, 0, 0) and K$_i$ (**k**= 1/3,1/3,0).*

   In this section, we will investigate the main differences between P6$_3$/mcm

and P6$_3$cm for the IP. First of all, we will show that group theory allows P6$_3$cm as an IP but that it cannot be antiferroelectric. This is in opposition to the statement of Lonkai *et al.* [11]. In addition, we will show that in the case that the IP has the symmetry P6$_3$/mcm, a transition of 2nd order character is possible through a Landau critical point starting from P6$_3$/mmc. Contrary to Lonkai *et al.* [11], we do not consider only the primary order parameters. A full analysis should include coupling to all symmetry-allowed secondary order parameters. This is the approach that we took.

4.3.2 Possibility of an antiferroelectric intermediate phase

The space group P6$_3$cm does not contain an inversion center. In order to generate zero-polarization, as observed experimentally, Lonkai *et al.* assume the IP to be antiferroelectric. We investigated this possibility using an analysis similar to that of Stokes and Hatch for BaAl$_2$O$_4$ [22]. Four IR's are involved in the transition from P6$_3$/mmc to P6$_3$cm. Γ_1^+, Γ_2^-, K$_1$ and K$_3$ IRs lead to P6$_3$cm. This result was found also by Fennie *et al.* [12]. This means that the atomic displacements from the transition can be decomposed into four modes which have the symmetry of these IR's (for a method see ref. [21]). In the paraelectric state, these modes are vibrational modes centered at the equilibrium positions. We associate the transition with the order parameters η_1, η_2, η_3, and η_4, corresponding to the time averaged displacement of the IR's K$_3$, Γ_1^+, Γ_2^-, K$_1$, respectively. Normally, η_1 and η_4 order parameters are 2-dimensional (K$_3$→η_1=(η_{1x},η_{1y}) and K$_1$→η_4=(η_{4x},η_{4y})) while η_2 and η_3 are monodimensional. However, we fixed the direction of the order parameter such that K$_3$ gives rise to P6$_3$cm [η_1=(η_{1x},0)] and K$_1$ gives rise to P6$_3$/mcm [η_4=(η_{4x},0)]. Thus, the primary order parameter η_1, associated with the K$_3$ mode transforms P6$_3$/mmc to P6$_3$cm, whereas the secondary order parameters η_2, η_3, and η_4 transform P6$_3$/mmc to P6$_3$/mmc (n°194), P6$_3$mc (n°186) (without tripling of the cell) and P6$_3$/mcm (n°193), respectively. Using symmetry considerations, we can find an expression for the free energy as a function of the order parameters [20]:

$$
\begin{aligned}
F = F_0 &+ F_{12}\eta_1^2 + F_{14}\eta_1^4 + F_{22}\eta_2^2 + F_{23}\eta_2^3 + \\
&F_{24}\eta_2^4 + F_{32}\eta_3^2 + F_{34}\eta_3^4 + F_{42}\eta_4^2 + F_{43}\eta_4^3 + \\
&F_{44}\eta_4^4 + A_{12}\eta_1^2\eta_2 + A_{13}\eta_1^3\eta_3 + A_{14}\eta_1^2\eta_4
\end{aligned}
\tag{4.1}
$$

The expansion is limited to terms up to the fourth order, and we include only coupling terms which are linear in the secondary order parameter. At the transition, the coefficient F$_{12}$ becomes negative, and the minimum of F occurs for a non-zero value of η_1 as shown by equations 4.2 and 4.3.

$$\frac{\partial F}{\partial \eta_1} = 2F_{12}\eta_1 + 4F_{14}\eta_1^3 + 2A_{12}\eta_1\eta2 + 3A_{13}\eta_1^2\eta_3$$

$$= 2\eta_1(F_{12} + 2F_{14}\eta_1^2 + A_{12}\eta_2 + \frac{3}{2}A_{13}\eta_3\eta_1) \tag{4.2}$$

However, the coupling terms are linear in η_2, η_3, and η_4 as shown in eqn. 4.1 and their contribution to the free energy becomes nonzero as well. In particular, through the coupling term $A_{13}\eta_1^3\eta_3$ the polar IR Γ_2^- becomes finite, and will generate a finite polarization (see equation 4.3).

$$\frac{\partial F}{\partial \eta_3} = 2F_{32}\eta_3 + 4F_{34}\eta_3^3 + A_{13}\eta_1^3 \tag{4.3}$$

Consequently, we see that in the hypothesis that the IP has the P6$_3$cm symmetry, this IP cannot be antiferroelectric (the polarization is non-zero). In addition, this result would oppose the usual interpretation of Ismailzade *et al.* (polarization non-zero above T$_{C1}$) [8]. Furthermore, the ferroelectric transition at T$_{C1}$ would be isosymmetric, driven by the Γ_1 IR, and should thus be of first-order character as observed for *P*nma perovskites [23], for which we find no experimental support. Finally, in this model the ferroelectricity would be driven by a secondary order parameter, and YMnO$_3$ would then be an improper ferroelectric. Improper ferroelectrics exhibit a saturation polarization that is much smaller than for proper ferroelectrics. BaAl$_2$O$_4$ (P$_S$~0.08 μC/cm^2) [22], Mg$_3$B$_7$O$_{13}$Cl (P$_S$~0.08 μC/cm^2) [24] and Tl$_2$Cd$_2$(SO$_4$)$_3$ (P$_S$~0.07μC/cm^2) [25] have significantly smaller polarization than YMnO$_3$ (P$_S$~5.5μC/cm^2) [6]. Based on symmetry arguments, we have demonstrated that the IP cannot be antiferroelectric.We will next investigate the possibility of a paraelectric IP and its consequences.

4.3.3   Possibility of a paraelectric intermediate phase

Order parameters involved

The other possibility for the intermediate phase is a paraelectric phase with the space group P6$_3$/mcm from literature (see section 4.2). Still, using the group theoretical approach, we can also investigate what are the secondary order parameters involved in the different steps of the two phase transitions towards the ferroelectric RT structure. For the first step, we have the IRs K$_1$ and Γ_1^+ which lead to P6$_3$/mcm. On further cooling, going from P6$_3$/mcm to P6$_3$cm, P6$_3$cm is obtained by the Γ_2^- and Γ_1^+ IRs.

The mode Γ_1^+ going from P6$_3$/mmc to P6$_3$/mcm is a strain mode without polarization component and the same remark holds for the Γ_1^+ IR involved between P6$_3$/mcm and P6$_3$cm. Consequently, in this case the present modes would be consecutively K$_1$ and some strain followed by a polar mode Γ_2^-.

We see that in this hypothesis, there are no contradictions with any experimental observations. We shall see in the next section the relationships between the different modes of the different symmetries. In particular, we will discuss the differences between our work and the work of Fennie *et al.* [12].

Symmetry-adapted mode decomposition

In order to determine what is the difference in terms of the strength of the different modes in the two possible scenarios ($P6_3cm$ vs $P6_3/mcm$ for the IP), we have done a study of the splitting of the Wyckoff positions. The results of this study are given in table 4.4.

HT	IP	RT
$P6_3/mmc$	$P6_3/mcm$	$P6_3cm$
Y (D_{3d})	Y_1 (D_{3d})	Y_1 (C_{3v})
	Y_2 (D_3)	Y_2(C_3)
Mn (D_{3h})	Mn (C_{2v})	Mn (C_s)
O_1	O_{11}	O_{11}
	O_{12}	O_{12}
O_2	O_2	O_{21}
		O_{22}

Table 4.4: *Relations between the different atoms in the different symmetries. In brackets, we indicate the local symmetry of the metal atoms.*

In order to express the strength of the different symmetry-adapted modes, using the method proposed by Aroyo and Perez-Mato, we have to express the atomic coordinates for the case of a paraelectric IP [21]. Using symmetry adapted mode decomposition and the program SYMMODE [26], we have derived the atomic coordinates in $P6_3/mcm$ symmetry (for more information on the derivation, see Appendix A). The atomic coordinates are presented in table 4.5. The symmetry-adapted mode decompositions for $P6_3/mcm$ and $P6_3cm$ are presented in tables 4.6 and 4.7.

According to subsection 4.3.3, the results may seem in contradiction with the first principles calculations of Fennie and Rabe [12]. We will show that this is not the case. First of all, Fennie *et al.* found that the main distortion mode is K_3 and not K_1 as in the hypothesis of a proper ferroelectric mechanism. However one needs to be precise with the different notations since as soon as we take into account a K type distortion, the labelling related to the nodes of the Brillouin zone will change. Using the Frobenius theorem [27] and the program CORREL [28], we can show that:

$$(K_3 \downarrow P6_3/mcm) = \Gamma_2^- \quad and \quad (\Gamma_2^- \downarrow P6_3/mcm) = \Gamma_2^- \qquad (4.4)$$

P6$_3$/mcm		
Atoms	Wyckoff positions	(x,y,z)
R$_1$	2b	(0,0,0)
R$_2$	4d	(1/3, 2/3, 0)
Mn	6g	(0.3352,0,1/4)
O$_{11}$	2a	(0, 0, 1/4)
O$_{12}$	4c	(1/3, 2/3, 1/4)
O$_2$	12k	(0.3335, 0, 0.08725)

Table 4.5: *Atomic coordinates of YMnO$_3$ in the paraelectric space group P6$_3$/mcm (n° 193) derived by symmetry-adapted mode decomposition from the room temperature phase P6$_3$cm using the data of Aken* et al. *[15].*

P6$_3$/mcm		
Atoms	Wyckoff positions	K$_1$ (Amplitude in Å)
R$_1$	2b	0
R$_2$	4d	0
Mn	6g	-0.0133//[100] and -0.00311//[010]
O$_{11}$	2a	0
O$_{12}$	4c	0
O$_2$	12k	-0.00413//[100] and -0.0292//[010]

Table 4.6: *Decomposition of P6$_3$/mcm atomic displacements into symmetry-adapted modes of prototype P6$_3$/mmc.*

These two expressions 4.4 and 4.4 mean that the K$_3$ mode in the P6$_3$/mmc symmetry becomes Γ_2^- in P6$_3$/mcm symmetry. The same remark holds for the Γ_2^- mode of the P6$_3$/mmc symmetry. For the same reasons, the K$_1$ mode in P6$_3$/mmc becomes Γ_1^+ in P6$_3$/mcm. Consequently, if one looks at the distortions going from P6$_3$/mmc to P6$_3$cm, the main distortion is due to K$_3$ of P6$_3$/mmc symmetry. However if we assume an IP with P6$_3$/mcm symmetry, the K$_3$ and Γ_2^- of P6$_3$/mmc become Γ_2^- of P6$_3$/mcm and their displacements add up. Thus the Γ_2^- mode of P6$_3$/mcm is the primary order parameter going from P6$_3$/mcm to P6$_3$cm. For similar reasons, the K$_1$-type distortion is the primary order parameter going from P6$_3$/mmc to P6$_3$/mcm. In other words, the apparent improper mechanism of ferroelectricity can be reinterpreted by a proper mechanism if the hypothesis of a paraelectric IP is considered.[1]

---

[1] The big amplitude that has the K$_3$ mode in the description of Fennie and Rabe [12] becomes part of the Γ_2^- mode relating P6$_3$/mcm to P6$_3$cm. However, as this part of the Γ_2^- mode can be explained as a K$_3$ distortion type from the P6$_3$/mmc structure, it can not produce a spontaneous polarization. In other words, the transition sequence K$_1$ plus Γ_2^- does not explain a larger polarization than in the scenario of Fennie and Rabe.

P6$_3$cm		
Atoms	Wyckoff positions	Γ_2^- (Amplitude in Å//[001])
R$_1$	2b	0.297
R$_2$	4d	-0.1679
Mn	6g	0.0203
O$_{11}$	4c	0.269
O$_{12}$	12k	-0.192
O$_{21}$	6c	0.0197
O$_{22}$	6c	0.0197

Table 4.7: *Decomposition of P6$_3$cm atomic displacements into symmetry-adapted modes of prototype P6$_3$/mcm.*

If there is a paraelectric IP, K$_1$ should be unstable starting from P6$_3$/mmc. However, Fennie and Rabe found that it is the K$_3$ mode which is unstable instead of the K$_1$ mode. This observation would rule out the hypothesis of a paraelectric IP since it is the K$_1$ mode which should give rise to this symmetry. But the calculations have been done at 0K. The typical assumption is that the negative (unstable) like the positive (stable) frequencies become more and more positive with temperature. This is the usual temperature dependence. Nevertheless, it is not always the case, for instance for reentrant ferroelectrics. If one carries out calculations from the prototypic phase to the RT phase, one will never find instabilities of any mode despite the fact that a ferroelectric IP exists [29]. These considerations illustrate that we cannot exclude the existence of a paraelectric IP based on zero-temperature calculations alone. We notice that our calculations and considerations are not in contradiction with the calculations of Fennie and Rabe, nor with the experimental reports (see section 4.2). Moreover, one should notice that the displacements of Mn and O$_2$ atoms in table 4.6 are particularly small between the HT phase and IP. Thus, it might be understandable that Fennie *et al.* found the K$_3$ mode unstable rather than the K$_1$ mode. Moreover, it means that the existence of an IP with P6$_3$/mcm symmetry will have little influence on the magnitude of the polarization but a significant effect on the mechanism of ferroelectricity. In addition, such small displacements from the ideal positions could be difficult to probe experimentally at temperatures above 1000K.

Landau Theory

Another insight given by group theory when coupled to Landau theory is the possible phases for a given HT phase and a given IR. The Landau theory gives information about the different phases and how they are related to each other (2nd or 1st order transition, tricritical points, Landau critical

points, etc.).

We would like here to investigate the transition at T$_{C2}$ in the hypothesis going from P6$_3$/mmc to P6$_3$/mcm or more generally to consider the transition starting from P6$_3$/mmc associated with the IR K$_1$. With each IR, we can associate a set of matrices M(g$_i$). For a given representation, the representation can be faithful or not (see Representation of a group in chapter 2). More generally, the representation will not be faithful. Among the M(g$_i$) defining a representation of **G**, the set of distinct matrices will form what we call the image I of **G**. It has been shown that the action of **G** on the order parameter space is effected by means of the elements of its image I [30]. Hence once the order parameter symmetry and the related image I are known, it is possible solely on the basis of this knowledge to determine the form of the free energy and to work out the possible symmetries of the low symmetry phase.

For the IR K$_1$, we can calculate the image of P6$_3$/mmc using the program ISOTROPY [20]. The image of P6$_3$/mmc associated with the IR K$_1$ is C$_{3v}$. The order parameter dimension in that case is n = 2 where $\eta = (\eta_1, \eta_2)$. It is generally more convenient to work using polar coordinates (ρ, ϕ) in the plane of the 2 order parameter components (η_1, η_2). We will use $\eta_1 = \rho\cos(\phi)$ and $\eta_2 = \rho\sin(\phi)$.

When a cubic invariant of the order parameter is allowed by symmetry in the Landau potential, the transition cannot be continuous, except for isolated points in the phase diagram, where the coefficient of the cubic term vanishes accidentally. For our case, a cubic invariant is allowed in the image C$_{3v}$. Thus, we will have a non-continuous phase transition (1st order). The phase diagram associated with the 2-dimensional image C$_{3v}$ was discussed in the literature [30, 31]. The full rational basis of invariants is in this case:

$$I_1 = \rho^2 = \eta_1^2 + \eta_2^2 \quad and \quad I_2 = \rho^3 cos(3\phi) = \eta_1^3 - 3\eta_1\eta_2^2 \qquad (4.5)$$

The more complete phase diagram is obtained by considering the sixth order expansion:

$$F = \alpha_1 I_1 + \alpha_2 I_1^2 + \alpha_3 I_1^3 + \beta_1 I_2 + \beta_2 I_2^2 + \gamma I_1 I_2 \qquad (4.6)$$

Using the polar coordinates, we have:

$$F = \alpha_1\rho^2 + \alpha_2\rho^4 + \alpha_3\rho^6 + \beta_1\rho^3 cos(3\phi) + \beta_2\rho^6 cos^2(3\phi) + \gamma\rho^5 cos(3\phi) \quad (4.7)$$

The minimization of F gives rise to the following equations:

$$F_1 = \frac{\partial F}{\partial I_1} = \alpha_1 + 2\alpha_2 I_1 + 3\alpha_3 I_1^2 + \gamma I_2$$
$$= \alpha_1 + 2\alpha_2\rho^2 + 3\alpha_3\rho^4 + \gamma\rho^3 cos(3\phi) \qquad (4.8)$$

and

$$F_2 = \frac{\partial F}{\partial I_2} = \beta_1 + 2\beta_2 I_2 + \gamma I_1$$
$$= \beta_1 + 2\beta_2 \rho^3 cos(3\phi) + \gamma\rho^2 \tag{4.9}$$

Using equations 4.8 and 4.9, we can show that the minima of the free energy are defined by:

$$\frac{\partial F}{\partial \rho} = \rho[2F_1 + 3\rho cos(3\phi)F_2] \tag{4.10}$$

and

$$\frac{\partial F}{\partial \phi} = -3\rho^3 sin(3\phi)F_2 \tag{4.11}$$

The first solution of the equations 4.10 and 4.11 corresponds to $\rho=0$. We will call this phase, phase 0 and it corresponds to the high temperature phase, P6$_3$/mmc ($\eta=0$). The second solution of the system is given for $sin(3\phi)=0$. If $sin(3\phi)=0$, then $\eta=(\eta_1,0)$. This solution corresponds to phases I and II which are isostructural and differ only by the sign of η_1 [30, 31]. They are associated with the extremum condition:

$$2\alpha_1 + 3\beta_1\eta_1 + 4\alpha_2\eta_1^2 + 5\gamma\eta_1^3 + 6(\alpha_3 + \beta_2)\eta_1^4 = 0 \tag{4.12}$$

Phases I and II are characterized by a group of symmetry of index 3 [30, 31]. Using the program ISOTROPY [20], we can look at the space group associated with the direction of the order parameter $\eta = (\eta_1, 0)$. We find that the space group is P6$_3$/mcm. Moreover it is effectively a space group of index 3 with respect to the high temperature phase (0) (P6$_3$/mmc). Using the stability conditions $\frac{\partial^2 F}{\partial \rho^2} \geq 0$ and $(\frac{\partial^2 F}{\partial \rho^2})^2$-$(\frac{\partial^2 F}{\partial \rho\partial\phi})^2 \geq 0$ in the limit $\eta \rightarrow 0$ for phases I and II, we find contradictory inequalities F$_2$ ≤ 0 and F$_2$ ≥ 0 [30, 31]. This fact expresses that the transitions 0-I and 0-II can be second order only at the Landau critical point defined by $\alpha_1=0$ and $\beta_1=0$. We call this point, the L point (see figure 4.3).

The last solution of the system defined by equations 4.10 and 4.11 is the case F$_1$=F$_2$=0. This solution corresponds to $\eta_1 \neq 0$, $\eta_2 \neq 0$. Using the program ISOTROPY [20], we look at the order parameter direction $\eta = (\eta_1, \eta_2)$ in order to determine the space group. We find that the space group corresponding to the order parameter $\eta = (\eta_1, \eta_2)$ is *P*-62c.

The different stability boundaries of the different phases are quite complicated and will not be discussed here. We refer the reader to the literature for more details [30, 31]. Using the results above and in the literature, we show in figure 4.3 the phase diagram corresponding to the image C$_{3v}$ of the space group P6$_3$/mmc.
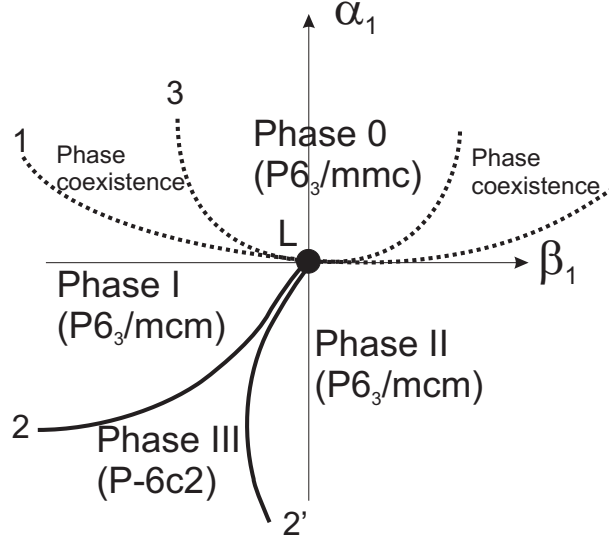
Figure 4.3: *Phase diagram corresponding to the image C_{3v} of the space group $P6_3/mmc$ associated with the IR K_1. Lines 1 and 3 are first-order transition lines. Lines 2 and 2$'$ are second-order transition lines. L is the Landau critical point allowing a second-order phase transition between $P6_3/mmc$ and $P6_3/mcm$.*

4.3.4   Conclusion

Using group theory, we have been able to reduce the number of the possible phases for the IP down to two. In addition, we have demonstrated that in contrast to the statement of Lonkai *et al.* [11], the IP cannot be antiferroelectric.[2]Moreover, we have demonstrated that the calculations of Fennie and Rabe [12] are not in contradiction with the scenario for a paraelectric IP due to the small deviations in the IP from the ideal positions. In the hypothesis of a paraelectric IP with $P6_3/mcm$ symmetry, we have predicted that the transition should be of 1st order character except at the Landau critical point L (see figure 4.3) where the transition can be of 2nd order. This will be of help in the experimental approach that we have carried out in order to give insight into the nature of the IP.

---

[2] While strictly speaking this statement is true, one can ask a question about the strength of the coupling and thus of the possibility to distinguish experimentally between the two states. In addition, we may wonder about the accuracy of the measurements of the pyroelectric current (measurement reported in ref. [8] at high temperature) considering that the conductivity increases with temperature.

4.4 Experimental Techniques

4.4.1 Sample preparation

Single crystal

$YMnO_3$ powder was synthesized by reacting stoichiometric amounts of Y_2O_3 (4N) and MnO_2 (3N metal basis) in nitrogen atmosphere at 1200°C for 10h. The powder was reground and resintered once under the same conditions to improve crystallinity. A single crystal was grown from the powder in air with additional 0.5 bar of oxygen by the Floating Zone technique using a four mirror furnace. The crystallinity of the crystal was checked by Laue diffraction. The high quality of the crystal is further evidenced by narrow X-ray diffraction peaks (FWHM∼0.012° at RT). Figure 4.4 shows a typical crystal grown by the Floating Zone technique.

Figure 4.4: *Single crystal of YMnO₃ grown by the Floating Zone technique.*

Powder sample

$YMnO_3$ powder was synthesized by reacting stoichiometric amounts of Y_2O_3 (4N) and MnO_2 (3N metal basis) in air at 1200°C with intermediate grinding until reaching an X-ray pure phase.

4.4.2 Neutron experiment

For preliminary measurements we have carried out high temperature powder neutron diffraction at the JEEP II reactor (Kjeller, Norway) with the PUS instrument. The wavelength was 1.5554 Å. The sample was kept in a silica-glass tube of 6 mm in diameter in a furnace (hot air blower). Due to the low flux of neutrons available, we have concentrated on a short d-spacing range. We could collect additional data sets using the high resolution instrument HRPD at ISIS (Didcot, England). The difference between the two experiments is that the instrument HRPD is based on the Time of

flight technique and has a higher flux and resolution. This allows a much quicker data collection. During this experiment, the sample was held in a quartz tube at ambient pressure or evacuated. This encapsulation reduces the amount of vacancies and prevents the sample from decomposition. We note that previously reported neutron experiments have been performed in dynamic vacuum in a vanadium container eventually giving rise to a partial decomposition of the sample [11, 32]. The GSAS software package has been used to treat the data [33].

4.4.3   X-ray experiments

Powder sample

We have carried out an additional high temperature synchrotron X-ray experiment on the beamline ID31 at ESRF (Grenoble, France) using a wavelength of 0.3 Å. The powder sample was placed in a Pt capillary which was spinning to improve the statistics. The Pt capillary was heated by means of a three mirror furnace. The temperature control was monitored by the position of the Pt peaks with a feedback system to compensate the aging of the lamps. In figure 4.5, we show a schematic picture of the furnace.
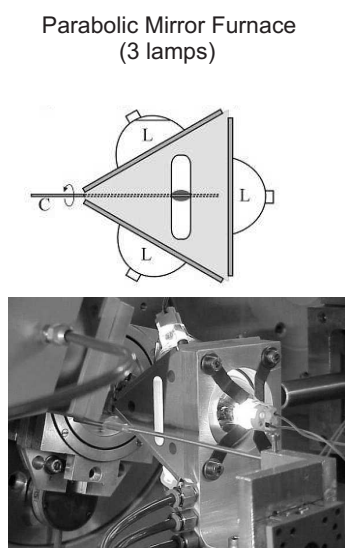

Figure 4.5: *Schematic picture of the mirror furnace used at ESRF on ID31.*

Single crystal

Prior to temperature dependent experiments, we have investigated the quality of our single crystal from the as-grown boule (see figure 4.4) by means of laboratory X-ray diffraction. A black colored crystal extracted from the

grown boule with the approximative dimensions of 0.14×0.12×0.04 mm was mounted on a Bruker SMART APEX CCD diffractometer (Platform with full three-circle goniometer). Intensity measurements were performed using graphite monochromated Mo-K$_\alpha$ radiation. The final unit cell was obtained from the xyz centroids of 1743 reflections after integration. Intensity data were corrected for Lorentz and polarization effects, scale variation, for decay and absorption: a multi-scan absorption correction was applied, based on the intensities of symmetry-related reflections measured at different angular settings (SADABS)[34], and reduced to F$^2_{obs}$. The program suite SHELXTL was used for space group determination assuming an inversion twin [35].

High temperature synchrotron X-ray diffraction experiments were performed on beamline BESSRC-11-ID-C at the Advanced Photon Source (Argonne National Laboratory, Chicago) using a wavelength of 10.772 pm. The oriented single crystal was heated in air using a four mirror furnace. Once more, we note that experiments by other groups were performed in vacuum, which may result in off-stoichiometry or even partial decomposition of the sample. The data were analyzed using the FIT2D program [36] to convert our image plate data to a 2D powder pattern, and then by the GSAS software package [33].

4.4.4 Differential Thermal Analysis

Differential thermal analysis was carried out in a flow of nitrogen using TA Instruments - SDT 2960 apparatus. The temperature ramp was 5K/min. We have used a crushed single crystal for this experiment in a platinum pan.

4.4.5 Thermomechanical analysis

The dilatometric measurements (Thermomechanical analysis, TMA) were carried out in static air using a SETARAM TMA92 dilatometer. The temperature ramps were 1 K/min with a dwell at 1473 K for half an hour. A load of 10 g was applied to optimize the signal to noise ratio. The choice of this slight load is based on several trial runs. The single crystal (SC) sample was protected from the alumina parts (see figure 4.6) using platinum sheets. All the measurements were corrected for the blank signal (alumina + platinum).
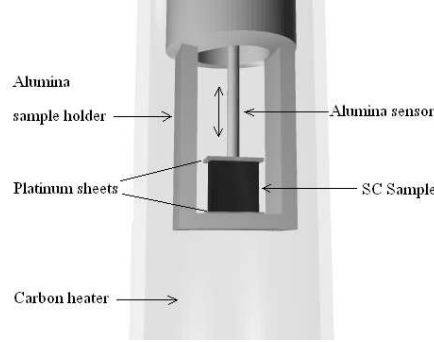
Figure 4.6: *Set-up used to measure the thermomechanical behavior of our YMnO$_3$ single crystal.*

4.5   Powder experiments

In order to obtain more insight into the nature of the IP, we have performed high temperature powder neutron diffraction. The main idea is to try to distinguish between the different proposed symmetries for the IP, namely P6$_3$/mcm and P6$_3$cm. Due to the small differences in the intensities of the reflections expected for the two models and the low neutron flux available at the JEEPII reactor, we focused on a limited range of reciprocal space to distinguish between P6$_3$/mmc and the two other possible symmetries P6$_3$/mcm and P6$_3$cm. The experiment has been performed at a single temperature between T$_{C1}$ and T$_{C2}$ (T$\sim$1223K) collecting data over 4 days. The recorded pattern is presented in figure 4.7.

From powder diffraction experiments, it is very difficult to distinguish between the P6$_3$cm and P6$_3$/mcm symmetries, since the reflection conditions are the same. Moreover, there is no enlargement of the unit cell, which would give rise to new reflections as in the case of P6$_3$/mmc symmetry. We have refined our data using both symmetries. Since we have limited range in d-spacing, we have done refinements with extreme care. We used in both cases the same profile function, where we refined only two Lorentzian components, one Gaussian component, one parameter for the shift and one parameter for asymmetry. We initially performed Lebail fitting in order to determine the optimum profile parameters [37]. In subsequent refinements, these parameters remained fixed. The results of these refinements are presented in figures 4.8 and 4.9. In these figures, we plot $\sqrt{I}$ in order to emphasize small differences in intensities. In the lower part of the figures 4.8 and 4.9, we emphasize the difference pattern.

As can be observed in figures 4.8 and 4.9, the quality of the fit is very similar between the two different models. Using the P6$_3$cm model gives rise to unrealistic bond lengths. Using the P6$_3$/mcm symmetry, we obtain negative values for the U$_{iso}$ indicating that something is incorrect with the
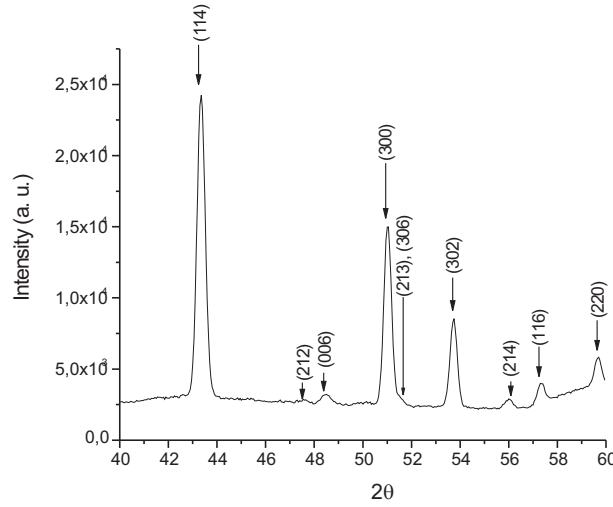
Figure 4.7: *High temperature powder neutron diffraction data of $YMnO_3$ recorded at $T \sim 1223K$ measured at the JEEPII reactor. This temperature is included in the range between T_{C1} and T_{C2}. The presence of the (214) reflection proves that we are not yet in the high temperature phase with the $P6_3/mmc$ symmetry.*
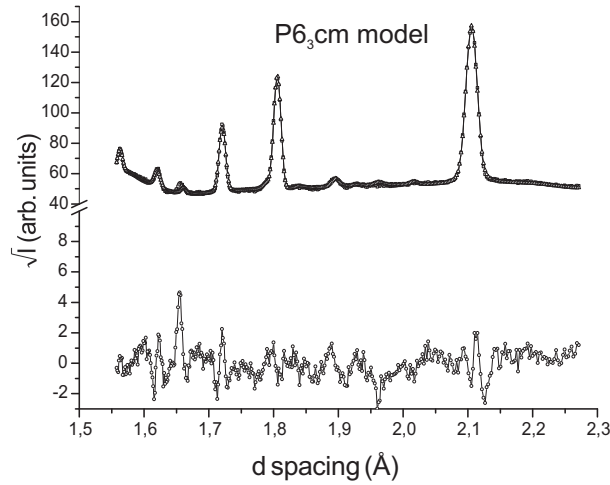

Figure 4.8: *Observed, calculated and difference patterns of $YMnO_3$ at 1223K for refinement done with the $P6_3cm$ symmetry.*

model. However one should notice that the numbers of free parameters (atomic coordinates not fixed by symmetry) in $P6_3cm$ symmetry is significantly larger than for $P6_3/mcm$ symmetry (10 versus 3). Therefore, we have a surprisingly good model for the $P6_3/mcm$ symmetry, considering the short d-spacing range of our data. However, we cannot conclusively differentiate the two models from this single experiment.

Due to the large number of parameters (especially for the $P6_3cm$ model)
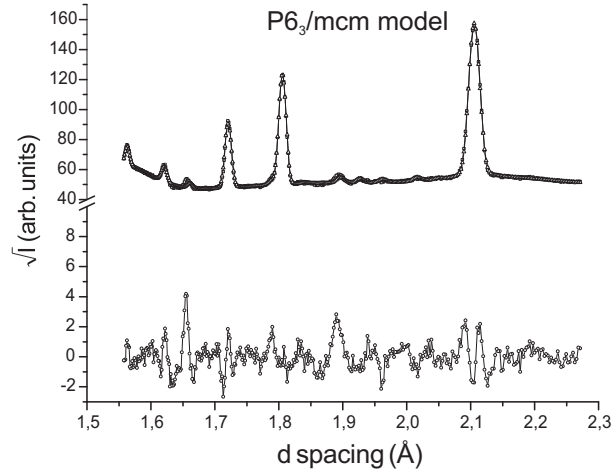
Figure 4.9: *Observed, calculated and difference patterns of YMnO$_3$ at 1223K for refinement done with the P6$_3$/mcm symmetry.*

and the very small number of reflections, it was impossible to distinguish between the two models. We decided to measure powder full datasets using a high resolution and high brilliance X-ray synchrotron. This experiment has been carried out with the set-up described previously at ESRF on the ID31 beamline (see figure 4.5). We measured at several temperatures, concentrating on the range 950K-1475K. This is below and above the expected T$_{C2}$ temperature (around 1300K). We present the measured cell parameters in figure 4.10.
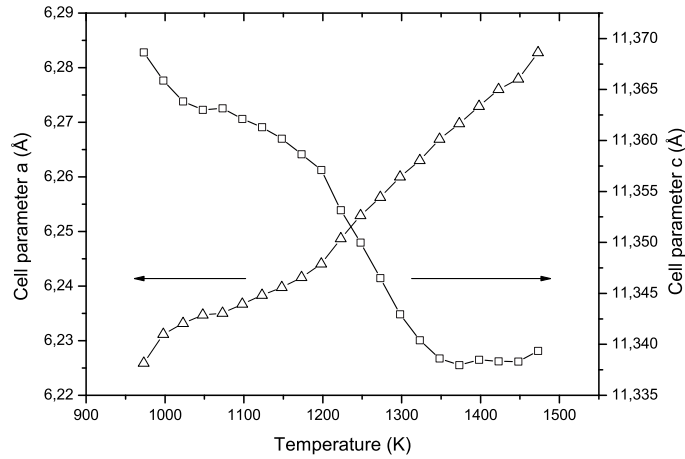

Figure 4.10: *Cell parameters obtained from a powder sample at the ID31 beamline at ESRF with P6$_3$cm symmetry.*

In figure 4.10, we can clearly see an anomaly around 1325K characteriz-

ing the transition towards the P6$_3$/mmc symmetry. This transition is also evidenced by the disappearance of the (214) reflection. We show in figure 4.11 evidence for the tripling of the unit-cell below T$_{c2}$ $\simeq$1325K.
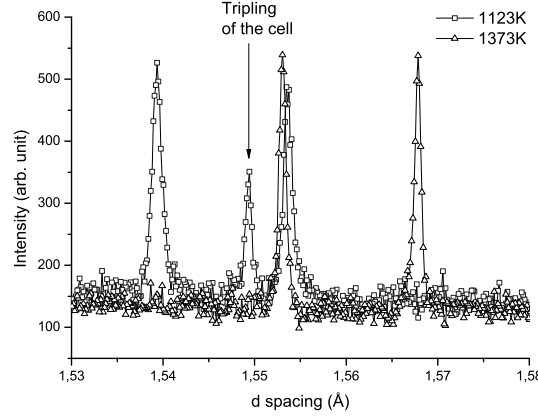

Figure 4.11: *Disappearance of the (214) reflection as function of temperature determined by X-ray synchrotron diffraction. This evidences the transition towards the P6$_3$/mmc symmetry.*

We refined the structure at high temperature including the Pt contribution of the sample holder. We give in table 4.8 the atomic coordinates in the high temperature centrosymmetric phase P6$_3$/mmc at 1373K. A physically meaningful model could be reached only by constraining all the U$_{iso}$ of the different atoms to be equal.

Atom	x	y	z	U$_{iso}$
Y	0	0	0	0.0270(7)
Mn	1/3	2/3	1/4	0.0270(7)
O$_1$	0	0	1/4	0.0270(7)
O$_2$	1/3	2/3	0.0821(8)	0.0270(7)

Table 4.8: *Atomic coordinates determined by X-ray synchrotron Rietveld refinement at 1373K in the P6$_3$/mmc symmetry. Cell parameters: a = 3.62178(2) Å and c = 11.3379(2) Å.*

Although, the cell parameters (see figure 4.10) do not present any anomaly below the change of symmetry, we had a look at the oxygens O$_{11}$ and O$_{12}$, more particularly at the evolution of their z coordinate. Indeed in the transition from the paraelectric to ferroelectric phase, the displacements along the *c* axis are expected to be significant (see table 4.7).

However, no anomalies could be clearly observed in the z coordinate of the oxygens O$_{11}$ and O$_{12}$ over the whole temperature range studied because
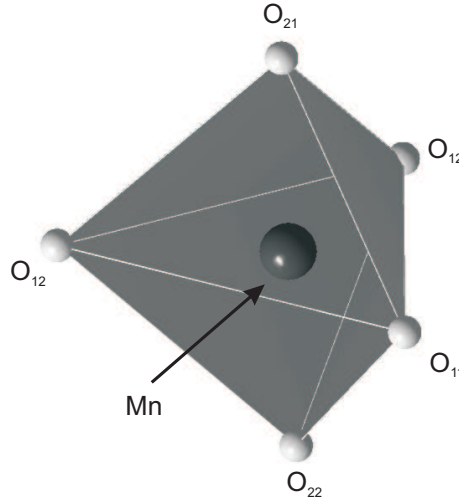
Figure 4.12: *Trigonal bipyramid of manganese represented by P6$_3$cm symmetry.*

the error bars are large, mainly due to two reasons. First of all, we use X-ray radiation which is less sensitive to oxygens than to heavy atoms. However it is mostly due to the Pt capillary which absorbs much of the X-ray flux giving a poor signal-background ratio.

We expect from the symmetry adapted mode analysis that the largest atomic displacements involve the oxygen atoms. Consequently, a neutron experiment is the natural next step in the search for an intermediate phase. We have carried out additional data collection on the high resolution powder diffractometer (HRPD) at ISIS. In order to minimize the eventual decomposition of our sample, we sealed about 10g of powder in a quartz ampoule. We wanted also to study the effect of the static atmosphere on our measurement. Thus, we used two quartz ampoules, one sealed under vacuum ($\approx 10^{-4}$ bar) and the other one at normal pressure (air). For the sample sealed under vacuum, we have made a series of short runs and a few long runs for better statistics. Thus, we will discuss below mostly the results of the evacuated quartz ampoule sample. We have used the P6$_3$cm symmetry to refine the data of the short runs. We present in figure 4.13 the cell parameters versus temperature extracted from the short run refinements.

We can see in figure 4.13 that the trend of the cell parameters versus temperature is quite similar to that determined by X-ray. We confirm the transition towards the high temperature centrosymmetric phase above T$\simeq$1300K. In contrast with the X-ray experiment, we could carry out good refinements with good statistics and even determine U$_{aniso}$ parameters (wR$_f$ = 3.80%; wR$_{exp}$ = 3.01% for a GoF = 1.27). We present the results in table 4.9 and table 4.10.

The signal/noise ratio is better in the neutron data due to the fact that bulky sample environment can be used with little absorption of the neutrons.
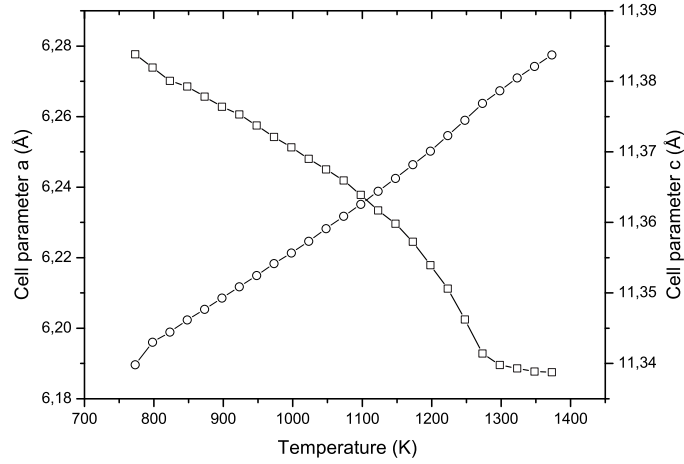
Figure 4.13: *Cell parameters (P6$_3$cm symmetry) obtained from a powder sample using the instrument HRPD (neutron).*

Atom	x	y	z
Y	0	0	0
Mn	1/3	2/3	1/4
O$_1$	0	0	1/4
O$_2$	1/3	2/3	0.08507(8)

Table 4.9: *Atomic coordinates determined by neutron Rietveld refinement for 1373K in the P6$_3$/mmc symmetry using HRPD at ISIS. Cell parameters: a = 3.62454(1) Å and c = 11.33843(5) Å.*

Neutron data allow us to have one order of accuracy better for most of the refined parameters including good and meaningful U$_{aniso}$ parameters. In the refinements that we have done using the P6$_3$cm symmetry, we have fixed the z coordinate of Y$_1$ to its RT value due to the lack of a center of symmetry. A splitting of the Y$_2$ position into two different positions (Y$_{2a}$ and Y$_{2b}$) was introduced between 1098K and 1273K because there were two refinement "minima" corresponding to two distinct z coordinates. Placement of Y$_2$ on the "average" position resulted in a thermal ellipsoid highly elongated along *c*. Additionally, the splitting of the Y$_2$ position led to an improvement in the fit (wR$_{exp}$=4.28% for Y$_{2a}$ and Y$_{2b}$ versus wR$_{exp}$=4.71% for one Y$_2$ position at T=1223K). We note that Y$_1$ remains off-center with respect to the oxygen polyhedra giving a net polarization. Refinements below 1098K using this Y$_2$-disorder model did not improve the quality of the fit. Thus, we have performed below this temperature refinements with only one Y$_2$ position. Between 1098K and 1273K, we have used 2 Y$_2$ positions. Above

Atom	Y	Mn	O$_1$	O$_2$
U$_{11}$	0.0193(4)	0.0375(7)	0.0338(5)	0.0352(4)
U$_{22}$	0.0193(4)	0.0375(7)	0.0338(5)	0.0352(4)
U$_{33}$	0.0759(9)	0.0220(9)	0.074(1)	0.0233(7)
U$_{12}$	0.0096(2)	0.0187(3)	0.0169(3)	0.0176(2)
U$_{13}$	0	0	0	0
U$_{23}$	0	0	0	0

Table 4.10: *Anisotropic atomic displacement components in angstroms squared determined by neutron Rietveld refinement for 1373K in the P6$_3$/mmc symmetry.*

T=1273K, we have a change in symmetry and thus no reason to introduce two Y$_2$ positions.
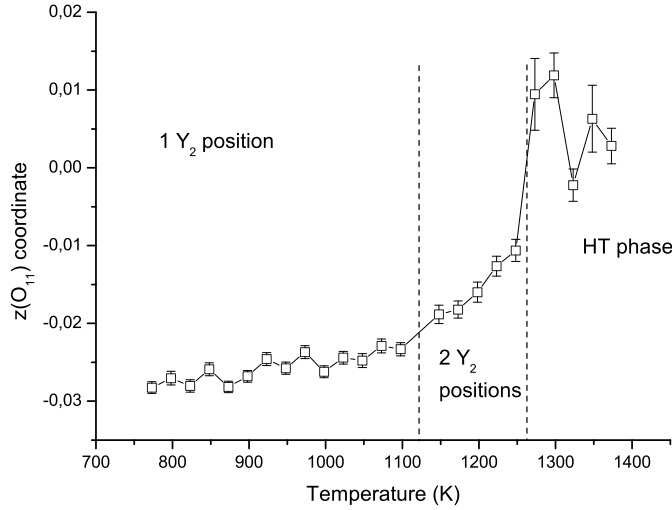

Figure 4.14: *z coordinate of oxygen O$_{11}$ extracted from the neutron refinements in the P6$_3$cm symmetry.*

We present in figure 4.14, the temperature dependence of the z coordinate of the oxygen O$_{11}$. Due to the better accuracy obtained from the neutron experiment, we can see that z(O$_{11}$) is increasing almost linearly over a range of about 250K followed by a change in slope around 1100K. Above this temperature, the temperature dependence is also linear until T≈1300K. Once, we reach the high temperature phase, z(O$_{11}$) is constant within the error bars. The large error-bars and scattered values at high temperature are caused by the use of the P6$_3$cm space group instead of P6$_3$/mmc, which introduces many correlations.

The room temperature crystal structure of YMnO$_3$ exhibits a ferrielec-

tric state with two unequal and opposite Y-dipoles. These two dipoles result from the off-centering of Y_1 and Y_2 ions. We neglect the small contribution of the off-centering of the Mn ions. The interpretation of the Y_2-disorder model is the following: while the off-centering of Y_{2b} gives rise to a parallel dipole to the one resulting from the off-centering of the Y_1 ion, the off-centering of Y_{2a} gives rise to an antiparallel dipole. Thus we interpret this model as the inability of the system to decide whether to display a ferroelectric or a ferrielectric state over the temperature range of the IP. On further cooling down below T_{C1}, the system adopts the ferrielectric state. This model supports the scenario proposed by Fennie *et al.* [12] where they proposed an IP with a non-zero polarization having the same symmetry as at RT.

In order to confirm the transition towards the high temperature centrosymmetric phase around 1300K, we compare the corrected z(Mn) and the *c* cell parameter. The corrected z(Mn) is based on putting Y_1 at the origin in order to compare with the setting of the high temperature phase ($P6_3/mmc$ symmetry). We present the comparison in figure 4.15.
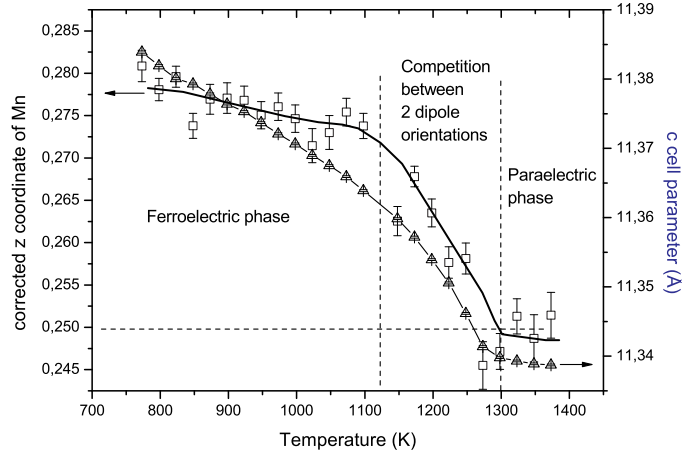

Figure 4.15: *Temperature dependence of corrected z(Mn) compared to that of the* c *cell parameter extracted from the neutron refinements using the P6₃cm symmetry. Squares represent the corrected z coordinate of Mn and triangles the* c *cell parameter.*

In figure 4.15, we observe that the z coordinate of Mn is continuously decreasing versus temperature. We notice a change of slope in lattice parameter *c* and in the fractional coordinate around 1100K corresponding to the transition between the Y_2-disorder model and the model without disorder. Around 1300K, the z coordinate is locked within the error bars to the value 1/4 corresponding to the z coordinate of Mn in the high tem-

perature P6$_3$/mmc phase. The appearance of the high temperature phase around 1300K is confirmed by an anomaly in the cell parameter c and the disappearance of the (214) reflection (not shown). Here again, the large error-bars and scattered values of the z coordinate of Mn above T$_{C2}$ are caused by the use of the P6$_3$cm space group instead of P6$_3$/mmc, which introduces many correlations.

Since from group theoretical arguments, it is possible that the intermediate phase has the P6$_3$/mcm symmetry, we have also carried out refinements using this symmetry within the intermediate phase at 1223K. We present in table 4.11 the results of the refinement done in P6$_3$/mcm and in table 4.12 the refinement done in P6$_3$cm using the Y$_2$-disorder model.

Atom	x	y	z	U$_{iso}$
Y$_1$	0	0	0	0.017(1)
Y$_2$	1/3	2/3	0	0.0303(6)
Mn	0.331(1)	0	1/4	0.0185(5)
O$_{11}$	0	0	1/4	0.091(3)
O$_{12}$	1/3	2/3	1/4	0.0133(6)
O$_2$	0.6608(5)	0	0.9126(1)	0.0196(3)

Table 4.11: *Atomic coordinates determined by neutron Rietveld refinement at 1223K in the P6$_3$/mcm symmetry using HRPD at ISIS. Cell parameters: a = 6.25676(4)Å and c = 11.34598(7) Å. wR$_f$ = 4.43% and wR$_{exp}$ = 5.55% for a GoF = 1.83*

Atom	x	y	z	Occ.	U$_{iso}$
Y$_1$	0	0	0.2712(-)	1	0.025(1)
Y$_{2a}$	1/3	2/3	0.2389(6)	0.5	0.0077(5)
Y$_{2b}$	1/3	2/3	0.2759(7)	0.5	0.0077(5)
Mn	0	0.3521(8)	0.0087(8)	1	0.0188(6)
O$_{11}$	0	0	-0.0148(4)	1	0.020(1)
O$_{12}$	1/3	2/3	0.0049(6)	1	0.0222(7)
O$_{21}$	0	0.3394(7)	-0.1554(4)	1	0.026(1)
O$_{22}$	0	0.3230(5)	0.1739(4)	1	0.0141(8)

Table 4.12: *Atomic coordinates determined by neutron Rietveld refinement at 1223K in the P6$_3$cm symmetry using HRPD at ISIS. Cell parameters: a = 6.25678(3)Å and c = 11.34599(5) Å. wR$_f$ = 3.71% and wR$_{exp}$ = 4.28% for a GoF = 1.41*

We clearly see that the Y$_2$-disorder model gives a better fit wR$_{exp}$ = 4.28% versus 5.55% for P6$_3$/mcm model. Moreover in the refinement using the P6$_3$/mcm symmetry, the U$_{iso}$ of O$_{11}$ is very high, suggesting that the model is wrong. The powder data show evidence for the existence of an IP

in which there is competition between parallel and antiparallel Y_2 dipoles. This IP would exist between a $T_{C1} \simeq 1100K$ and the high temperature paraelectric phase around 1300K.

In addition to the investigation of the IP, we have also investigated the effect of the static atmosphere on the structure of our compound. Indeed, it has been reported that a sample contained in a dynamic vacuum (continuous pumping) eventually gives rise to a partial decomposition of the sample while heating [11, 32]. Consequently, as stated previously, we have prepared two samples: both were sealed in a quartz ampoule but one in air, the other one in vacuum ($\approx 10^{-4}$ bar). The two samples originate from the same synthesis. A sample from the same batch was also used for the X-ray synchrotron experiment. The results presented above were for the sample contained in an evacuated ampoule. For the other sample, we have carried out only short runs in order to determine the cell parameters, shown in figure 4.16.
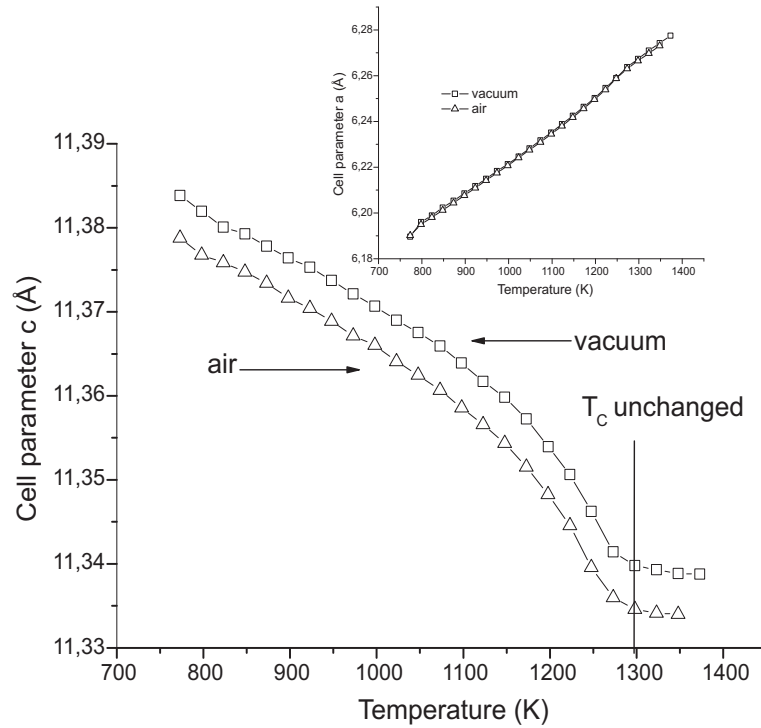

Figure 4.16: *Differences in the cell parameter* a *and* c *between the samples held in vacuum and in air determined by neutron diffraction using HRPD at ISIS.*

While the *a* cell parameter is unchanged over the whole temperature range investigated, there are significant differences in the *c* cell parameter between the sample measured in air and the one measured in vacuum. Indeed, one can see that the *c* cell parameter for the sample measured in vacuum is higher by a constant amount of about 0.005 Å, which is above

the resolution of the determination of the cell parameter (error on $c \simeq 10^{-5}$). Due to the difference in atmosphere, one may argue that the difference between the samples is the presence of vacancies in the sample measured in static vacuum. The number of vacancies once formed seems to be constant since we have a constant difference in the c cell parameter as function of temperature. This is confirmed by the absence of any difference in the cell parameter a. Thus, this excludes a possible off-set due to misalignment between the two experiments. If there are vacancies, we would expect a reduction of the volume. In contrast, if there are oxygen vacancies, the cations become closer to each other and the coulomb repulsion may give rise to an enhancement of the unit-cell along the c axis as observed. Consequently, the vacancies seem to be found on preferential sites between the different layers of MnO$_5$ and Y stacked along the c axis. Surprisingly, the presence of these vacancies does not alter the transition temperature towards the high temperature phase P6$_3$/mmc, as evidenced in figure 4.16. More experiments are required to clarify the effect of vacancies on the structural properties.

Combining high temperature and high resolution neutron and synchrotron diffraction on powder samples, we are able to give evidence for the existence of an IP and to determine the transition to the HT phase using high quality data. The IP can be modelled by a Y$_2$-disorder model: 1) Y$_1$ is off centered with respect to its coordinating oxygens; 2) Y$_2$ is off-centered with respect to its coordinating oxygens with dipoles that are 50% parallel and 50% antiparallel to the Y$_1$ dipole. We decided to further investigate the high temperature behavior of YMnO$_3$ using single-crystal experiments.

4.6   Single-crystal experiments

Prior to the temperature dependent experiments that we wanted to carry out, we have checked the quality of our single crystal of YMnO$_3$. A fragment extracted from the as-grown boule (see figure 4.4) of approximatively 0.14×0.12×0.04 mm was selected under a microscope. Using a Bruker SMART Apex CCD diffractometer, we carried out data collection at room temperature. The atomic coordinates and the isotropic displacement parameters determined by the refinement are presented in table 4.13. This structure is very similar to the previously reported single-crystal structures of YMnO$_3$ [9]. The results and statistics presented in table 4.13 prove that our single crystal is of good quality.

We have carried out high temperature X-ray synchrotron measurements on beamline BESSRC-11-ID-C at the Advanced Photon Source using a wavelength of 0.10772 Å. Due to the experimental set-up, we needed to use an oriented single crystal (small angular range available). In figure 4.17, we show six representative diffraction patterns from RT up to 1353

Atoms	x	y	z	U_{eq} (Å^2)
Y_1	0.00000	0.00000	0.7711(2)	0.0056(5)
Y_2	1/3	2/3	0.73038(-)	0.0060(3)
Mn	0.6672(5)	0	0.4976(2)	0.0059(5)
O_1	0.697(1)	0	0.661(1)	0.010(2)
O_2	0.353(1)	0	8352(9)	0.005(2)
O_3	0.00000	0.00000	0.973(2)	0.008(3)
O_4	1/3	2/3	0.515(1)	0.010(3)

Table 4.13: *Atomic coordinates of a single crystal $YMnO_3$ grown by the Floating Zone Technique from data collected at room temperature. The cell parameters are a = 6.1469(6)Å and c = 11.437(1)Å (space group $P6_3cm$, $wR(F^2)$ = 8.45% and R(F) = 3.43%). In brackets, we indicate the relative error. The z coordinate of Y_2 was fixed due to the lack of a center of symmetry.*

K. Between 1283K and 1383K, we can clearly see the disappearance of the reflections (124), (204), (102) and (022). At 1283K, we only observe weak diffuse scattering and at 1353K the vanishing of the reflections. The disappearance of these reflections, while the reflections (113) and ($2\bar{1}3$) remain above T_{C2} signals a phase transition. According to group theory (section 4.3), the possible high temperature symmetry is $P6_3/mcm$ (without volume change) or $P6_3/mmc$ (with volume divided by a factor of 3). From the few reflections that we have studied, we cannot assign the space group. The reflection conditions for space groups $P6_3cm$ and $P6_3/mcm$ are identical ($h\bar{h}0l$: l=2n and 000l: l=2n) while the reflection conditions for $P6_3/mmc$ are hkil: l=2n. Thus the disappearance of the reflections between 1283K and 1383K clearly demonstrates that the symmetry above T_{C2} is $P6_3/mmc$. These observations are confirmed by the results of the powder experiments in section 4.5 at similar temperature.

From the few reflections that we could follow versus temperature, we derive the cell parameters, shown in figure 4.18. The lattice parameter c clearly shows two transitions, one near 1050 K and the other near 1300 K. We associate these transitions with the two temperatures T_{C1} and T_{C2}, respectively. The two phase transitions are more obvious than in the cell parameters obtained from the powder experiments, where we could observe only one anomaly at the tripling of the unit-cell. We notice that the cell parameters of figure 4.18 are slightly different to the values reported in the literature. This is due to the large systematic error resulting from the few reflections from which these cell parameters are derived. However it does not affect the trend of the cell parameters. A full refinement at RT on single crystal provides $a = 6.1469(6)$Å and $c = 11.437(1)$Å in good agreement with the values of ref. [9] (see table 4.13).

We now look in more detail at the temperature dependence of the square
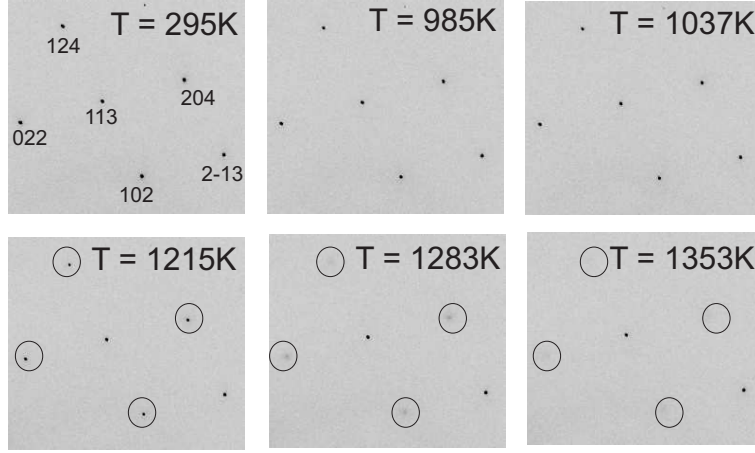
Figure 4.17: *Image plate data showing the evolution of the peak intensities versus temperature from RT to 1353K using single-crystal X-ray synchrotron radiation.*

root of the integrated intensity ($\sqrt{I_{102}}$) of the reflection (102). In figure 4.19, we plot $\sqrt{I_{102}}$ as a function of temperature. The $\sqrt{I_{102}}$ describes the atomic displacements which are responsible for the change of symmetry from the IP towards the HT P6$_3$/mmc phase. Consequently, we can consider that $\sqrt{I_{102}}$ is equivalent to the primary order parameter in the phase transition at T$_{C2}$. The transition at T$_{C2}$ can be interpreted either as a 1st order transition (rapid decrease of $\sqrt{I_{102}}$ as a function of temperature) or as a 2nd order phase transition. The rather poor control of the temperature and the size of the temperature step used do not allow us to determine clearly the nature of the phase transition at T$_{C2}$. The temperature dependence of the cell parameters is consistent with a second order transition.

In order to further investigate the transitions, we have carried out TMA on a single crystal. In figure 4.20, we show the temperature dependence of the dilatometric response of an unoriented single crystal of YMnO$_3$. This crystal is from the same growth as the one used for the synchrotron experiment. We observe clearly two anomalies while heating. The first anomaly appears at about 1100K (corresponding to T$_{C1}$) and the second anomaly appears at T$_{C2}$~1350K. These results confirm the existence of an IP in YMnO$_3$. The set-up used at the Advanced Photon Source did not allow an accurate control of the temperature. Therefore, TMA (and DTA below) allow more accurate transition temperatures to be determined. Moreover, we notice that the value found here for T$_{C2}$ is in good agreement with that determined from the powder neutron and synchrotron data (see figures 4.16 and 4.10). Nevertheless, there are quantitative and differences between the TMA data and the lattice parameters, which remain to be resolved.

We had a closer look at the temperature dependence of the TMA response close to T$_{C2}$. In figure 4.21, we show a zoom of the TMA response
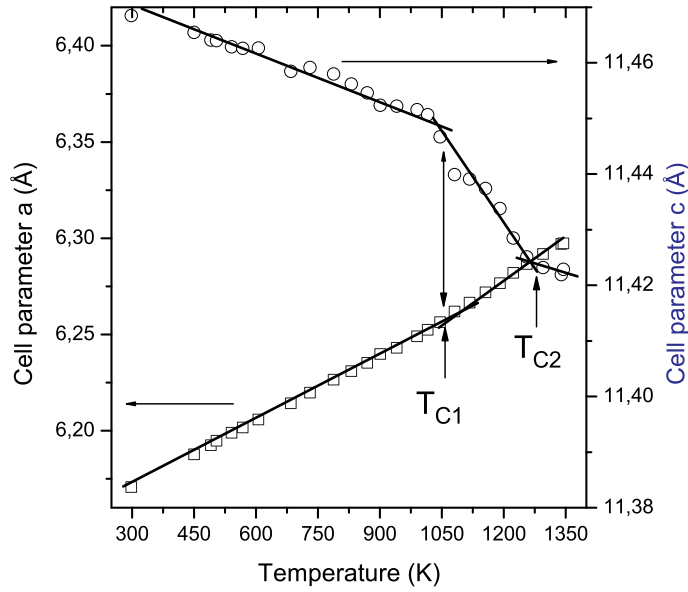
Figure 4.18: *Temperature dependence of the cell parameters* a *(left) and* c *(right) determined by single-crystal X-ray synchrotron diffraction. The arrows indicate the two transition temperatures at* T_{C1} *and* T_{C2}. *The tripling of the unit cell occurs at* T_{C2}.

close to T_{C2}, which is linear below about 1340K. While measuring the TMA response, one measures the strain which usually plays the role of a secondary order parameter during a phase transition. Indeed, we know that the transition from the HT phase to the IP could involve some strain as a secondary order parameter. The linear dependence on temperature of the TMA response suggests that the transition at T_{C2} is of 2nd order.

The area of a peak in a DTA scan (whether endothermic or exothermic) is related to the enthalpy change (ΔH) [38]. Consequently, in order to clarify the nature of the two phase transitions, we carried out a DTA experiment on a crushed single crystal under N_2 atmosphere. The results are presented in figure 4.22. We notice a small anomaly at T_{C1} and a larger one at T_{C2}. The main characteristic of a first order transition is the presence of latent heat. Thus the large peak at about 1350K suggests that the transition could be first order. The DTA anomaly at about 1100K is small compared to the peak near 1350K. We interpret the nature of this transition (from IP towards the RT phase) as second order or weakly first order. However, the differentiation between 2nd order and 1st order phase transitions using DTA remains a non-straightforward task [39]. Thus, we have no firm evidence for a first order transition and from the diffraction data, we are inclined to conclude that it is second order.
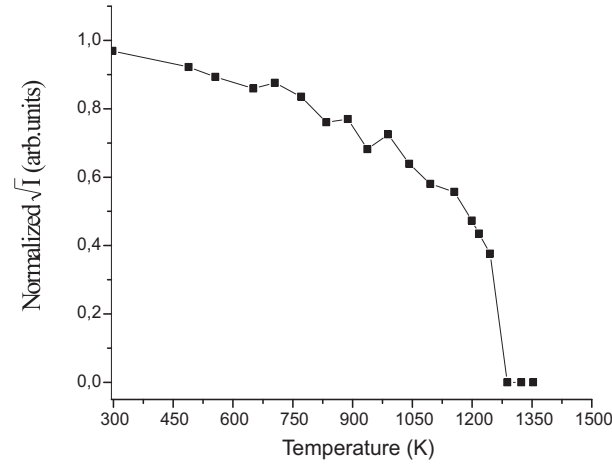
Figure 4.19: *Square root of the integrated intensity of the reflection (102) versus temperature.*
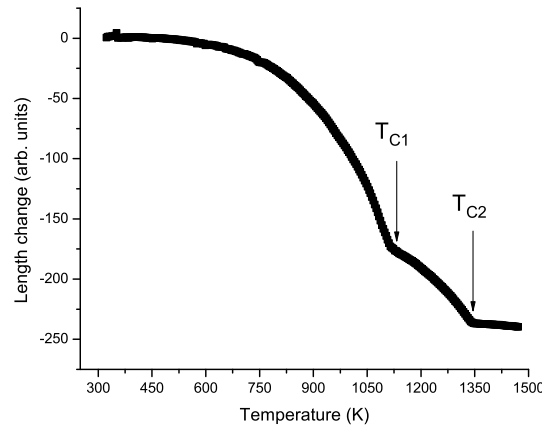

Figure 4.20: *Dilatometry measurement of an unoriented single crystal of YMnO$_3$. The arrows indicate the transition temperature T_{C1} and the tripling of the unit cell T_{C2}.*

Based on the different experiments that we have carried out, we know now several features of the transition involving the tripling of the unit cell. In order to explore the mechanism of the phase transition in more detail, we have analyzed the relative stability of the different structures by means of electronic structure calculations on the relevant phases.
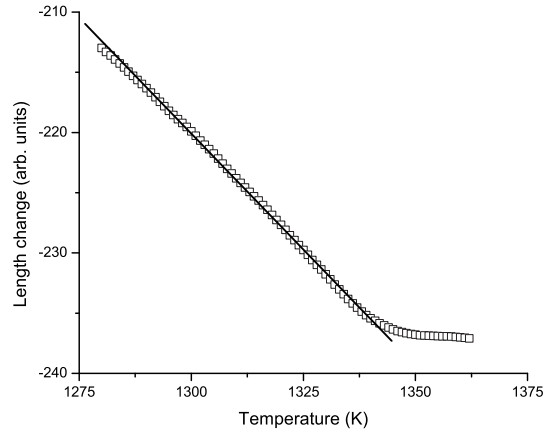
Figure 4.21: *Linear temperature dependence below T_{C2} of the thermomechanical analysis.*
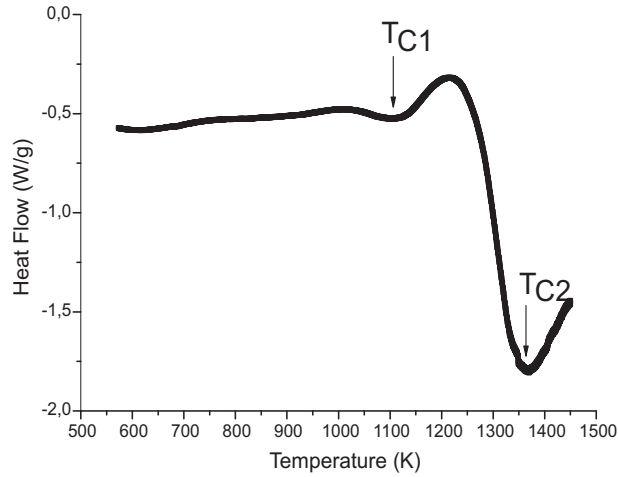

Figure 4.22: *Differential Thermal Analysis of a crushed single crystal of YMnO$_3$. The measurement was carried out in a N$_2$ atmosphere with a rate of 5K/min. The arrows indicate the transition temperature T_{C1} and the tripling of the unit cell at T_{C2}.*

4.7 Contribution of Band structure calculations

4.7.1 Introduction

In order to investigate the origin of the phase transition, the electronic structure of YMnO$_3$ has been described using different methods of solid state physics. In particular, we mention the LDA and LDA+U calculations on the low and high temperature hexagonal phases of YMnO$_3$ by Medvedeva *et al.* [40] and the recent work of Fennie and Rabe [12] using the same LDA+U

approach to describe the phase transition. In the work of Medvedeva *et al.* [40] it is shown that LDA fails to properly describe the insulating magnetic character of this compound as found in many other magnetic materials [41]. The same authors also explore the LDA+U approach which supplements the LDA with an effective on-site repulsion for the Mn^{3+} ions. This approach improves the band gap and the spin localization on Mn ions in YMnO$_3$, but its usual implementation [42] involves the introduction of two semiempirical parameters. The values given to these parameters are critical and usually are chosen by fitting the calculated properties to some experimental data for the same or analogous materials. The same LDA+U approach of Medvedeva *et al.* [40] has also been used by Fennie and Rabe [12] to explore the structural phase transition. In this work, group theoretical analysis and electronic structure calculations are used to connect the high and low temperature phases. These authors propose a possible mechanism to describe the phase transition involving an isotructural phase transition between the IP and the room temperature one. However, they do not explore the full energy landscape of the system (including the room temperature phase).

A different procedure, considered in the present work, consists in choosing an alternative DFT based approach to describe the electronic structure of YMnO$_3$. The introduction of hybrid exchange density functionals in which the exact Fock exchange is mixed with a given exchange functional and the correlation is also treated within the density functional framework made very significant progress in the description of molecular and solid state systems. In particular, we used the spin polarized formulation of hybrid DFT based on the so-called B3LYP exchange-correlation functional [43, 44] as implemented in the CRYSTAL03 code [45]. This hybrid DFT approach performs excellently in describing many different types of molecules and solids. This functional appears to be very well suited to describe not only the band gap [46] but also the structural parameters [47, 48] and the magnetic coupling constants [48, 49] of this kind of transition metal compounds. See, for instance, the recent investigation of the closely related ScMnO$_3$ by Bredow, Jug and Evarestov and references therein [48].

In the present approach the crystalline orbitals are constructed as linear combinations of Bloch functions built from atomic orbitals (AOs) optimized for the crystal environment. The AOs are contracted real solid spherical harmonic Gaussian-type functions (GTFs). Extended all-electron basis sets have been used to describe Mn^{3+} and O^{2-} in an ionic environment whereas a Hay and Wadt small-core pseudopotential [50] has been used to represent inner electrons of Y. The reciprocal space was sampled according to a regular sublattice defined by six points in the irreducible Brillouin zone generated via the Monkhorst-Pack scheme [51]. The values adopted for the computational parameters (Coulomb and exchange integral evaluations and convergence of the self-consistent-field procedure) ensure the numerical ac-

curacy required for the evaluation of energy differences of 10^{-6} a.u. (see refs. 44 and 45 for detail). For YMnO$_3$, we have analyzed in detail the electronic structure and magnetic coupling of the material at room temperature using the experimental structure given in ref. [15]. [3]

4.7.2 Results and Discussion

The calculations show that the system is an insulator with a gap of 1.8 eV. For the ferromagnetic state, the Mulliken analysis of the charge distribution provides a net charge of Mn$^{+1.90}$, O$^{-1.40}$ and Y$^{+2.60}$. These charges deviate from the formal +3, -2 and +3 charges and this is an indication of a significant degree of covalency in the interactions between the constituent ions. The spin population analysis shows that the d$_{z^2}$ orbital is unoccupied and the spin density on the Mn ions is 3.88 electrons, corresponding to an effective particle with S = 2. This result is consistent with the experimentally observed moment of 3.30 μ_B from neutron diffraction at 10K [52].

The antiferromagnetic ground state shows spin frustration, as expected for the triangular net of spins. For the evaluation of the magnetic coupling constant between nearest neighbor Mn ions, two different magnetic phases have been considered (see ref. 49 for details); a ferromagnetic phase and a frustrated AF ground state. The magnetic coupling constant J can be related to the energy difference between these two magnetic phases through the Ising Hamiltonian:

$$H^{Ising} = - \sum_{<i,j>} J_{ij} S_{z,i} S_{z,j} \qquad (4.13)$$

where only the $S_{z,i}$ components of the $\mathbf{S}_i$ magnetic moment vectors are considered and $< i, j >$ indicates that only the interaction between nearest neighbor magnetic moments is taken into account. In this case, the energy per formula unit corresponds to

$$E(AF) - E(F) = 18J = -102.2 meV \qquad (4.14)$$

and hence J = -5.7meV, in good agreement with the experimental estimation of -3.8 meV by Park *et al.* [52].

The relative stabilities of the different structural phases have been analyzed by a restricted energy minimization of the internal coordinates of the atoms in each cell using a common set of cell parameters for the room temperature structure and intermediate phases ($a = 6.1469$ Å and $c = 11.437$ Å) as a starting point. Under these conditions, it has been observed that

---

[3] These calculations have been carried out by Ibério de P. R. Moreira at the Departament de Química Física and CeRQT, Universitat de Barcelona, Barcelona, Spain.
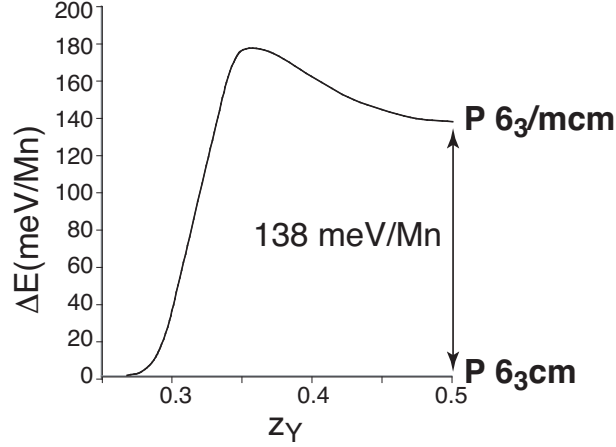
Figure 4.23: *Energy landscape between the RT (P6$_3$cm) and IP (P6$_3$/mcm) symmetries by means of a continuous Y atom displacement along the polar axis. Z_Y is the coordinate of the Y atom under consideration (Y$_1$ in table 4.1).*

the low symmetry intermediate phase is unstable and the optimization of the structure parameters leads to the room temperature structure.

The high symmetry intermediate phase (P6$_3$/mcm symmetry) remains stable under small displacements of the atoms when optimized without internal constraints imposed by symmetry. This stability suggests that this phase is a local minimum for the system under these conditions. This local minimum is 138 meV/Mn atom (or 13kJ/mol) less stable than the room temperature optimized structure and only 49 meV/Mn atom ($\sim$5 kJ/mol) more stable than the optimized HT structure. In figure 4.23 we show the relative stability of the HT, IT and RT phases as well as an approximate energy profile connecting the intermediate and the low temperature structures by means of a continuous Y atom displacement. We note that the intermediate phase is a local minimum and a barrier of 38 meV/Mn atom is found in the approximate path connecting this and the RT structure.

4.8   Discussion

4.8.1   Powder results

We have carried out powder X-ray synchrotron and neutron diffraction at high temperature. We showed that a HT phase with P6$_3$/mmc symmetry is present above T$_{C2} \simeq$ 1300K. We presented in tables 4.9 and 4.10 the results of the refinement carried out for T = 1373K. Evidence for the existence of an IP was found from the refined atomic coordinates between 1100K and 1300K. This IP could be best characterized using a Y$_2$ disorder model with P6$_3$cm symmetry rather than a model with paraelectric P6$_3$/mcm symme-

try. We interpret this model as being the expression of the inability of the system to choose between a parallel and antiparallel Y_2 dipoles.

The transition at T_{C1} was more obvious in the cell parameters determined from the single-crystal sample. There are several reasons which may contribute to this observation. A possibility is the differences in term of vacancies between the samples. The possible presence of these vacancies has not been investigated. However, from the neutron powder measurement carried out at ISIS, the value of the transition temperature T_{C2} is unchanged. We are unable to speculate on the eventual influence of vacancies on T_{C1} which is expected to be the ferrielectric transition temperature. Another difference could be the quality of the sample. In single crystal, the quality (crystallinity, order) is always better than in powder. It is possible that the transition at T_{C1} is simply broadened in the powder sample due to the different grain sizes, boundary effects, etc. Indeed a change in slope of the c cell parameter is seen in the vicinity of T_{C1} (see figures 4.10 and 4.13).

Our value of T_{C2} can explain the main features of the recent experiments by Lonkai and Katsufuji. Both groups used powders and failed to observe a phase transition. This holds with the exception of R=Tm where Lonkai *et al.* [11] observed the start of a transition, however without reaching the HT phase. Katsufuji *et al.* measured until 1000K for $YMnO_3$, synthesized in air, while our experiments show a transition at 1300K. For R=Lu and R=Yb, Lonkai *et al.* [11] and Katsufuji *et al.* [9] did not measure at sufficiently high temperatures in order to observe a phase transition. For the smaller rare-earths the ferroelectric transition is expected to be higher than for R=Y [19]. Therefore, our work seems in agreement with previous literature. Moreover, our work illustrates the complementarity of single-crystal X-ray and powder neutron diffraction in order to accurately pin-point the successive phase transitions in $YMnO_3$.

4.8.2 Single crystal results

Nature of the intermediate phase

The tripling of the unit cell below T_{C2} is characterized by likely second order character. This is evidenced by the absence of discontinuities in the cell parameters and the linear dependence of the TMA response close to T_{C2} (see figures 4.13 and 4.21). The disappearance of the (102) reflection (see figure 4.19) and the peak in the DTA experiment (see figure 4.22) are consistent with a second order transition although a weak first order transition cannot be excluded. Using group theory and Landau theory, we have shown in section 4.3.3 that in the case of a paraelectric IP with the $P6_3/mcm$ symmetry, the transition could be either a 1st order or 2nd order function of

the parameters α_1 and β_1. Band structure calculations show that the most stable phase is a paraelectric one with the symmetry P6$_3$/mcm. However, our powder diffraction results indicate that the IP should be described as a polar phase. Further work is required to characterize more thoroughly the nature of the IP.

Differences in critical temperatures

We have carried out X-ray synchrotron diffraction, DTA and thermomechanical analysis using a single crystal grown by the Floating Zone Technique. All these experiments evidence the existence of an intermediate phase between T$_{C1}$ and T$_{C2}$. We found that T$_{C1}$ $\simeq$1100K and T$_{C2}$ $\simeq$1300K. The phase transition at T$_{C2}$ is characterized by a change of symmetry to space group P6$_3$/mmc above T$_{C2}$. The value of T$_{C2}$ is in agreement with that reported in the literature (see section 4.2). However T$_{C1}$ is different to the previously reported value estimated to be around 950K which is about 150K below the transition temperature that we observed.

One possible explanation for the difference between our value of T$_{C1}$ and the 950K in older reports is the difference in the sample synthesis. Most previous work on YMnO$_3$ [19] was performed on crystals grown from a Bi$_2$O$_3$ flux. These samples probably contain some Bi and/or vacancies which could explain the difference in the critical temperatures. This is supported by the consistently lower c-axis lattice parameter for crystals grown from Bi$_2$O$_3$ flux compared to floating zone grown crystals.

Reference	a (Å)	c (Å)
Ref. 7	6.145	11.42
Ref. 15	6.1387	11.4071
Ref. 53	6.125	11.41
This work	6.1469(6)	11.437(1)

Table 4.14: *Comparison of the lattice parameters between single crystals grown from a Bi$_2$O$_3$ flux and this work (Floating Zone Technique).*

We expect that if Bi is incorporated into the structure, it will preferentially occupy the yttrium site. Bi^{3+} has a larger Shannon radius than Y^{3+}: r(Bi^{3+}) = 1.24Å (derived from the average between 6-fold coordination and 8-fold coordination) and r(Y^{3+})=1.1Å. Therefore, we expect an increase of the cell parameters. We have carried out refinements of the occupation on both Y-sites using the dataset of van Aken *et al.* [15] and our data. We did not find any evidence for substitution of Y by Bi. Thus, we have no experimental evidence for the incorporation of Bi into the lattice. The second possibility is the creation of vacancies. According to Abrahams [54], the ferroelectric transition temperature (in Kelvin) can be expressed as:

$$T_{FE} = (\kappa/2k)(\Delta z)^2 \tag{4.15}$$

where κ is a force constant, k is Boltzmann's constant and Δz is the largest displacement along the polar c axis between the ferroelectric phase and the paraelectric phase. This value is expressed in Å as $\Delta z = (z_{para} - z_{ferro}) \times c$. The ratio $\kappa/2k$ has been estimated as $2.00(9) \times 10^4$ KÅ^{-2}. According to equation 4.15, a decrease of T_{FE} implies a decrease of the force constant, the displacement of the rare earth z_{para}-z_{ferro} and/or a change in the c lattice parameter. It is obvious that defects can be responsible for such changes. For instance, an excess of yttrium ($YMn_{1-x}O_{3-3/2x}$) would certainly both decrease the c parameter (consistent with the observations) and lower κ. In the same way, impurities can lower T_{FE}. Even experiments using alumina crucibles instead of platinum can easily result in $YMn_{1-x}Al_xO_3$. Such a substitution would again account for a small decrease in the c parameter. All of these suggestions need to be checked experimentally. Concerning the possibility of oxygen vacancies within the structure: these are unlikely because electrostatic repulsions give rise to an enhancement in the c cell parameter (see figure 4.16). A difference in the concentration of vacancies could also explain the difference in the ferrielectric transition (T_{C1}) observed in the powder and single-crystal experiments. However, according to the powder data, the phase below T_{C2} also appears to be polar. Thus one may wonder why T_{C1} would be affected by vacancies while T_{C2} is not or at least to a lesser extent.

The ferroelectric mechanism

Band structure calculations by Fennie *et al.* [12] have suggested that the ferroelectric state originates at T_{C2} from the K_3 mode. The transition at T_{C1} is then an isostructural transition with P6$_3$cm symmetry. This model is supported by the fact that they found that K_3 is the only unstable mode. In addition, the K_3 mode was giving rise to the biggest atomic displacements.

Our structural data indicate a modification of this model. While the Y_1 ion is clearly off-center below T_{C2}, the Y_2 ion is best modelled using two different sites. The Y_2 dipoles are oriented 50% parallel and 50% antiparallel with respect to the Y_1 dipole. Our structural data are consistent with second order transitions both at T_{C1} and at T_{C2}.

Our band structure calculations suggest that the intermediate phase is paraelectric. In this case, the distortion is largely induced by a K_1 mode at T_{C2} followed at low temperature by a proper ferroelectric mode Γ_2^- at T_{C1}. Landau theory indicates that in this case the transition at T_{C2} is likely first order except at the Landau critical point. The transition at T_{C1} is likely to be second order.

The displacement pattern of the K$_3$ mode has been discussed in the literature [15]. In the following, we discuss the K$_1$ mode. We restrict our discussion to the displacement patterns associated with the primary order parameter only. The local symmetry for Y and Mn is given for the three phases in table 4.4. The displacements due to the K$_1$ mode from the HT phase to the IP are described in figure 4.24. We note that for this transition, mostly the apical oxygens O$_{2j}$ and the Mn are involved. The other oxygen atoms O$_{1j}$ are constrained by symmetry. In a trigonal pyramid, the O$_{2j}$ and Mn atoms are displaced in the same direction. This displacement gives rise to an enhancement $\sqrt{3}a \times \sqrt{3}b$ of the unit cell. These distortions give rise to: 1) two inequivalent Mn - O distances, 2) remove the C$_3$ axis and the mirror plane containing the basal oxygen atoms, 3) lower the local environment of Mn from D$_{3h}$ to C$_{2v}$. These displacements also create two inequivalent Y - O distances and thus two inequivalent Y-sites.
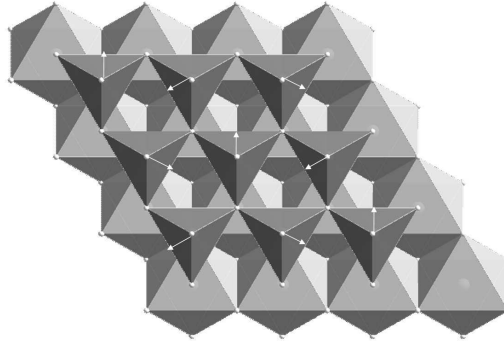

Figure 4.24: *Description of the atomic displacements taking place on the unit cell of YMnO$_3$ going from P6$_3$/mmc to P6$_3$/mcm at T$_{C2}$. The white arrows represent the displacement vectors of the oxygen O$_2$ (apical oxygens) and of the Mn atoms (not the same magnitude and not to scale).*

The displacements resulting from the ferroelectric mode $\Gamma_2{}^-$ below T$_{C1}$ are described in figure 4.25. The main feature of this transition is the creation of polarization along the c axis. This polarization results from the tilting of the MnO$_5$ polyhedra. This tilting is accompanied by a z displacement of the apical oxygens. This scenario is qualitatively in agreement with the displacement pattern of van Aken *et al.* since the displacements involved in the transition from P6$_3$/mmc to P6$_3$/mcm are small. The main contribution to the polarization is from the displacement of one of the oxygen atoms of the basal plane of MnO$_5$ towards the coordination sphere of the yttrium atoms resulting in a significant differentiation in the Y - O(apical) distances. Thus, the coordination of the Y atoms changes from 6 to 6+1 . Also, the Y atoms within the YO$_6$ octahedra will come closer to one triangle of the oxygen octahedron and thus further away from the other triangle, resulting

in a contribution to the polarization along the c axis. Finally, the C_2 axis of the MnO_5 polyhedra is removed by the displacement of the Mn and the basal plane oxygens.
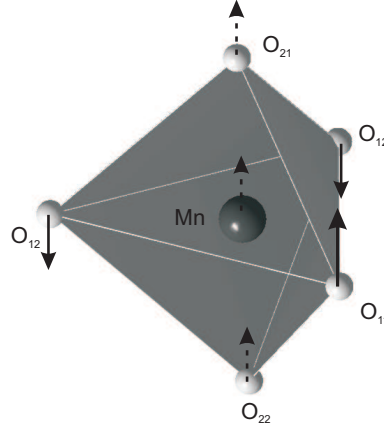

Figure 4.25: *Description of the atomic displacement pattern at the ferroelectric transition T_{C1} of $YMnO_3$ going from $P6_3/mcm$ to $P6_3cm$. We show here only the displacements associated with the trigonal bipyramid MnO_5.*

4.9   Conclusion

We have investigated the high temperature onset of ferroelectricity in hexagonal $RMnO_3$. For this purpose, we have considered the parent compound $YMnO_3$. Using group theory, we have demonstrated that the possible symmetries of the intermediate phase are $P6_3cm$ (identical symmetry to the room temperature structure) or $P6_3/mcm$. In addition, we have shown that the intermediate phase cannot be antiferroelectric as stated previously. Moreover, in the hypothesis of a paraelectric IP ($P6_3/mcm$), we have shown that the transition HT $\rightarrow$ IP could be either a second order or first order phase transition.

Using powder neutron and synchrotron diffraction, we could probe the reduction of the cell volume by a factor of 3 at $T_{C2} \simeq 1300K$ towards the $P6_3/mmc$ symmetry on heating. This result has been confirmed by single-crystal diffraction. The phase transition at T_{C2} is of likely second order character. This character has been confirmed by TMA experiment on a single crystal. Powder neutron diffraction data indicate that the IP is polar with $P6_3cm$ symmetry. We show experimentally that this IP is stable within a temperature range $T_{C1} \simeq 1100K$ to $T_{C2} \simeq 1300K$. The powder data can be best fitted using a Y_2 disorder model. Below T_{C1} the Y_2 site becomes fully ordered. In opposition to these results, band structure calculations suggest a proper ferroelectric mechanism (paraelectric IP) taking place at T_{C1}.

Consequently, we can describe the system as a succession of three phases. The IP is clearly evidenced between T$_{C1}$ ≃1100K and T$_{C2}$ ≃1300K. The order of the transition at T$_{C2}$ is likely to be second order. In the IP, there is competition between parallel and antiparallel Y$_2$ dipoles. The polarization can be described by a tilting of the MnO$_5$ polyhedra due to displacements of the basal oxygens in the Y polyhedra. The displacement patterns at T$_{FE}$ for both scenarios (improper or proper ferroelectric) are similar. Thus our experimental data support the scenario of Fennie *et al.* who proposed a polar intermediate state followed by a strain driven transition towards the room temperature ferrielectric phase.

However, there are some unresolved issues. For instance, the effect of strain on the nature of the IP is unclear. Additionally, further work is needed in the study of the effect of vacancies on the ferroelectric transition in YMnO$_3$. This further work could clarify the spread of the transition temperatures reported in the literature and give the final input to more than 50 years of research.

References

[1] Z. J. Huang, Y. Cao, Y. Y. Sun, Y. Y. Xue, and C. W. Chu, Phys. Rev. B **56**, 2623 (1997)

[2] M. N. Iliev and H.-G. Lee, Phys. Rev. B **56**, 2488 (1997)

[3] M. Fiebig, Th. Lottermoser, D. Fröhlich, A. V. Goltsev and R. V. Pisarev, Nature **419**, 818 (2002)

[4] B. Lorenz, A. P. Litvinchuk, M. M. Gospodinov, and C. W. Chu, Phys. Rev. Lett. **92**, 87204 (2004)

[5] J. Wang *et al.*, Science **299**, 1719 (2003);Kimura *et al.*, Nature **426**, 55 (2003) and Hur *et al.*, Nature **429**, 392 (2004)

[6] Jean-Claude Peuzin, C. R. Acad. Sc. Paris, **261**, 2195 (1965)

[7] K. Lukaszewicz *et al.*, Ferroelectrics **7**, 81 (1974)

[8] I. G. Ismailzade *et al.*, Sov. Phys. Solid State, **70**, 236 (1965)

[9] T. Katsufuji, M. Masaki, A. Machida, M. Moritomo, K. Kato, E. Nishibori, M. Takata, M. Sakata, K. Ohoyama, K. Kitazawa, and H. Takagi, Phys. Rev. B **66**, 134434 (2002)

[10] B. van Aken,T.T.M. Palstra, A. Filippetti and N. A. Spaldin, Nature Materials **3**, 164 (2004)

[11] T. Lonkai, D. G. Tomuta, U. Amann, J. Ihringer, R. W. A. Hendrikx, D. M. Többens, and J. A. Mydosh, Phys. Rev. B **69**, 134108 (2004)

[12] C. J. Fennie and K. M. Rabe, Phys. Rev. B **72**, 100103 (2005)

[13] Coeure *et al.* Proceedings of the International Meeting on Ferroelectricity, **1**, 332 (1966)

[14] Y. Aikawa, T. Katsufuji, T. Arima, and K. Kato, Phys. Rev. B **71**, 184418 (2005)

[15] B. B. van Aken, A. Meetsma and T. T. M. Palstra, Acta Cryst. C **57**, 230-232 (2001)

[16] Bertaut *et al.* C. R. Acad. Sci. Paris, **256**, 1958 (1963)

[17] Bokov *et al.* Sov. Phys. Solid State, **5**, 2646, (1964)

[18] Smolenskii *et al.* J. Appl. Phys., **35**,915, (1964)

[19] S. C. Abrahams, Acta Cryst. B**57**, 485 (2001)

[20] H. T. Stokes and D. M. Hatch, (2002). ISOTROPY, stokes.byu.edu/isotropy.html

[21] M. I. Aroyo and J. M. Perez-Mato, Acta Cryst. A (1998) **54**, 19-30

[22] H. T. Stokes et al., Phys. Rev. B **65**, 64105 (2002)

[23] T. Chatterji et al. Phys. Rev. B **68**, 052406 (2003); T. Maitra, P. Thalmeier, and T. Chatterji Phys. Rev. B **69**, 132417 (2004); L. Martín-Carrón and A. de Andrés Eur. Phys. J. B **22**, 11-16 (2001).

[24] J. H. Kobeyashi and T. Sakudo, in *Numerical Data and Relationships in Science and Technology, Landolt-Bornstein, New Series, Group III*, Vol. 9 edited by K. H. Hellwege (Springer, New York, 1987).

[25] A. Guelylah et al. Acta. Cryst. B, **56**, 921 (2000)

[26] C. Capillas, E. Kroumova, M. I. Aroyo, J. M. Perez-Mato, H. T. Stokes and D. M. Hatch, J. Appl. Cryst. **36** 953 (2003).

[27] Crystallographic groups, T. Janssen, North-Holland publishing company, 1973

[28] Program CORREL, Bilbao crystallographic server http://www.cryst.ehu.es/

[29] D. Higashiyama *et al.*, Phys. Rev. B **70**, 174405 (2004); D. Pociecha *et al.*, Phys. Rev. Lett. **86**, 3048 (2001); B. Lorenz *et al.*, Phys. Rev. B **71**, 014438 (2005)

[30] The Landau Theory of Phase Transitions, J.-C. Tolédano and P. Tolédano, World Scientific, 1987

[31] V. P. Sakhnenko and V. M. Talanov, Sov. Phys. Solid State, **21**, 1401 (1979)

[32] D. Tomuta, PhD Thesis (2003), Leiden, The Netherlands

[33] A. C. Larson and R. B. von Dreele, General Structure Analysis System GSAS, Los Alamos National Laboratory Report No. LAUR 86-748, 1994 (unpublished).

[34] Sheldrick, G.M. (2001). SADABS. Version 2. Multi-Scan Absorption Correction Program. University of Gttingen, Germany

[35] Bruker (2000). SMART, SAINT, SADABS, XPREP and SHELXTL/NT. Area Detector Control and Integration Software. Smart Apex Software Reference Manuals. Bruker Analytical X-ray Instruments. Inc., Madison, Wisconsin, USA

[36] FIT2D V10.3, A. P. Hammersly/ESRF 1987-1998.

[37] A. Le Bail, H. Duroy and J.L. Fourquet, Mat. Res. Bull. **23** 447 (1988)

[38] Comprehensive Supramolecular Chemistry, vol. 8, Physical methods in Supramolecular Chemistry, Edited by J. Eric D. Davies and John A. Ripmeester (1996)

[39] P. Navard and J. M. Haudin, J. Thermal Analysis **30**, 61 (1985)

[40] J. E. Medvedeva, V. I. Anisimov, M. A. Korotin, O. N. Mryasov and A. J. Freeman, J. Phys.: Condens. Matter **12**, 4947 (2000)

[41] K. Terakura, T. Oguchi, A. R. Williams, and J. Klüber, Phys. Rev. B **30**, 4734 (1984); Z.-X. Shen, R. S. List, D. S. Dessau, B. O. Wells, O. Jepsen, A. J. Arko, R. Barttlet, C. K. Shih, F. Parmigiani, J. C. Huang, and P. A. P. Lindberg, Phys. Rev. B **44**, 3604 (1991)

[42] V. I. Anisomov, J. Zaanen, and O. K. Andersen, Phys. Rev. B **44**, 943 (1991); V. I. Anisimov, I. V. Solovyev, M. A. Korotin, M. T. Czyzyk, and G. A. Sawatzky, Phys. Rev. B **48**, 16 929 (1993)

[43] A. D. Becke, Phys. Rev. A **38**, 3098 (1998)

[44] C. Lee, W. Yang and R. G. Parr, Phys. Rev. B **37**, 785 (1988)

[45] V. R. Saunders, R. Dovesi, C. Roetti, R. Orlando, C. M. Zicovich-Wilson, N. M. Harrison, K. Doll, B. Civalleri, I. J. Bush, Ph. D'Arco, M. Liunell, CRYSTAL2003 User's Manual, University of Torino, Torino(2003).

[46] T. Bredow and A. R. Gerson, Phys. Rev. B **61**, 5194 (2000); J. Muscat, A. Wander, and N. M. Harrison, Chem. Phys. Lett. **342**, 397 (2001); I. de P. R. Moreira, F. Illas, and R. L. Martin, Phys. Rev. B **65**, 155102 (2002)

[47] M. Alfredsson, G.D. Price, C.R.A. Catlow, S.C. Parker, R. Orlando, J.P. Brodholt Phys. Rev. B **70**, 165111 (2004); E. M. Alfredsson, J.P. Brodholt, P.B. Wilson, G.D. Price, F. Cora, A. Calleja, R. Bruin, L.J. Blanshard, R.P. Tyer, Mol. Simulat. **31**, 367 (2005); F. Cora, MOL. PHYS. **103**, 2483(2005); T. Bredow and A. R. Gerson, Phys. Rev. B **61**, 5194 (2000); I. de P. R. Moreira, F. Illas, and R. L. Martin, Phys. Rev. B **65**,155102 (2002); T. Bredow, K. Jug, R.A. Evarestov, Phys. Status Solidi B **243**, R10 (2006)

[48] T. Bredow, K. Jug, R.A. Evarestov, Phys. Status Solidi B **243** R10 (2006)

[49] I. de P. R. Moreira, F. Illas, and R. L. Martin, Phys. Rev. B **65**, 155102 (2002); D. Munoz, N.M. Harrison, F. Illas Phys. Rev. B **69**, 085115 (2004)

[50] P. J. Hay, W. R. Wadt J. Chem. Phys. **82**, 299 (1985)

[51] H. J. Monkhorst and J. D. Pack, Phys. Rev. B **13**, 5188 (1967)

[52] J. Park, J.-G. Park, Gun Sang Jeon, Han-Yong Choi, Changhee Lee, W. Jo, R. Bewley, K. A. McEwen, and T. G. Perring, Phys. Rev. B **68**, 104426 (2003)

[53] H. L. Yakel, W. C. Kochler, F. Bertaut, E. Forrat, Act. Cryst. **16**, 957 (1963)

[54] S. C. Abrahams, S. K. Kurtz and P. B. Jamieson, Phys. Rev. **172**, 551 (1968)

Chapter 5

Interplay between polarization and dielectric properties

5.1 Magnetodielectric coupling in an organic-inorganic hybrid

5.1.1 Introduction

While both organic and inorganic materials can be polar or magnetic, the combined properties rarely occur in either class of materials. Here, we introduce a hybrid material in which the polar symmetry originates from the organic component, while the magnetism comes about from the 3d transition metal ions Cr^{2+}. Using such hybrid materials is a significant new approach in which the dielectric and magnetic properties can be tuned individually. Thus, this also provides a new method to tune the magnetodielectric coupling in a systematic manner.

$Cr[(H_3N-(CH_2)_2-PO_3)(Cl)(H_2O)]$ (**I**) is a rare polar organic-inorganic hybrid example. **I** contains Cr^{2+} ions which order magnetically at low temperature. It crystallizes in the polar space group $P2_1$ (n°4) with a=5.249(1)Å, b=14.133(3) Å, c=5.275(1)Å, and β=105.55(2)° [1] (see figure 5.1). Electrostatic interactions as well as hydrogen bonds ensure the cohesion of the 3D structure. The magnetic susceptibility data in the temperature range from 300 to 50 K show Curie-Weiss behavior, with C=2.716 cm^3K.mol^{-1} and a Weiss constant θ= -2.2 K. Hysteresis loops taken at different temperatures show that **I** behaves as a canted antiferromagnet below T_N=5.5 K with a coercive field and a remnant moment of 30 Oe and 0.08 μ_B, respectively at 4.5K [1]. Two main reasons have motivated this work: the first one is that polar molecule based materials may show some interesting phenomena (pyroelectricity, non linear optical effect, etc) [2]. The second one resides in the fact that magnetodielectric coupling studies of polar materials

are focused mainly on inorganic multiferroic metal-oxides [3, 4, 5, 6, 7, 8]. Our aim here is twofold: to investigate the magnetodielectric coupling in a polar organic-inorganic hybrid material and to discuss our results in comparison with some well known magnetodielectric compounds. Indeed, this is particularly of interest since $YMnO_3$ like **I** presents one unique polar axis, both are antiferromagnetic but with a small ferromagnetic component for the latter. In addition, we use a Landau approach which explains the temperature dependence of the dielectric constant (ε). It is similar to previous studies [7]. The other features of the magnetodielectric coupling are explained using classical mechanics. We derive a relationship that quantifies the decrease of ε below T_N. In addition, we show that the departure from a quadratic dependence in magnetic field of ε is not necessarily due to magnetic fluctuations. This is in disagreement with recent claims [5].
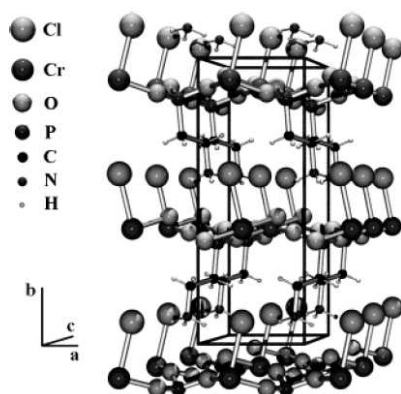

Figure 5.1: *Structure of Cr[(H₃N-(CH₂)₂-PO₃)(Cl)(H₂O)].*

5.1.2   Experimental section

I has been synthesized according to a previous published paper [1]. The resulting light-blue microcrystalline solid was finely ground under inert atmosphere. The fine blue powder was then introduced in a stainless-steel die (Perkin Elmer) and pressed under vacuum (10^{-2} mm Hg) at a pressure of 12 t. A cylindrical shaped blue pellet of 1.5 mm thickness and 8 mm radius was obtained and stored under inert atmosphere[1].

Complex impedance measurements were performed using an Agilent AG4284A LCR meter. In order to measure the dielectric constant in the presence of a magnetic field, a home made sample holder with four coaxial cables was used. The sample holder fits inside a commercial Quantum Design PPMS apparatus, allowing measurements of the dielectric constant in

---

[1]The sample was provided by Elvira M. Bauër, Carlo Bellitto and Guido Righini from the CNR-Istituto di Struttura della Materia, Monterotondo Stazione, Roma, Italy.

the presence of a magnetic field up to 9T and at different temperatures. The ac-voltage applied to the sample was set at 1 Volt. The dielectric constant can be extracted from the value of capacitance using the sample dimensions.

5.1.3 Results and Discussion

The dielectric constant of a pellet of **I** was measured as a function of temperature, T, and of frequency, f, with 0.25 K step. We observed a shift towards higher value of the dielectric constant for f = 1kHz while the two other frequencies (f = 10kHz and f = 100kHz) do not show noticeable difference. In addition, we see that the measurement with f = 1kHz is significantly more noisy than for the other frequencies. For all the studied frequencies, the loss is quite low ($\tan(\delta)$ <0.01). The loss for f = 1kHz is more noisy than for the other frequencies.

Based on the frequency dependence studies, we chose to use a 10kHz frequency for our measurement. We present in figure 5.2 the temperature dependence of ε measured with 0.25K step. We observe clearly an anomaly at the Néel temperature. The anomaly is evidenced by a decrease below the Néel temperature. This anomaly demonstrates for the first time, to our knowledge, the existence of a magnetodielectric coupling in a polar organic-inorganic hybrid material. We notice that the anomaly is significantly less pronounced than in other magnetodielectric compounds (see table 5.1). In order to compare our data, we have normalized the variation of ε to the magnetic transition temperature.
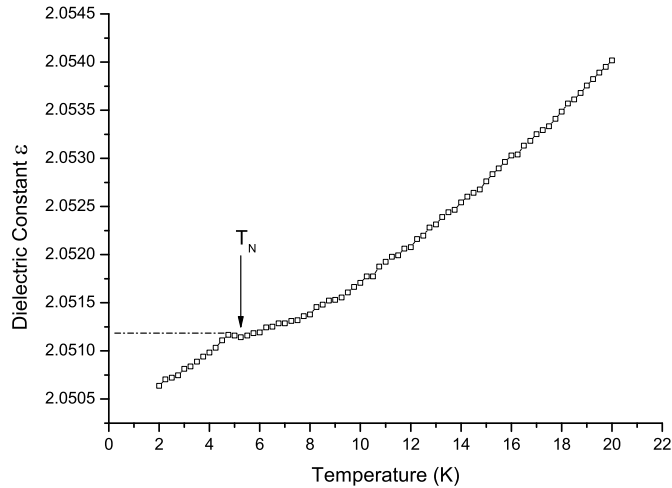

Figure 5.2: *Dielectric constant measured versus temperature. A clear anomaly is observable below T_N (f = 10kHz).*

In order to investigate the magnetic field dependence of the magnetodielectric coupling, we have performed magnetocapacitance measurement under a magnetic field up to 5T below and above T_N=5.5K. The results are presented in figure 5.3. We show that both magnetocapacitive responses below and above T_N follow a quadratic dependence in magnetic field, at least up to a field of 3T. The significant difference in the magnetocapacitive responses below (T=4.2K) and above T_N (T=10K) can be explained by the onset of the magnetic ordering (see section 5.1.4). The increase of the magnetocapacitive response below T_N is almost one order in magnitude between 4.2 and 10K ($\Delta\varepsilon/\varepsilon_{(H=0)}$=a + b$H^2$, $b_{T<T_N}/b_{T>T_N} = 2.1\times10^{-2}/2.4\times10^{-3}$= 8.75).

Compound	$\frac{\Delta\varepsilon}{\varepsilon}$ at $H = 5T$	$\frac{\Delta\varepsilon}{\varepsilon}$ per K	$b_{T<T_N}$	T_N (K)
EuTiO$_3$ [4]	$\approx 6\%$	1%	2.74×10^{-3}	5.5
ε-Fe$_2$O$_3$ [6]	0.26%	0.05%	5.2×10^{-2}	110
YMnO$_3$ [8]	0.005%	9.1%	$\approx 2\times10^{-4}$	77
this work	0.0275%	0.0085%	2.1×10^{-2}	5.5

Table 5.1: *Different relevant magnetodielectric parameters for several compounds compared to Cr^{II} organophosphonate. $\frac{\Delta\varepsilon}{\varepsilon}$ at $H = 5T$ is given below the magnetic ordering temperature. $\frac{\Delta\varepsilon}{\varepsilon}$ per K is the variation of the ε normalized to $\Delta T = T_N - T_{low}$ where T_{low} is the lowest measured temperature. $b_{T<T_N}$ corresponds to the curvature of $\Delta\varepsilon/\varepsilon_{(H=0)}$=a + b$H^2$.*

In **I** the magnetic field response of ε below T_N is almost one order of magnitude larger than above T_N. This is not the case in YMnO$_3$ where the magnetocapacitive response is almost constant below and above T_N [8]. We will show in the section 5.1.4 that this increase in the magnetodielectric coupling is due to the arising of the magnetic ordering below T_N. While the field dependence of our sample is quite small above T_N, the magnetodielectric constant $b_{T<T_N}$ in the magnetically ordered phase is larger by two orders of magnitude than for YMnO$_3$ or EuTiO$_3$ (see table 5.1). We notice also from table 5.1 that b is not related to the magnetic transition temperature.
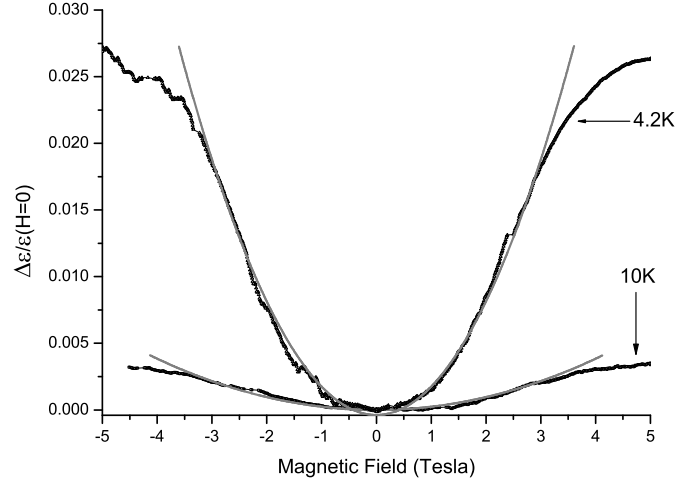
Figure 5.3: *Magnetocapacitance measured below and above $T_N = 5.5K$ (f = 10kHz). In black, we present the field dependence at 4.2K and at 10K. In grey, we show the fit with $\Delta\varepsilon/\varepsilon_{(H=0)}=a + bH^2$.*

5.1.4 A phenomelogical description

In this section, we develop a phenomelogical approach based on symmetry analysis and in the framework of Landau theory [9]. We will show that we can describe the main features of ε as function of magnetic field and temperature:
- Quadratic dependence of ε in magnetic field
- b coefficient higher below T_N ($\varepsilon=a+bH^2$)
- Decrease of ε below T_N

I crystallizes in the space group $P2_1$ (n°4) where there is only one Cr^{2+} per asymmetric unit cell occupying the general Wyckoff position 2a. Consequently, there are two Cr atoms per unit cell at (x, y, z) (carrying $\overrightarrow{S_1}$ moment) and at (-x, y+1/2, -z) (carrying $\overrightarrow{S_2}$ moment).

Consequently, we can define 2 magnetic vectors:

$$\overrightarrow{M} = \overrightarrow{S_1} + \overrightarrow{S_2} \tag{5.1}$$

$$\overrightarrow{L} = \overrightarrow{S_1} - \overrightarrow{S_2} \tag{5.2}$$

The space group $P2_1$ contains only two symmetry elements the identity 1 and a two fold screw axis 2_1 that we will denote h_1 and h_2, respectively. The matrix expressions of these two elements of symmetry are:

$$
\mathbf{h_1} = \begin{pmatrix} 1 & 0 & 0 & 0 \\ 0 & 1 & 0 & 0 \\ 0 & 0 & 1 & 0 \\ 0 & 0 & 0 & 1 \end{pmatrix} \quad \mathbf{h_2} = \begin{pmatrix} -1 & 0 & 0 & 0 \\ 0 & 1 & 0 & 1/2 \\ 0 & 0 & -1 & 0 \\ 0 & 0 & 0 & 1 \end{pmatrix}
$$

The magnetic ordering which develops below T_N=5.5K is characterized by the presence of a ferromagnetic component giving rise to a canted antiferromagnet. Although the magnetic structure has not been studied by neutron diffraction, we can consider the simplest case where the magnetic cell is identical to the chemical one. Indeed having two Cr^{2+} sites per unit cell, one can easily imagine an antiferromagnetic coupling between these two sites. Consequently, the irreducible representations (IR) associated with this wave-vector ($\overrightarrow{k} = \overrightarrow{0}$) are the same as the ones of point-group 2 (see table 5.2).

	h_1	h_2	Rh_1	Rh_2
Γ_1	1	1	-1	-1
Γ_2	1	-1	-1	1

Table 5.2: *Irreducible representations for the space group $P2_11'$ associated with* **k**=0.

In order to know which components of the different magnetic vectors belong to which IR, we need to look at the effect of the symmetry elements on the position of the atoms.

$$
h_2 = \begin{pmatrix} -1 & 0 & 0 & 0 \\ 0 & 1 & 0 & 1/2 \\ 0 & 0 & -1 & 0 \\ 0 & 0 & 0 & 1 \end{pmatrix} \times \begin{pmatrix} x \\ y \\ z \\ 1 \end{pmatrix} = \begin{pmatrix} -x \\ y+1/2 \\ -z \\ 1 \end{pmatrix}
$$

Since h_1 keeps the whole system invariant, we can simply write the following table (see table 5.3)

	h_1	h_2
(x, y, z)	(x, y, z)	(-x, y+1/2, -z)
(-x, y+1/2, -z)	(-x, y+1/2, -z)	(x, y, z)

Table 5.3: *Transformation properties of the symmetry elements on the Wyckoff positions 2a in the space group $P2_1$.*

Table 5.3 gives us the permutational representations of the two symmetry elements h_1 and h_2. In order to be able to write down the free-energy, we need to determine the axial representations of the group. We can derive

this representation by using the matrix representations of the different symmetry elements (see above). For this purpose, we use $\tilde{V}(h_i) = \text{Det}(h_i) \times h_i$, where Det is the determinant of the matrix representation of the rotational part of the symmetry element. Since for h_1 and h_2 the determinant is 1, the axial representations are given by:

$$\tilde{\mathbf{V}}(\mathbf{h_1}) = \begin{pmatrix} 1 & 0 & 0 \\ 0 & 1 & 0 \\ 0 & 0 & 1 \end{pmatrix} ; \tilde{\mathbf{V}}(\mathbf{h_2}) = \begin{pmatrix} -1 & 0 & 0 \\ 0 & 1 & 0 \\ 0 & 0 & -1 \end{pmatrix}$$

Thanks to the table 5.3 and the expressions of $\tilde{V}(h_i)$, we can associate to each magnetic component an IR. The results are presented in table 5.4.

Γ_1	L_x, L_z, M_y
Γ_2	L_y, M_x, M_z

Table 5.4: *Components of the **M** and **L** vectors which form a basis for the IR of $P2_1 1$' at **k**=0.*

The results of table 5.4 allow us to construct the Landau free-energy, separating the exchange and magnetic anisotropy energies. We write the exchange terms up to the fourth degree and the relativistic terms up to the second degree:

$$\begin{aligned}
F = {} & F_0 + \frac{a}{2}L^2 + \frac{b}{4}L^4 + \frac{c}{2}M^2 + \frac{d}{4}M^4 \\
& + \frac{1}{2}\sum_{i=x,y,z} (\nu_i L_i^2 + \beta_i M_i^2) \\
& + \delta L_x L_z + \gamma M_x M_z \\
& + \sigma_1 L_x M_y + \sigma_2 L_z M_y + \sigma_3 L_y M_z + \sigma_5 L_y M_x
\end{aligned} \tag{5.3}$$

The first line in equation 5.3 represents the exchange energy. It is formed from the scalar products $\vec{L}^2 = \vec{L} \cdot \vec{L}$ and $\vec{M}^2 = \vec{M} \cdot \vec{M}$. The other lines in equation 5.3 correspond to the relativistic terms. We have separated in the magnetic anisotropy term the δ which couples different antiferromagnetic components L_i, from the σ_j terms which couple the total magnetization components M_i to the L_i and γ which couples the total magnetization components M_x and M_z. We are now able to discuss in a complete manner the type and nature of the magnetic order which arise below T_N.

Most of the magnetic phase transitions involve only one IR. We know that below T_N, we have antiferromagnetic interactions. Thus, looking at table 5.4, there are two possibilities for the antiferromagnetic ordering, either with magnetic moments in the (*ac*) plane or along the *b* axis. Since the

closest next neighbors of Cr^{II} are within the (ac) plane, the strongest magnetic coupling will be in this plane. However, it is not sufficient to decide what is the most likely direction of the spins. It can be shown that the discussion will not be much changed irrespective of the spin directions. Thus, we decide arbitrarily to assume that the antiferromagnetic components are in the (ac) plane. In this hypothesis, we can rewrite the free-energy in its simplest form as:

$$
\begin{aligned}
F = F_0 &+ \frac{a}{2}L^2 + \frac{b}{4}L^4 + \frac{1}{2}\sum_{i=x,y,z}\nu_i L_i^2 \\
&+ \delta L_x L_z + \sigma_1 L_x M_y + \sigma_2 L_z M_y + \frac{c}{2}M^2
\end{aligned}
\tag{5.4}
$$

Minimization of F gives:

$$
\begin{aligned}
\frac{\partial F}{\partial L_x} &= aL_x + bL_x^3 + \nu_x L_x + \delta L_z + \sigma_1 M_y = 0 \\
\frac{\partial F}{\partial L_y} &= aL_y + bL_y^3 + \nu_y L_y = 0 \\
\frac{\partial F}{\partial L_z} &= aL_z + bL_z^3 + \nu_z L_z + \delta L_x + \sigma_2 M_y = 0 \\
\frac{\partial F}{\partial M_y} &= \sigma_1 L_x + \sigma_2 L_z + cM_y = 0
\end{aligned}
\tag{5.5}
$$

Below T_N, we see from the expression of the free energy (equation 5.5) that the minimum of F arises for non zero value of M_y. Thus an induced magnetization can occur. A detailed neutron study below T_N could give more informations on the origin of the ferromagnetic component in **I**. Now that we have described a possible origin of the weak ferromagnetic properties of **I**, we will have a look at the decrease of the capacitance at T_N.

We present in figures 5.2 and 5.3, the magnetodielectric measurement of a pellet of **I**. Let's try to justify the above point that we observed experimentally. For this purpose, we note the ferromagnetic component **M** and $\mathbf{L}_s$ the antiferromagnetic vector describing the antiferromagnetic ordering below T_N. We use only relevant terms as derived above. Thus, we can write the free-energy to investigate the magnetodielectric coupling as:

$$
\begin{aligned}
F = F_0 &+ \frac{a}{2}L_s^2 + \frac{b}{4}L_s^4 + \sigma_1 L_s M_y \\
&+ \frac{1}{2\chi_p}P^2 - PE + \gamma_1 L_s^2 P^2 + \gamma_2 M_y^2 P^2
\end{aligned}
\tag{5.6}
$$

χ_p is the dielectric tensor of the polar paramagnetic phase of the material. We do not put term like P^4 since we are not interested in the ferroelectric transition. If we differentiate F respect to P, we have:

$$\frac{\partial F}{\partial P} = \frac{P}{\chi_p} + 2\gamma_1 L_s^2 P + 2\gamma_2 M_y^2 P - E = 0$$
$$\Longleftrightarrow \frac{1}{\chi_p}\frac{\partial P}{\partial E} + 2\gamma_1 L_s^2 \frac{\partial P}{\partial E} + 2\gamma_2 M_y^2 \frac{\partial P}{\partial E} - 1 = 0 \qquad (5.7)$$
$$\Longleftrightarrow \frac{\partial P}{\partial E} = \frac{1}{\frac{1}{\chi_p} + 2\gamma_1 L_s^2 + 2\gamma_2 M_y^2}$$

We note that the equation 5.7 assumes that $\mathbf{L}_s$ does not depend on the electric field $\mathbf{E}$. The total dielectric susceptibility is defined as $\chi_e = \frac{\partial P}{\partial E}$ and the dielectric constant as $\varepsilon = 1 + \chi_e$. Consequently:

$$- T > T_N (L_s = 0 \quad and \quad M_y = 0) \longrightarrow \frac{\partial P}{\partial E} = \chi_p$$
$$- T < T_N (L_s \neq 0 \quad and \quad M_y \neq 0) \longrightarrow \frac{\partial P}{\partial E} = \frac{\chi_p}{1 + 2\gamma_1 \chi_p L_s^2 + 2\gamma_2 \chi_p M_y^2} \qquad (5.8)$$

We can define the variation of the dielectric constant $\Delta\varepsilon$ as function of temperature:

$$\Delta\varepsilon = \frac{\partial P}{\partial E}_{(T>T_N)} - \frac{\partial P}{\partial E}_{(T<T_N)}$$
$$= \chi_p - \frac{\chi_p}{1 + 2\gamma_1 \chi_p L_s^2 + 2\gamma_2 \chi_p M_y^2} \qquad (5.9)$$
$$= \frac{2\gamma_1 \chi_p^2 L_s^2 + 2\gamma_2 \chi_p^2 M_y^2}{1 + 2\gamma \chi_p L_s^2 + 2\gamma_2 \chi_p M_y^2}$$

Since we have a weak ferromagnetic component, we can express $\mathbf{L}_s$ as function of M$_y$. This is given in equation 5.10.

$$\frac{\partial F}{\partial M_y} = \sigma_1 L_s + 2\gamma_2 M_y P^2 = 0 \longrightarrow L_s = \frac{-2\gamma_2 M_y P^2}{\sigma_1} \qquad (5.10)$$

Using the results of equation 5.10 to put in equation 5.9, we obtain the following expression:

$$\Delta\varepsilon = \frac{\gamma_2\chi_p^2 M_y^2(8\gamma_1\gamma_2 P^4 + 2\sigma_1^2)}{\sigma_1^2 + \gamma_2\chi_p M_y^2(8\gamma_1\gamma_2 P^4 + 2\sigma_1^2)}$$

$$if \quad we \quad assume \quad that \quad 8\gamma_1\gamma_2 P^4 \ll 2\sigma_1^2 \qquad (5.11)$$

$$\Delta\varepsilon \simeq \frac{2\gamma_2\chi_p^2 M_y^2}{1 + 2\gamma_2\chi_p M_y^2}$$

Using the last expression of equation 5.11, we can explain all the characteristics of ε as function of temperature and magnetic field. Assuming that $\gamma_2 > 0$ and taking into account that $\mathbf{M} = \chi_{mag}\mathbf{H}$, we see that ε varies for low magnetic field ($1 \gg 2\gamma_2\chi_p M_y^2$) as H^2 in agreement with our experimental observations. Moreover, the b coefficient in $\varepsilon = a + bH^2$ is proportional to χ_{mag}^2. χ_{mag} is higher below T_N than above T_N. Therefore we can explain the increase of b below T_N.

We see that the variation of the dielectric constant is directly related to the square of the magnetic moment. Consequently if one plots $\Delta\varepsilon$ as function of the square of the magnetic moment, we will find a linear dependence for magnetic field. This behavior has been reported for various compounds such as $EuTiO_3$ [4], $\varepsilon - Fe_2O_3$ [6] and $YMnO_3$ [8]. However, it is not the case for compounds presenting large magnetic fluctuations such as $R_2Ti_2O_7$ [5]. Katsufuji *et al.* show that the relationship above is not fulfilled below the temperature where the magnetic fluctuations start to develop. This is justified by the fact that $\langle\mathbf{S}_i.\mathbf{S}_j\rangle$ (pair correlation of neighboring spins) cannot be replaced by the square of the spin moments $|\langle S\rangle^2|$ if magnetic fluctuations are present. However, as shown from Landau theory, the quadratic dependence in magnetic field is an approximation. A fuller expression would include term like $1 + \gamma_2\chi_p M_y^2$ in the denominator of ε. Consequently, a deviation from the quadratic dependence in magnetic field of the magnetocapacitance response can arise if a more complete expression is taken into account. Consequently, the deviation from quadratic dependence in magnetic field may not be systematically due to magnetic fluctuations.

5.1.5   Conclusion

We have investigated the magnetodielectric coupling of polar organic-inorganic hybrid material. We show that the magnetodielectric response is enhanced by almost one order of magnitude below T_N between 4.2 and 10K due the appearance of long range magnetic ordering. We discuss the common and different features with well-known magnetodielectric compounds. In addition to these experimental observations, we elaborate a Landau approach

which enables us to describe the main characteristics of the magnetodielectric response: quadratic dependence in the magnetic field, increase of the magnetodielectric coupling below T$_N$ and the decrease of the dielectric constant below T$_N$.

5.2 Magnetoelectricity in Ho$_2$BaNiO$_5$ Haldane gap system

5.2.1 Introduction

Interest in low dimensional magnetism was greatly renewed by the theoretical work of Haldane, who predicted that an integer-spin Heisenberg antiferromagnetic chain should have a singlet ground state, and a gap in the magnetic spectrum [12]. Several examples of quasi-one dimensional systems with a Haldane gap have been studied by now (see ref. [13] and references therein). Most of the work has been carried out on organometallic compounds [14].

Darriet and Regnault [15] and DiTusa *et al.* [16] were the first to observe a Haldane gap in a metal oxide compound, namely, Y$_2$BaNiO$_5$. The R$_2$BaNiO$_5$ (R = rare-earth or Y) oxides present interesting structural and magnetic properties due to the fact that their structure posses a strong 1D character [17, 18]. As a function of R and the synthesis conditions, the R$_2$BaNiO$_5$ family can crystallize in two different polymorphs: *P*nma (n°62) and *I*mmm (n°71) [19, 20]. The members in which we are interested have the *I*mmm symmetry. The main structural feature is the presence of 1D chains of NiO$_6$ octahedra along the *a*-axis. The octahedra are strongly distorted with a very short Ni-O$_{apical}$ distance ($\approx$ 1.88Å), and a longer Ni-O$_{basal}$ distance ($\approx$ 2.18Å) (see figure 5.4).

In particular, the R$_2$BaNiO$_5$ family is of interest from a magnetic point of view, due to the fact that the onset of 3D long-range magnetic order does not eliminate the Haldane-like behavior above and below the Néel temperature [21]. Our motivation in studying the Ho member of this family was triggered by two reasons: the existence of two field induced phase transitions at low temperature and the possible existence of magnetoelectricity. We will show in a first part that we predicted the presence of a linear magnetoelectric effect based on symmetry analysis. From this prediction, we have synthesized the compound and studied its magnetic properties. We finally demonstrate experimentally the presence of an induced polarization by application of a magnetic field (linear magnetoelectric effect) on a polycrystalline sample. We discuss the magnetic field behavior of the induced polarization in the light of the two unusual field induced phase transitions.
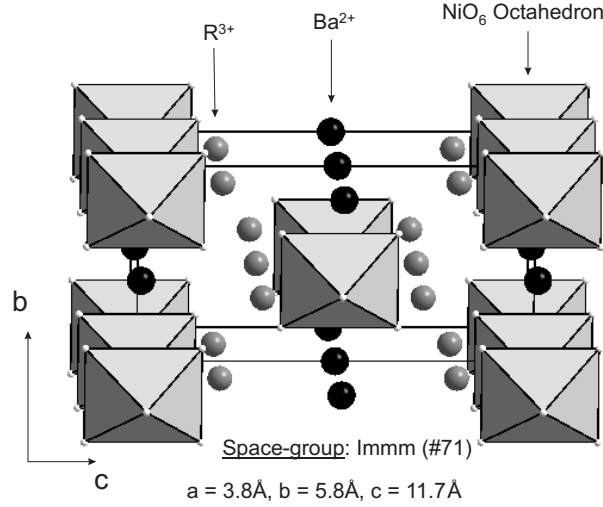
Figure 5.4: *Crystallographic structure of the R_2BaNiO_5 in the space group Immm. The cell parameters are a $\approx$ 3.8Å b $\approx$ 5.8Å and c $\approx$ 11.3Å for small R and c $\approx$ 11.7Å for large R*

5.2.2   Magnetic symmetry analysis

E. García-Matres *et al.* have studied the magnetic structures of most of the members of the R_2BaNiO_5 family using neutron powder diffraction (R = Nd, Tb, Dy, Ho, Er and Tm) [23]. Below T_N, Ho_2BaNiO_5 orders magnetically with a magnetic wave-vector $\overrightarrow{k}$ = (1/2, 0, 1/2). The Ni atoms occupy the Wyckoff position 2a and the Ho atoms occupy the Wyckoff position 4j with z $\approx$ 0.202. The authors determined the point-group of the little group G_k = 2/m. Using methods presented in chapter 2, they determined that Ho_2BaNiO_5 could be described by the B_g representation of the little group 2/m. Consequently, the magnetic moments of Ni and Ho ions are within the *ac*-plane. Let's have a look which terms are primed or unprimed. The easiest way is to describe the magnetic structure in the enlarged unit cell. Using the program ISOTROPY [24], an enlargement of the unit cell by a vector (1/2,0,1/2) gives rise to the space group Cmmm (n°65) with $\overrightarrow{a}' = 2\overrightarrow{c}$, $\overrightarrow{b}' = 2\overrightarrow{a}$ and $\overrightarrow{c}' = \overrightarrow{b}$. The new Wyckoff positions for Ni are (in Cmmm setting) 2a, 2b and 4f. The new Wyckoff positions for Ho are 8p, and 2 times 4h with different x coordinate in Cmmm setting.

   We know from the work of E. García-Matres *et al.* [23, 25] that the magnetic moments of Ni and Ho at 1.5K are $\overrightarrow{S_{Ni}}$ = (0.58(9), 0, -1.26(4)) and $\overrightarrow{S_{Ho}}$ = (0.12(5), 0, 9.06(4)), respectively. We consider only one propagation vector which defines the magnetic structure. Thus, we can relate

any magnetic moment in the structure by:

$$\vec{S_n} = \vec{S_k} exp(-i2\pi \vec{k}.\vec{R_n}) \qquad (5.12)$$

where $\vec{S_n}$ is the the magnetic moment of the atom considered attached to the lattice point $\vec{R_n}$ for a magnetic wave-vector $\vec{k}$. We investigate the 8 axial vector representations of the symmetry elements (we deal here with spins) of the space group Cmmm (in the enlarged unit cell). We find out that the only symmetry elements which remain are the two fold axis along y (in Cmmm symmetry) and the mirror m$_{xy}$ (in Cmmm symmetry) which is primed. Consequently, the magnetic point-group describing the magnetic order under T$_N$ is 2/m$'$. According to table 2.4, this compound may present a linear magnetoelectric effect. This prediction has been the motivation for an experimental investigation of Ho$_2$BaNiO$_5$.

5.2.3 Synthesis and characterization

The synthesis of Ho$_2$BaNiO$_5$ was already reported [20, 23, 25]. We follow a similar procedure for the synthesis of our sample. Ho$_2$BaNiO$_5$ was prepared as polycrystalline material by solid state reaction from stoichiometric mixtures of analytical grade Ho$_2$O$_3$ (dried at 1000°C overnight prior to use), NiO (99.999%) and BaCO$_3$. The sample was ground, pelletized and heated in air overnight at 900°C, 950°C, 1050°C and 1100°C until reaching X-ray pure sample. After each thermal treatment, the reaction products were reground and repelletized before starting the next treatment.

The quality of the sample was checked by means of powder X-ray diffraction using a Bruker D8 Advance diffractometer with an energy dispersive detector. Refinement of the powder data has been carried out using the program GSAS [22]. We use the peak profile function of type 2 in GSAS. Only three parameters have been used to describe the peaks shape with one Gaussian parameter, one Lorentztian parameter and the shift. The results of the refinement are presented in figure 5.5 and in table 5.5. We obtain very good refinement of the structure with the following statistics: GoF = 1.51, wR$_p$=3.28% and R$_p$=3.94% with cell parameters $a = 3.76010(5)$Å, $b = 5.75871(7)$Å, $c = 11.3275(1)$Å.

5.2.4 Magnetic properties

The magnetic properties have been investigated for two reasons: the magnetoelectric effect is dependent on the magnetic properties and two field induced phase transitions have been reported for Ho$_2$BaNiO$_5$. Checking for the existence of such transition is a good way to further investigate the quality of the sample, especially in terms of phase purity.
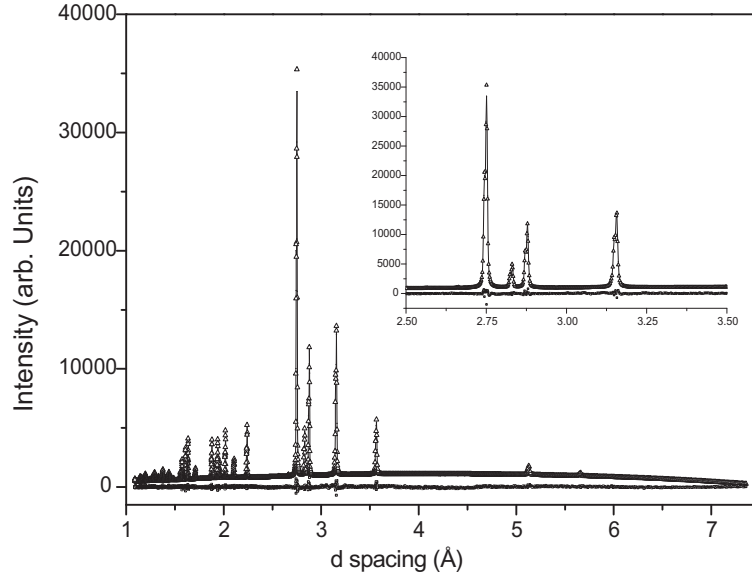
Figure 5.5: *Refinement of the crystal structure of Ho_2BaNiO_5 on a powder sample. The refinement was carried with Immm symmetry giving rise to the following statistics: GoF = 1.51, wR$_p$=3.28% and R$_p$=3.94%. Cell parameters: a = 3.76010(5)Å, b = 5.75871(7)Å, c = 11.3275(1)Å*

Atom	Wyckoff	x	y	z	U_{iso}
Ho	4j	0.5	0	0.7977(1)	0.0473(7)
Ba	2c	0.5	0.5	0	0.0490(8)
Ni	2a	0	0	0	0.049(1)
O_1	8l	0	0.766(1)	0.8500(5)	0.058(2)
O_2	2b	0	0.5	0.5	0.041(5)

Table 5.5: *Crystallographic coordinates extracted from the refinement carried out on X-ray powder diffraction.*

We present in figure 5.6, the magnetic field dependence of the magnetization measured at T = 5K in order to confirm the experimental observations [20, 23, 25]. We confirm the two field induced phase transitions at a slightly different value for H_{C2} (5.2T versus 5.4T) and exactly the same for H_{C1} (2.9T).

The magnetization for Ho_2BaNiO_5 reaches $\approx 1\mu_B$ at H_{C1} and $\approx 4.5\mu_B$ at H_{C2} per formula unit. From neutron measurements in zero magnetic field [25], the Ni moments are rotated 26° from the *c*-axis to the *a*-axis, and the Ho moment is almost collinear with the *c*-axis at 1.5K (0.7°). The Ni and Ho moments reach $1.4\mu_B$ and $9\mu_B$ at 1.5K, respectively. Thus, we observe that even at H_{C2}, we are still far from the saturated value of the magnetic moment of Ho. This is in contrast with Nd_2BaNiO_5. In this material, a full saturation of the rare-earth moment is reached at H_{C2} [26] while this is not
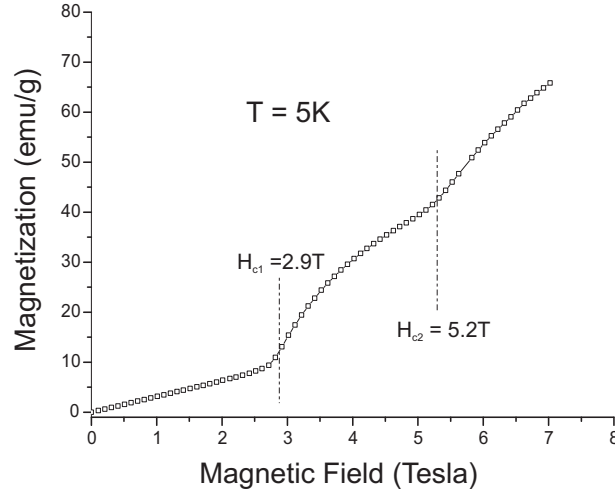
Figure 5.6: *Magnetic field dependence of the magnetization measured on a pellet of Ho$_2$BaNiO$_5$ at 5K. Two noticeable magnetic induced transitions are at H_{C1}=2.9T and at H_{C2}=5.2T*

the case for Ho in Ho$_2$BaNiO$_5$. From neutron diffraction, we expect that the scenario for Nd will also hold for Ho since both rare-earths order along the c axis. Experiments on single crystal of Ho$_2$BaNiO$_5$ could clarify the reasons for this discrepancy. In addition to the magnetization versus magnetic field, we measure also the temperature dependence of the magnetic susceptibility of a Ho$_2$BaNiO$_5$ pellet. The results are presented in figures 5.7 and 5.8.
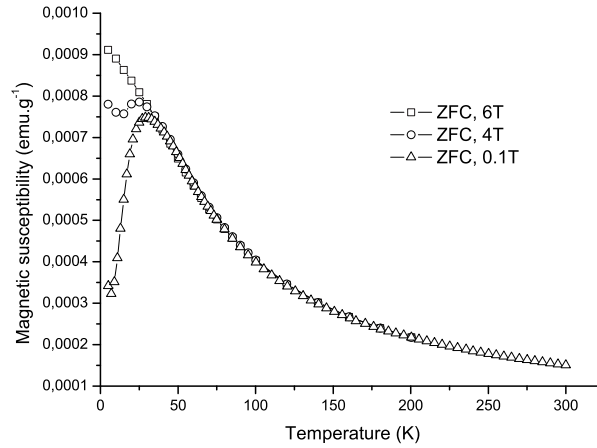
Figure 5.7: *Magnetic susceptibility measured on a Ho$_2$BaNiO$_5$ pellet in zero field cooled mode function for different applied magnetic fields: 0.1T (triangles), 4T (circles) and 6T (squares)*

The magnetic susceptibility data present the common features of the R$_2$BaNiO$_5$ family. There is a broad maximum at around 30K characteristic for all the family. Indeed, this broad maximum (maximum at χ_{max}) is

always present below T_N for any R (e.g. Er_2BaNiO_5, $T_{max} = 16K$ and T_N=33K) [27]. From neutron diffraction, it has been shown that there is a change of slope versus temperature in the Ho magnetic moment around 30K corresponding to χ_{max} in the magnetic susceptibility data [25]. In low-dimensional magnetic systems a maximum in magnetic susceptibility is not related to the 3D antiferromagnetic ordering.

In figure 5.8, we present the inverse susceptibility of a polycrystalline sample of Ho_2BaNiO_5 measured in zero field cooled mode with a magnetic field of 0.01T. We could fit the data in the paramagnetic phase using a Curie-Weiss dependence defined by $\frac{1}{\chi} = \frac{T+\theta}{C}$ between 200 and 300K. We find that Ho_2BaNiO_5 exhibits ferromagnetic interactions since θ is positive (θ=10.8K). In addition, the value of the Curie constant C=27.8 emu.K.mol^{-1} is in good agreement with the theoretical value of 28. It should be noted that at all temperatures the magnetic susceptibility is dominated by the contribution of the Ho^{3+} moments (p_{eff}=10.4μ_B, $C_{2Ho^{3+}}$=27 emu.K.mol^{-1}) being much larger than the contribution of the Ni^{2+} moments (p_{eff}=2.8μ_B, $C_{Ni^{2+}}$=1 emu.K.mol^{-1}). This means that in the paramagnetic regime the Ni^{2+} contribution is only about 4% of the total susceptibility.
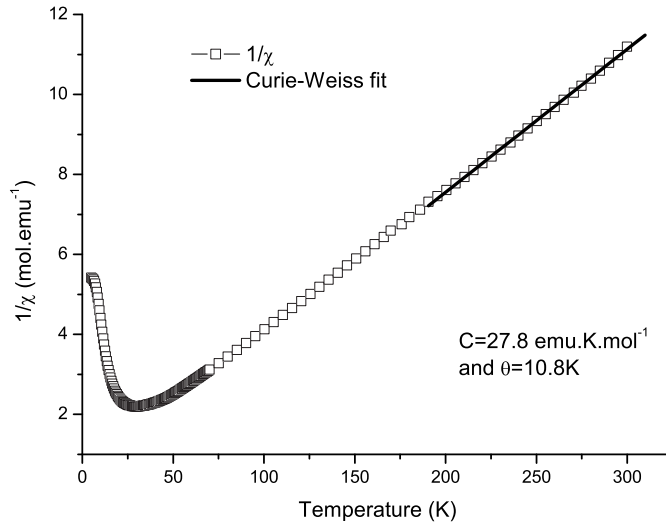

Figure 5.8: *Inverse magnetic susceptibility measured on a pellet of Ho_2BaNiO_5 in zero field cooled mode with 0.01T. The line is a fit of the Curie-Weiss function using $\frac{1}{\chi} = \frac{T+\theta}{C}$.*

Considering the derivative $d\chi/dT$, we notice an anomaly around 50K in agreement with the reported Néel temperature of T_N=53K [23, 25, 27] (see figure 5.9). Consequently, we ascribe this anomaly as the signature for the Néel temperature. The insufficient accuracy of our data for higher

magnetic fields does not allow, even by plotting dχ/dT, the determination of the magnetic ordering temperature. In first approximation, we assume that T$_N$ does not change.
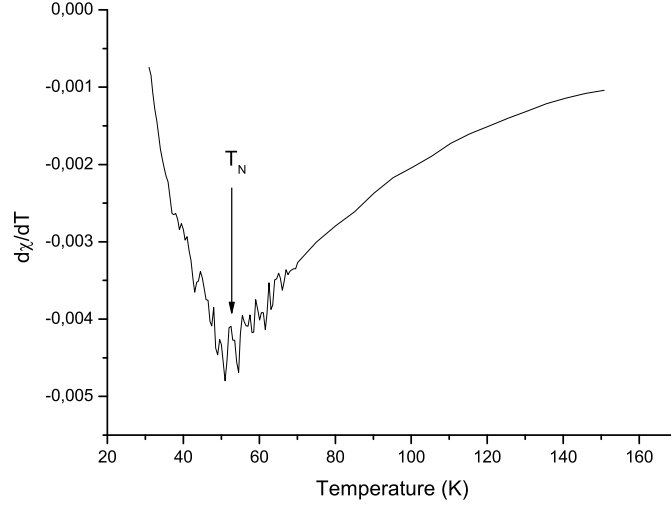

Figure 5.9: *dχ/dT versus temperature for an applied field of 0.01 Tesla. The arrow indicates the Néel temperature in agreement with the literature [23, 25, 27].*

In figure 5.7, we can observe that the decrease below χ_{max} disappears when applying a magnetic field of 6T. As the susceptibility is dominated by the Ho-contribution, this decrease should be associated with the magnetic behavior of the Ho-spins. There can be several reasons for this decrease: 1) the magnetic ordering of the Ho-sublattice; 2) the low-dimensional behavior of the Ho-sublattice or 3) a coupling of the Ho^{3+}-spins to the Ni^{2+}-Haldane system. We consider the first possibility unlikely because this would not lead to a suppression below 30K but already below T$_N$ $\simeq$53K [25]. The second option arises from the large moment for Ho for which a field of 6T represents a significant magnetic energy compared with the magnetic interactions. Nevertheless, we adopt the suggestion by Zheludev *et al.* [28]. They argue that there exists significant coupling of local crystal field excitations of the rare-earth ions to the Haldane-gap excitations of the Ni-sublattice. In such case the low-temperature behavior of the susceptibility may be determined by excitations of the Ho-sublattice, being coupled to the Ni-sublattice system, which exhibits excitations across the Haldane gap Δ. Modelling the magnetic susceptibility by a temperature independent term and a Haldane-gap term $\frac{exp(-\Delta/T)}{\sqrt{T}}$ [29], we extract from our magnetic susceptibility data below 15K a value of Δ $\simeq$42K which is significantly lower than the value reported for Nd$_2$BaNiO$_5$ (Δ=127K) [21] or for Y$_2$BaNiO$_5$ (Δ=100K) [15]
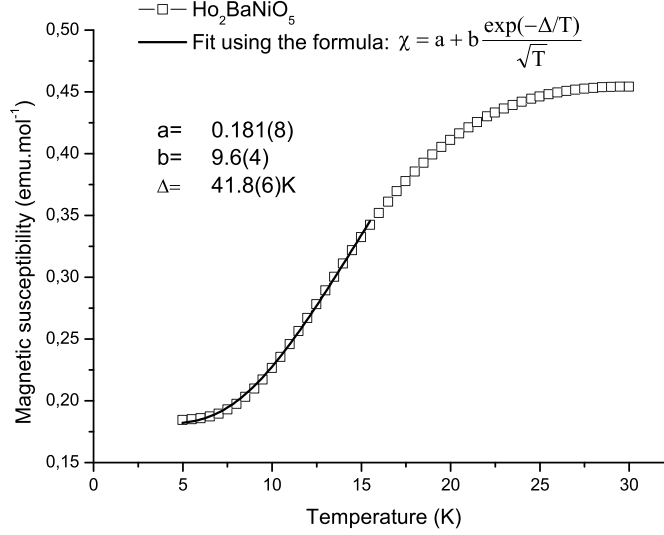
(see figure 5.10).

Figure 5.10: *Estimation of the Haldane gap in Ho_2BaNiO_5 by modelling the low temperature data with $\chi = a + b\frac{exp(-\Delta/T)}{\sqrt{T}}$. We use the temperature range 5-15K.*

The dependence of the Néel temperature of this family as function of temperature of the ionic radius suggests the influence of the volume, as well as the value of gJ, in the magnetic order [23]. For a Haldane system, a value of the gap Δ is function of J. The value of the gap for Ho_2BaNiO_5 is reduced by a factor 2 compared to other known R_2BaNiO_5. Such reduction of the gap could be due to different reasons:
- a significant difference in the Ni-Ni distances for Ho_2BaNiO_5 compared to the other rare-earth.
- an interchain coupling much larger in Ho_2BaNiO_5 which would renormalize the value of the gap.
The first possibility is unlikely due to the fact that the Ni-Ni distance (cell parameter a=d(Ni-Ni)) varies only by few percents over the different ionic radius (see figure 5.11).

If we assume that J does not change much between different members of the R_2BaNiO_5 family, which is true at least for Tb, Dy, Ho, Er and Tm [23], the value of the Haldane gap Δ should vary in an opposite fashion to the Néel temperature. We see in figure 5.11 that the Néel temperature increases linearly between Yb and Dy. Thus we believe that the reason for a reduced Haldane gap in Ho_2BaNiO_5 is likely due to a renormalization originating from the onset of a long range magnetic ordering.

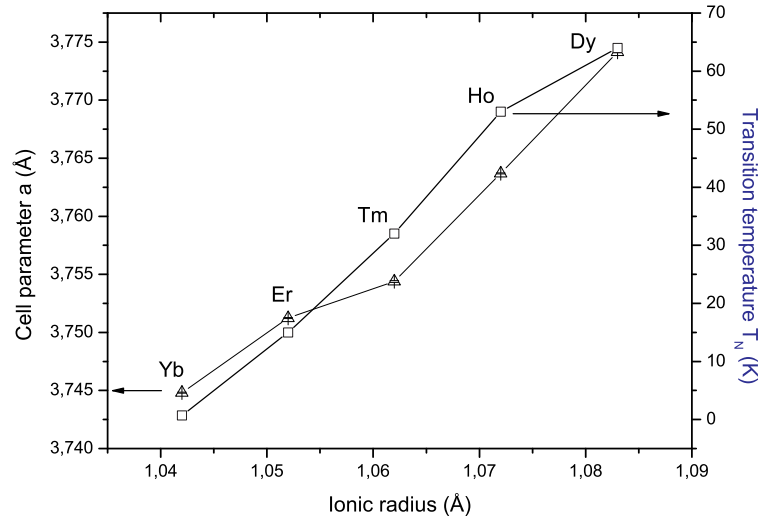We believe that for $T \ll \Delta$, the magnetic susceptibility exhibits Haldane

Figure 5.11: *The Néel temperature and the* a *cell parameter of some R$_2$BaNiO$_5$ from [23]*

behavior (see figure 5.10) originating from the Ho-spins, being coupled by exchange to the Ni-sublattice. Thus the disappearance of the decrease in χ below χ_{max} can be associated with the closure of the Haldane gap by a magnetic field, or with a change in the coupling of the Ho-spins to the Ni-spins. We do not know the influence of the external magnetic field on the staggered exchange field acting on the Ni chains due to the Ho sublattice magnetization. In zero field, the staggered exchange field is about 35T [30]. Therefore, we believe that an external magnetic field of 6T≪35T does not close the Haldane gap.

5.2.5 Magnetoelectricity

Now that we have investigated the magnetic properties of Ho$_2$BaNiO$_5$, we will show that we could induce a finite polarization in a magnetic field. The polarization was measured in a magnetic field. For each measurement, we cooled down the sample to 5K starting from 90K (T≫T$_N$). During the cooling process, we applied the magnetic field perpendicular to the electric field (magnetoelectric annealing). We used two different electric fields: 3.15kV/cm (175V) and 4.5kV/cm (250V). At 5K, we removed the electric field and kept the magnetic field. The induced polarization was measured upon heating by integrating the pyroelectric current. The electric field was generated using a Keithley 237 high voltage source measure unit. The pyroelectric current was measured using a Keithley 617 programmable electrometer. We show in figure 5.12 the sample holder that we used. The sample used was a sintered pellet polished down to 0.55 mm thickness with
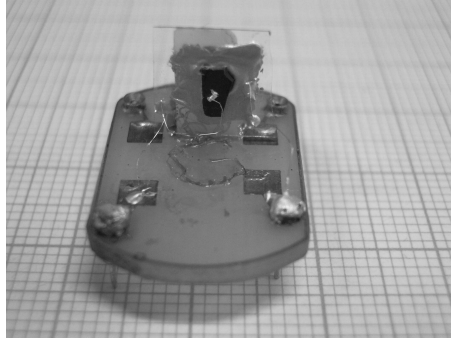
$0.5mm^2$ contact area.

Figure 5.12: *Picture of the Ho_2BaNiO_5 sample used for the determination of the induced polarization by magnetic field.*

First, we measure our sample applying an electric field of 3.15kV/cm (175V). We show the induced polarization in figure 5.13 under the application of a 1T magnetic field. We observe that the induced polarization has a broad maximum around 30K. Above T≈30K, the polarization decreases almost linearly and becomes zero near 70-75K. The linear magnetoelectric effect is observable only in the magnetically ordered phase. Thus, it is surprising that the polarization disappears near 70-75K while T_N is about 55K. Thus, we measure the induced polarization under H=1T for a higher electric field. We show for comparison in the same figure, the induced polarization under 1T magnetic field when applying a 4.5kV/cm (250V) electric field. The temperature behavior is similar for both electric fields. However, the polarization for a 4.5kV/cm electric field becomes zero at a lower temperature around 60K. Moreover, we notice a significant higher value of the induced polarization for the 4.5kV/cm electric field. Thus we believe that the apparent transition temperature to the paramagnetic paraelectric phase is related to the electric domains structure of our polycrystalline sample. One possible reason could be the presence of strong low dimensional interactions below T_N. This is known to occur in Nd_2BaNiO_5 [28]. The magnetic interactions could couple to the polarization and thus being affected by the strength of the electric field. Therefore the onset of the polarization does not coincide exactly with T_N.

Attempts of measurement with higher electric fields than 4.5kV/cm were not possible due to the closeness to the electrical breakdown of the sample. Consequently in the remaining part of our investigation, we made a magnetic field dependence study using a 4.5kV/cm electric field. We present in figure 5.14 the magnetic field dependence of the induced polarization.

There are common features of the induced polarization independently of the applied magnetic field. These common features are a linear dependence of the induced polarization close to T_N and a broad maximum around 30K.
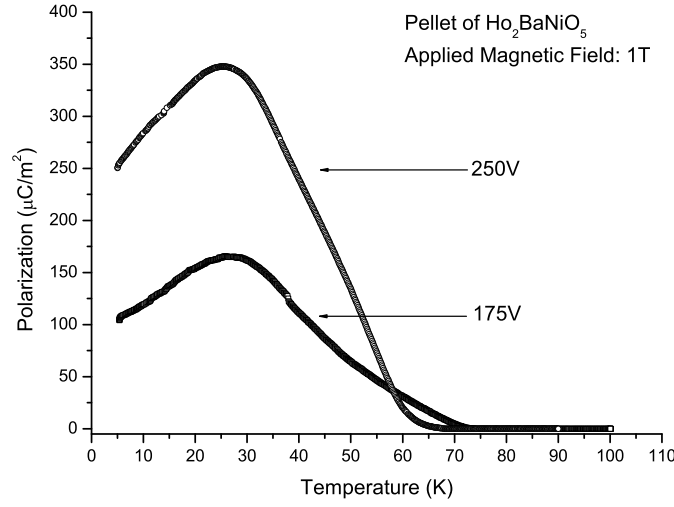
Figure 5.13: *Influence of the applied voltage on the induced polarization with H=1T*

In first approximation, we know that the induced polarization close to T$_N$ is proportional to the magnetic order parameter [31]. From neutron diffraction [25], we know that the Ho magnetic moment below T$_N$ and over a quite large range of temperature has a quasi linear temperature dependence. The Ni moments saturate very quickly below T$_N$. Thus, we ascribe the linear temperature dependence of the polarization below T$_N$ as a result of the magnetic order parameter. In this temperature range, this magnetic order parameter is mostly governed by the Ho magnetic moment and thus we are not sensitive to the Haldane gap to which the Ni moments contribute. Another common feature is the broad maximum around 30K which is almost magnetic field independent. This broad maximum is also present in the magnetic susceptibility (see figure 5.7) as a result of the one dimensional character of the magnetic order. Thus, we observe that the temperature dependence of the polarization reflects the 1D character of the magnetic order. Applying a magnetic field, we observe a decrease of the induced polarization from 1 to 5T. At H=6T, we observe a jump in the induced polarization. This jump in the polarization cannot be related to the eventual closing of the Haldane gap as discussed earlier. We know from susceptibility data that at H$_{C2}$, we have a new magnetic phase. Thus, in the hypothesis of a higher magnetization, one can expect a higher induced polarization. If the gap is closed thus the total magnetic moment of the system would increase and thus the induced polarization would be increased too. However the decrease from 1 to 5T followed by the increase at 6T of the polarization remains to be explained in its details. However the observation of a finite
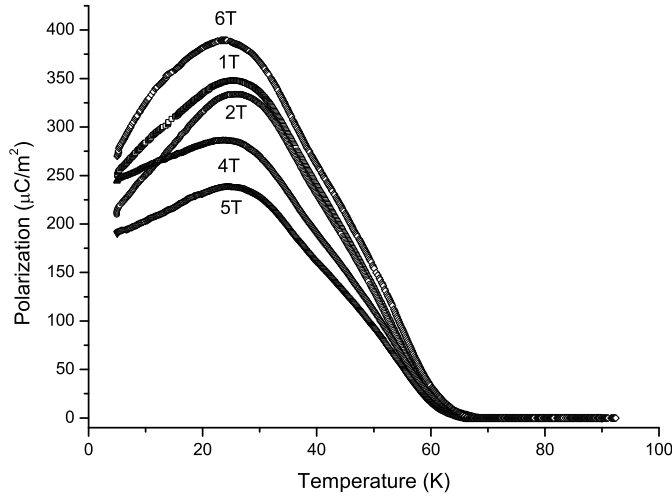
Figure 5.14: *Magnetic field dependence of the induced polarization measured on a pellet of Ho_2BaNiO_5 using a 4.5kV/cm electric field.*

polarization at any magnetic fields give us the indication that the three magnetic phases observed in figure 5.6 are magnetoelectric and thus magnetically ordered. This is surprising since the second metamagnetic phase transition at H_{C2} would typically gives rise to a paramagnetic phase for a simple 1D-Heisenberg system. Additional measurements and neutron diffraction under magnetic field could clarify the magnetic field dependence of the structural and magnetic properties.

5.2.6 Conclusion

Using symmetry arguments, we predict a linear magnetoelectric effect in Ho_2BaNiO_5. We investigate the magnetic and magnetoelectric properties of this Haldane gap system. We confirm the existence of two metamagnetic phase transitions at H_{C1}=2.9T and at H_{C2}=5.2T. We show that this system presents a linear magnetoelectric effect which exhibits the 1D character of its magnetic order. In addition, we demonstrate the unusual magnetic behavior of this Heisenberg system trough its magnetoelectric response. Further investigations are necessary to interpret the relationships between magnetic and structural properties.

References

[1] E. M. Bauer, C. Bellitto, M. Colapietro, G. Portalone, and G. Righini, Inorg. Chem. **42**, 6345 (2003)

[2] D. Y. Curtin, I. C. Paul, Chem. Rev. **81**, 525 (1981)

[3] T. Katsufuji, S. Mori, M. Masaki, Y. Moritomo, N. Yamamoto, and H. Takagi Phys. Rev. B, 64, 104419 (2001)

[4] T. Katsufuji and H. Takagi, Phys. Rev. B **64**, 54415 (2001)

[5] T. Katsufuji and H. Takagi, Phys. Rev. B **69**, 54415 (2004)

[6] M. Gich, C. Frontera, A. Roig, J. Fontcuberta, E. Molins, N. Bellido, C. Simon and C. Fleta, Nanotechnology **17**, 687 (2006)

[7] T. Kimura, S. Kawamoto, I. Yamada, M. Azuma, M. Takano, and Y. Tokura Phys. Rev B 67, 180401 (2003)

[8] N. Bellido, G. Nénert, T. T. M. Palstra, C. Simon, unpublished

[9] The Landau Theory of Phase Transitions, J.-C. Tolédano and P. Tolédano; World Scientific Publishing 1987

[10] J. H. van Vleck, The theory of electric and magnetic susceptibilities, Oxford University Press, (1932)

[11] Q. Jiang and S. J. Gong, Eur. Phys. J. B **43**, 333 (2005); C. Zhong, J. H. Fang and Q. Jiang, J. Phys.: Condens. Matter **16** 9059 (2004)

[12] F. D. M. Haldane, Phys. Lett. **93**A, 464 (1983)

[13] L. P. Regnault, I. Zaliznyak, J. P. Renard, and C. Vettier, Phys. Rev. B **50**, 9174 (1994)

[14] J. P. Renard *et al.*, Eur. Lett. **3**, 945 (1987); J. P. Renard *et al.*, J. Appl. Phys. **63**, 3538 (1988); K. Hirota *et al.*, Physica B **213**, 173 (1995); J. P. Renard *et al.* J. Phys. Colloq. **49**, C8 (1988); and A. Zheludev *et al.*, Phys. Rev. B **53**, 15 004 (1996)

[15] J. Darriet and L. P. Regnault, Solid State Commun. **86**, 409 (1993)

[16] J. F. DiTusa *et al.*, Physica B **194-196**, 181 (1994); J. F. DiTusa *et al.*, Phys. Rev. Lett. **73**, 1857 (1994)

[17] S. T. Schiffler, H. K. Müller-Buschbaum, Z. Anorg. Allog. Chem. **540-541**, 243 (1986)

[18] J. Amador, E. Gutierrez-Puebla, M. A. Monge, I. Rasines, J. A. Campá, C. Ruiz-Valero, J. M. Gomez de Salazar, Solid States Ionics, **32-33**, 123 (1989)

[19] A. Salinas-Sánchez, R. Sáez-Puche, J. Rodríguez-Carvajal, J. L. Martínez, Solid State Commnun. **78**, 481 (1991)

[20] R. Sáez-Puche, S. R. Herrera Apéstigue, Ann. Chim. Sci. Mat. 1998, **23**, 415

[21] A. Zheludev, J. M. Tranquada, T. Vogt and D. J. Buttrey, Phys. Rev. B **54**, 7437 (1996) and references therein

[22] A. C. Larson and R. B. Von Dreele, Los Alamos National Laboratory Report No. LAUR 86-748, 1994.

[23] E. García-Matres, J. L. Martínez and J. Rodríguez-Carvajal, Eur. Phys. J. B **24**, 59 (2001)

[24] H. T. Stokes and D. M. Hatch, (2002). ISOTROPY, stokes.byu.edu/isotropy.html

[25] E. García-Matres, J. Rodríguez-Carvajal and J. L. Martínez, Solid State Commun. **7**, 553 (1993)

[26] S. Okubo, H. Ohta, T. Tanaka, T. Yokoo and J. Akimitsu, Physica B **284-288** (2000) 1475

[27] E. García-Matres, J. L. García-Muñoz, J. L. Martínez and J. Rodríguez-Carvajal, J. Magnetism and Magnetic Materials **149** (1995) 363

[28] A. Zheludev *et al.*, Phys. Rev. B **61**, 11601 (2000)

[29] D. Poilblanc *et al.*, Phys. Rev. B **50**, 6511 (1994); Troger *et al.*, Phys. Rev. B **50**, 13515 (1994)

[30] A. Zheludev, E. Ressouche, S. Maslov, T. Yokoo, S. Raymond adn J. Akimitsu, Phys. Rev. Lett. **80**, 3630 (1998)

[31] P. Tolédano, Ferroelectrics **161**, 257 (1994)

Chapter 6

Predictions for new magnetoelectrics/multiferroics

6.1 Introduction

In the recent years, there has been a renewed interest in the coexistence and interplay of magnetism and electrical polarization [1, 2, 3]. This interest has been concentrated on multiferroics and magnetoelectric materials. In multiferroics, a spontaneous polarization coexists with a long range magnetic order. In magnetoelectrics (we consider here only the linear effect), the polarization is induced by a magnetic field in a magnetically ordered phase. In the Landau theory framework, multiferroics which are not magnetoelectric present at least a coupling of the type P^2M^2 (P: polarization, M: total magnetization) while linear magnetoelectrics are characterized by terms like PM^2 or LMP (L: antiferromagnetic order parameter) [4]. Terms like P^2M^2 are of higher degree than PM^2 or LMP terms. Consequently, we expect a stronger interplay between dielectric and magnetic properties in linear magnetoelectrics than in multiferroics. Other coupling terms can also characterize the magnetoelectric effect. They are discussed by Harris [5]. In the search for materials presenting a strong coupling of magnetism and polarization, the most promising ones are multiferroics materials presenting linear magnetoelectric properties. These materials are scarce. Thus, it is also of interest to look for new magnetoelectric materials by itself.

The recent efforts have been concentrated on two main ideas: magnetic frustration and breaking of the inversion center due to an antiferromagnetic ordering. These approaches have been generated by the ideas on one side of Katsura [6] and of Sergienko [7] and on the other side of Mostovoy [8]. They described in the case of non collinear magnets a possible mechanism for magnetoelectricity and polarization induced by antiferromagnetic ordering, respectively. The new mechanism proposed by Katsura *et al.* does not

involve the Dzialoshinskii-Moriya (DM) interaction contrary to typical magnetoelectric compound such as Cr_2O_3 [9]. Most of the recent research on multiferroics concerns centrosymmetric oxides [11]. These materials present a breaking of the symmetry giving rise to a spontaneous polarization which may be reversible by application of a magnetic field. However, the investigation of possible polar structures induced by antiferromagnetic ordering is known since about 35 years [13]. The authors of ref. [13] proposed already $BiMn_2O_5$ as possible multiferroic which is nowadays one of the most studied families. The idea of using symmetry analysis to predict magnetoelectric compounds is not new. The first reported magnetoelectric compound Cr_2O_3 was predicted to be magnetoelectric prior to any experimental evidence [12]. Nevertheless, we use symmetry analysis in order to illustrate the usefulness of it by predicting several materials exhibiting possible multiferroic and magnetoelectric properties.

In addition, one can notice that the magnetic point groups do not give information regarding magnetic frustration. The magnetic frustration is strongly correlated to the crystal structure. This is an important and obvious point, however often overlooked. The inversion center breaking due to antiferromagnetic ordering is intrinsic to the symmetry properties of the spins. Thus, the fact that the structure remains centrosymmetric in the magnetically ordered phase is also strongly related to the crystal structure. This will be illustrated in section 6.4.

In the present chapter, we present a symmetry analysis of selected materials. All these materials should present magnetoelectricity based on symmetry arguments. We made a literature survey considering various magnetically ordered compounds for which neutron data were available. We made a systematic symmetry analysis of all the studied compounds (about 50 materials). We present here only a selection of this list.

6.2   Study of selected fluorides

We present in this part our investigation of selected fluorides. We chose this family as an illustration for magnetic frustration as an important component for magnetoelectricity. Moreover, we cannot have polarization in conducting materials. Thus, the high charge transfer in these materials make them good candidates for experimental investigations. Several fluorides were reported to crystallize in a polar structure. Consequently, in addition to magnetoelectric properties, several fluorides are potentially ferroelectric. Experimental examples of magnetic frustration [14] are still rather scarce [15]. Among them, the most common case is provided by the triangular plane lattice with antiferromagnetic interactions, which has been extensively studied, from a theoretical point of view. This geometry leads to three antiferromagnetic

sublattices oriented at 120° to each other. Among these materials, several fluorides have shown to exhibit magnetic frustration. We focus here on several of them. They have been the subject of detailed crystallographic and magnetic studies by means of neutron diffraction. Depending on their structure, they present a high or low degree of magnetic frustration. Several of these fluorides are possibly magnetoelectric multiferroic materials based on symmetry analysis.

6.2.1 Study of α-KCrF$_4$

α-KCrF$_4$ is the first in the selected fluorides we are going to present on magnetically frustrated fluorides with possible magnetoelectric properties. The crystal structure of α-KCrF$_4$ is orthorhombic (space group Pnma (n°62), a = 15.76 Å, b= 7.43 Å, c = 18.38 Å). It consists of infinite columns of CrO$_6$ octahedra sharing edges along the b axis (see figure 6.1) [16].
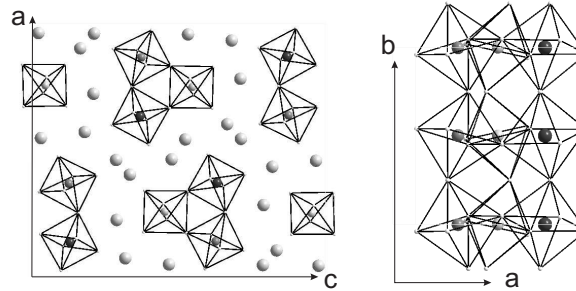

Figure 6.1: *Crystal structure of KCrF$_4$ projected along* b *(left) and* c *axis (right). We show the* Cr^{3+} *sites in their octahedral environment. The white atoms are the* K$^+$ *atoms. The different grey scales represent the three inequivalent* Cr^{3+} *sites.*

This compound is the most frustrated of the fluorides. It orders antiferromagnetically only under T$_N$ = 4 K with a quasi 1D behavior. We present in figure 6.2 a representation of the magnetic structure as determined from neutron scattering [17].

There are three inequivalent Cr^{3+} ions per unit cell and occupying the Wyckoff position 8d. Consequently, we have eight different magnetic sites all carrying one spin S$_j$. We can define the following eight magnetic vectors (one ferromagnetic and seven antiferromagnetic ones):
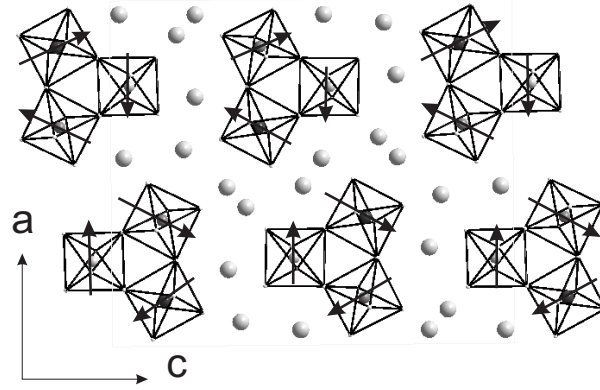
Figure 6.2: *Magnetic structure of KCrF$_4$ in the (a,c) plane. Arrows indicate the magnetic moments on the chromium atoms with a quasi-120° configuration.*

$$\vec{M} = \vec{S_1} + \vec{S_2} + \vec{S_3} + \vec{S_4} + \vec{S_5} + \vec{S_6} + \vec{S_7} + \vec{S_8}$$
$$\vec{L_1} = \vec{S_1} - \vec{S_2} + \vec{S_3} - \vec{S_4} + \vec{S_5} - \vec{S_6} + \vec{S_7} - \vec{S_8}$$
$$\vec{L_2} = \vec{S_1} + \vec{S_2} - \vec{S_3} - \vec{S_4} + \vec{S_5} + \vec{S_6} - \vec{S_7} - \vec{S_8}$$
$$\vec{L_3} = \vec{S_1} - \vec{S_2} - \vec{S_3} + \vec{S_4} + \vec{S_5} - \vec{S_6} - \vec{S_7} + \vec{S_8}$$
$$\vec{L_4} = \vec{S_1} + \vec{S_2} + \vec{S_3} + \vec{S_4} - \vec{S_5} - \vec{S_6} - \vec{S_7} - \vec{S_8} \qquad (6.1)$$
$$\vec{L_5} = \vec{S_1} - \vec{S_2} + \vec{S_3} - \vec{S_4} - \vec{S_5} + \vec{S_6} - \vec{S_7} + \vec{S_8}$$
$$\vec{L_6} = \vec{S_1} + \vec{S_2} - \vec{S_3} - \vec{S_4} - \vec{S_5} - \vec{S_6} + \vec{S_7} + \vec{S_8}$$
$$\vec{L_7} = \vec{S_1} - \vec{S_2} - \vec{S_3} + \vec{S_4} - \vec{S_5} + \vec{S_6} + \vec{S_7} - \vec{S_8}$$

Lacorre and collaborators have investigated also the transformation properties of the different components of the magnetic vectors. We reproduce in table 6.1 the results of their derivations [17].

Let's have a look at the possible LMP terms allowed by symmetry. These terms are the signature of the linear magnetoelectric effect. For this, we need to know what are the transformation properties of the polarization components. Here once more, it is sufficient to look at the effect of the generators of the space group. In table 6.2, we present the transformation properties of the polarization components.

According to the tables 6.1 and 6.2, we can determine the allowed LMP terms which may be present and giving rise to an induced polarization under magnetic field. We know that below T$_N$, the magnetic structure is

IR	Magnetic components
Γ_1	L_{1x}, L_{2y}, L_{3z}
Γ_2	M_x, L_{3y}, L_{2z}
Γ_3	L_{2x}, L_{1y}, M_z
Γ_4	L_{3x}, M_y, L_{1z}
Γ_5	L_{5x}, L_{6y}, L_{7z}
Γ_6	L_{4x}, L_{7y}, L_{6z}
Γ_7	L_{6x}, L_{5y}, L_{4z}
Γ_8	L_{7x}, L_{4y}, L_{5z}

Table 6.1: *Magnetic components classified by IR.*

	2_{1x}	2_{1z}	$\bar{1}$
P_x	1	-1	-1
P_y	-1	-1	-1
P_z	-1	1	-1

Table 6.2: *Transformation properties of the polarization components for the space group Pnma1' associated to $k = 0$.*

described by the IR Γ_6. It is experimentally observed that $L_{4x} \text{¿} L_{6z}$ and $L_{7z} \simeq 0$ [17]. Taking into account these experimental results, we find that the most relevant magnetoelectric terms are $L_{4x}P_yM_z$ and $L_{4x}P_zM_y$. Consequently, an induced polarization may appear along P_y (P_z) if one applies a magnetic field along z (y). Since this compound is centrosymmetric, it does not present a multiferroic character. The quasi-120° configuration allows a DM interaction which may be responsible for magnetoelectricity.

6.2.2 Study of KMnFeF$_6$

The fluoride KMnFeF$_6$ presents a partial ordering of the Mn and Fe atoms giving rise to an enlargement of the unit cell compared to the usual tetragonal tungsten bronze type [18]. The family of tetragonal tungsten bronze and related ones have been extensively investigated due to their ferroelectric properties [19]. This compound crystallizes in the space group Pba2 (n°32), where the Mn and Fe ions order on the 8c Wyckoff position of the structure and occupy statistically the 4b Wyckoff position. This compound is magnetically frustrated due to the presence of triangular cycles of antiferromagnetic interactions. All the Mn and Fe cations have an octahedral environment of fluorine atoms. In the *ab* plane, Mn and Fe ions alternate along the *c* axis. The magnetic structure is presented in figure 6.3 [18]. Although the ferroelectricity transition has not been investigated to our knowledge, this compound should present a multiferroic character below
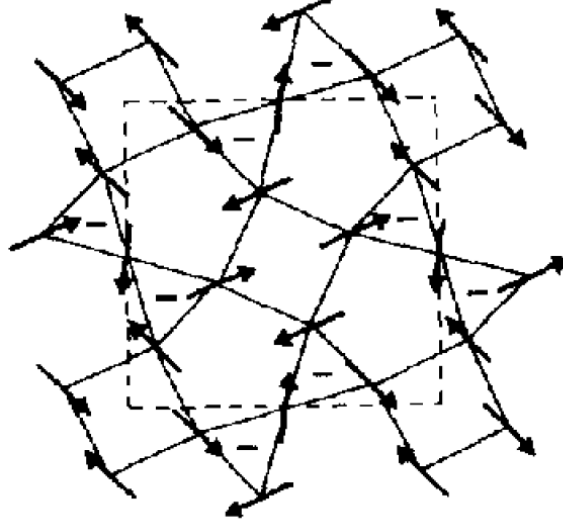
T_C.

Figure 6.3: *Magnetic structure of KMnFeF$_6$ in the (a,b) plane. Arrows indicate the magnetic moments on the iron atoms (mostly along the a axis) from [18].*

Although presenting magnetic frustration, the compound KMnFeF$_6$ orders ferrimagnetically below $T_C = 148$ K with a ratio $\frac{\Theta}{T_C}$=3. The magnetic structure is identical to the chemical unit cell and thus $\overrightarrow{k} = \overrightarrow{0}$. The symmetry analysis by Bertaut's method gives rise to the results presented in table 6.5 [18, 20].

Modes	x	y	z	Magnetic space groups
Γ_1	G_x	A_y	C_z	Pba2
Γ_2	C_x	F_y	G_z	Pba'2'
Γ_3	A_x	G_y	F_y	Pb'a'2
Γ_4	F_x	C_y	A_y	Pb'a2'

Table 6.3: *Irreducible representations for the space group P$ba21$' associated to **k**=0.*

The neutron data show that the best model for the magnetic structure is given by the Γ_4 mode. The corresponding magnetic space group is thus Pb'a2' which has the magnetic point group m'm2'. According to table 2.4, we have a linear magnetoelectric effect which is allowed having the following allowed terms (after transformation of the coordinates system):

$$[\alpha_{\mathbf{ij}}] = \begin{pmatrix} 0 & 0 & 0 \\ 0 & 0 & \alpha_{23} \\ 0 & \alpha_{32} & 0 \end{pmatrix}$$

We remind that $KMnFeF_6$ presents a polar structure and is likely to be ferroelectric. Consequently, $KMnFeF_6$ is a multiferroic material which presents a strong interplay between magnetism and polarization below $T_C=148K$. Moreover, we notice here that it would be one of the scarce ferrimagnetic compounds presenting such properties. Under the application of a magnetic field below T_C along the c axis (direction of spontaneous polarization) should create a polarization along the b axis (term α_{23}) and vice versa (term α_{32}).

6.2.3 Study of 2 members of the $Ba_6M_nF_{12+2n}$ family

In the previous fluorides, the magnetic frustration appeared in corner-sharing octahedra, which leads to a single type of interaction. P. Lacorre and coworkers have been also investigating compounds like $Ba_2Ni_3F_{10}$ (n = 9) and $Ba_2Ni_7F_{18}$ (n = 21) which are members of the $Ba_6M_nF_{12+2n}$ family [21, 22]. In this family where M=Ni, there are not only corner-sharing octahedra but also edge-sharing octahedra. Both types of interaction exist in the $Ba_2Ni_3F_{10}$ and $Ba_2Ni_7F_{18}$ compounds. These compounds have been investigated by means of powder neutron diffraction at room and low temperatures.

Let's have a look first at the $Ba_2Ni_3F_{10}$ material. This compound crystallizes in the space group $C2/m$ (n°12) containing 3 different Ni^{2+} per unit cell. 2 Ni ions occupy the Wyckoff position 4i and the other one occupies the Wyckoff position 4h. Below $T_N = 50$ K, an antiferromagnetic ordering starts to develop characterized by a magnetic wave-vector $\overrightarrow{k}=(0,0,1/2)$. All the (hkl) magnetic reflections do not satisfy the C-centering of the chemical cell but a primitive lattice. P. Lacorre and collaborators have shown that the magnetic space group is $P2/m'$ where the magnetic moments lie in the ac plane. Consequently, the magnetic point group of this compound below its T_N is 2/m'. According to table 2.4, a linear magnetoelectric effect is allowed having the following expression:

$$[\alpha_{\mathbf{ij}}] = \begin{pmatrix} \alpha_{11} & 0 & \alpha_{13} \\ 0 & \alpha_{22} & 0 \\ \alpha_{31} & 0 & \alpha_{33} \end{pmatrix}$$

Consequently, induced polarization can be observed along the three crystallographic directions under the application of an applied magnetic field. This material is not multiferroic since its structure is centrosymmetric. Moreover the structure remains centrosymmetric in the magnetic ordered phase. Consequently no spontaneous polarization can develop below and above T_N.

The other member of the family of interest is for n=21. $Ba_2Ni_7F_{18}$ crystallizes in the polar space group P1 (n°1) containing four inequivalent

sets of Ni^{2+} ions. Each Ni^{2+} ion occupies the Wyckoff position 1a in the general position. From all the fluorides that we treat here, it is the second which orders ferrimagnetically under $T_C = 36$ K. Due to the low symmetry of the crystal, we have to deal here with magnetic components along the three crystallographic directions. While all the already studied fluorides present magnetic frustrations, it is not the case in this compound. We mean there is no competition between next nearest neighbors. However, we have a non collinear magnet most probably due to the allowed DM interaction. All the new magnetic reflections can be indexed in the same cell as the chemical one. Consequently, the star of the magnetic wave-vector has only one arm. Thus, we have the following IR:

	h_1
Γ_1	1

Table 6.4: *Irreducible representation for the space group* P11' *associated to* **k**=(0, 0, 0).

According to the table 6.4, there is only one possibility for the magnetic space group which is P1. Following the table 2.4, a linear magnetoelectric effect is allowed with non-zero components:

$$[\alpha_{\mathbf{ij}}] = \begin{pmatrix} \alpha_{11} & \alpha_{12} & \alpha_{13} \\ \alpha_{21} & \alpha_{22} & \alpha_{23} \\ \alpha_{31} & \alpha_{32} & \alpha_{33} \end{pmatrix}$$

Consequently, $Ba_2Ni_7F_{18}$ is a potential multiferroic material (polar structure and ferrimagnetic below T_C=36K). Moreover, irrespective of the direction of an applied magnetic field, the polarization parallel to the magnetic field will increase due to the magnetoelectric effect below T_C.

6.2.4   Study of CsCoF$_4$

CsCoF$_4$ is the last compound among the fluorides that we investigate in the light of a possible magnetoelectric effect. This compound crystallizes in the non-polar space group I-4c2 (n°120) with two different Co^{3+} Wyckoff positions in the unit cell: 4d and 16i. The antiferromagnetic order occurring below $T_N = 54$ K is characterized by a magnetic wave-vector $\overrightarrow{k} = \overrightarrow{0}$ [23]. This structure is also magnetically frustrated due the presence of ferromagnetic interactions within an antiferromagnetic plane as described in figure 6.4.

Based on geometrical considerations and comparison with magnetic structure of compounds of the same family (namely LiCoF$_4$), the authors proposed some constraints on the orientation of the magnetic moments. From
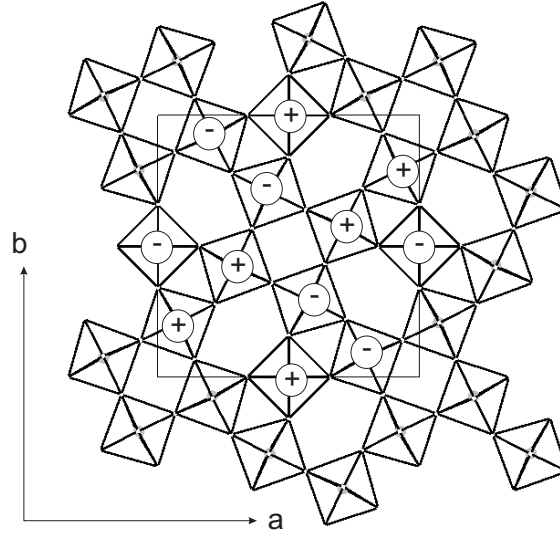
Figure 6.4: *Magnetic structure of CsCoF$_4$ in the (a,b) plane. Plus and Minus signs indicate the magnetic moments along the c axis (up or down).*

these considerations, they found that the magnetic space group of CsCoF$_4$ is I-4'. The corresponding magnetic point group is -4'. If one compares this magnetic point group with the ones listed in table 2.4, we observe that a linear magnetoelectric effect is possible along several directions:

$$[\alpha_{\mathbf{ij}}] = \left(\begin{array}{ccc} \alpha_{11} & \alpha_{12} & 0 \\ -\alpha_{12} & \alpha_{11} & 0 \\ 0 & 0 & \alpha_{33} \end{array} \right)$$

Here a probable DM is responsible for the magnetoelectric effect although it has not been reported experimentally. This is probably due to the too low deviation from collinearity along the c axis.

In conclusion, we have shown from symmetry analysis that several fluorides may present a multiferroic character coupled to an induced polarization under the application of a magnetic field. Most of them present magnetic frustration. We present here possible magnetoelectrics which are among the scarce ferrimagnetic systems. This ferromagnetism may enhance the interplay between polarization and magnetism for the case of multiferroic materials. While the mechanism for potential ferroelectricity remains to be investigated, the associated magnetoelectric effect is presumably due to the DM interaction (including the non multiferroic cases).

6.3   Other materials of interest

6.3.1   Introduction

We present in this section, compounds already known as potential materials of technological importance. $LiFeP_2O_7$ is a material considered for Li battery while $Sr_2CoSi_2O_7$ is considered as a good candidate for lasers. We want to emphasize with these two examples the possibility for additional interesting properties (i.e. magnetoelectricity) in already known materials.

6.3.2 $LiFeP_2O_7$

Introduction

Compositions with general formula $LiMX_2O_7$ (M = Fe, V; X = P, As) have been widely investigated in the 90's but also nowadays for their interesting crystal chemistry and more recently for their potential application as electrode materials. The transition metal ion is surrounded by six oxygens forming an octahedron [27]. In $LiFeP_2O_7$, iron atoms are connected through super-super exchange paths involving diphosphate groups which may present interesting magnetic properties. $LiFeP_2O_7$ crystallizes in a polar structure described by the space group $P2_1$. It is a remarkable feature since most of the AMP_2O_7 family members crystallizes in the non-polar space group $P2_1/c$. Many of these materials experience a transition from $P2_1/c$ to $P2_1/c$ with an enlargement of the unit cell above RT. Thus, we can reasonably expect that $LiFeP_2O_7$ may undergo a phase transition towards a centrosymmetric structure. Depending on the IR involved in the transition we will have a proper or an improper ferroelectric. While the magnetic properties of the parent compound $NaFeP_2O_7$ have been widely studied, $LiFeP_2O_7$ has been the subject of few studies. Among these ones, G. Rousse and collaborators have been investigating the magnetic structure using neutron diffraction on a powder sample [27]. The magnetic structure is presented in figure 6.5.

Magnetic ordering

The compound $LiFeP_2O_7$ crystallizes in the space group $P2_1$ (n°4) where there is only one Fe^{3+} per asymmetric unit cell occupying the Wyckoff position 2a. Consequently, there are two Fe atoms per unit cell at (x, y, z) (carrying $\overrightarrow{S_1}$ moment) and (-x, y+1/2, -z) (carrying $\overrightarrow{S_2}$ moment).

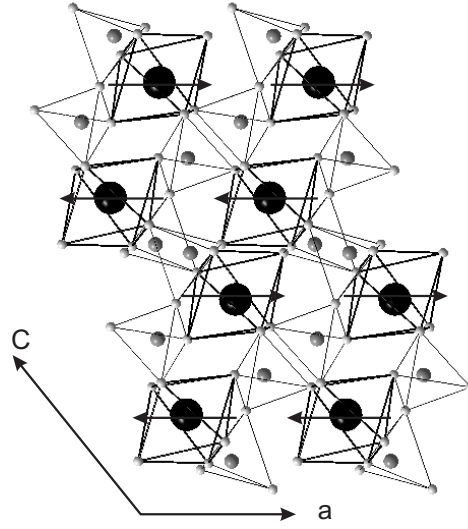Consequently, we can define 2 magnetic vectors:

Figure 6.5: *Crystal and magnetic structures of LiFeP$_2$O$_7$ in the (a,c) plane. Arrows indicate the magnetic moments on the iron atoms (mostly along the a axis). The iron atoms are represented in black within oxygen octahedra. The dimers with corner shared oxygen contain the phosphorus atoms.*

$$\overrightarrow{M} = \overrightarrow{S_1} + \overrightarrow{S_2} \tag{6.2}$$

$$\overrightarrow{L} = \overrightarrow{S_1} - \overrightarrow{S_2} \tag{6.3}$$

The space group P2$_1$ contains only two symmetry elements: the identity 1 and a 2 fold screw axis 2$_1$ that we will denote h$_1$ and h$_2$, respectively. The expressions of these two symmetry elements are:

$$\mathbf{h_1} = \begin{pmatrix} 1 & 0 & 0 & 0 \\ 0 & 1 & 0 & 0 \\ 0 & 0 & 1 & 0 \\ 0 & 0 & 0 & 1 \end{pmatrix} \mathbf{h_2} = \begin{pmatrix} -1 & 0 & 0 & 0 \\ 0 & 1 & 0 & 1/2 \\ 0 & 0 & -1 & 0 \\ 0 & 0 & 0 & 1 \end{pmatrix}$$

The magnetic order appearing under T$_N$ = 22K is described by $\overrightarrow{k}$ = 0. Consequently, the irreducible representations associated with this wave-vector are the same as the ones of point group 2 (see table 6.5).

In order to know which components of the different magnetic vectors belong to which IR, we need to look at the effect of the symmetry elements on the position of the atoms.

	h_1	h_2	Rh_1	Rh_2
Γ_1	1	1	-1	-1
Γ_2	1	-1	-1	1

Table 6.5: *Irreducible representations for the space group $P2_1 1'$ associated to* ***k***=0.

$$h_2 = \begin{pmatrix} -1 & 0 & 0 & 0 \\ 0 & 1 & 0 & 1/2 \\ 0 & 0 & -1 & 0 \\ 0 & 0 & 0 & 1 \end{pmatrix} \times \begin{pmatrix} x \\ y \\ z \\ 1 \end{pmatrix} = \begin{pmatrix} -x \\ y+1/2 \\ -z \\ 1 \end{pmatrix}$$

From the example described above, we can find all the transformations properties of the atoms. These results are presented in table 6.6. Using tables 6.5 and 6.6, we can determine to which IR belong each magnetic compounds. We present the results in table 6.7.

	h_1	h_2
(x, y, z)	(x, y, z)	(-x, y+1/2, -z)
(-x, y+1/2, -z)	(-x, y+1/2, -z)	(x, y, z)

Table 6.6: *Transformation properties of the symmetry elements on the Wyckoff positions 2a in the space group $P2_1$.*

The results of table 6.7 allow us to construct the Landau free-energy, separating the exchange and magnetic anisotropy energies. Due to the magnitude of the two contributions, we write the exchange terms up to the fourth degree and the relativistic terms up to the second degree (see equation 6.4.

Γ_1	L_x, L_z, M_y
Γ_2	L_y, M_x, M_z

Table 6.7: *Components of the **M** and **L** vectors which form a basis for the IR of $P2_1 1'$ at **k**=0.*

$$\begin{aligned} F = F_0 &+ \frac{a}{2}L^2 + \frac{b}{4}L^4 + \frac{c}{2}M^2 + \frac{d}{4}M^4 \\ &+ \frac{1}{2}\sum_{i=x,y,z}(\nu_i L_i^2 + \beta_i M_i^2) \\ &+ \delta L_x L_z + \gamma M_x M_z \\ &+ \sigma_1 L_x M_y + \sigma_2 L_z M_y + \sigma_3 L_y M_z + \sigma_5 L_y M_x \\ &+ \frac{\alpha}{2}P^2 + \beta L_x L_z P_y \end{aligned} \tag{6.4}$$

The first line in equation 6.4 represents the exchange energy. It is formed from the scalar products $\vec{L}^2 = \vec{L} \cdot \vec{L}$ and $\vec{M}^2 = \vec{M} \cdot \vec{M}$. The other lines correspond to the relativistic terms. We have separated in the magnetic anisotropy term the δ which couples different antiferromagnetic components L_i, from the σ_j terms which couple the total magnetization components M_i to the L_i. γ term couples the total magnetization components $M_x M_z$. The last line corresponds to the polar state of the structure. We are now able to discuss in a complete manner the type and nature of the magnetic order which arise below T_N.

- First approximation: we neglect the coupling terms involving the total magnetization. This approximation is justified by the fact that no ferromagnetic component has been observed experimentally. We can rewrite the free energy as:

$$F = F_0 + \frac{a}{2}L^2 + \frac{b}{4}L^4 + \frac{1}{2}\sum_{i=x,y,z}(\nu_i L_i^2) + \frac{\alpha}{2}P^2 + \beta L_x L_z P_y \qquad (6.5)$$

Minimization of F gives:

$$\frac{\partial F}{\partial L_x} = aL_x + bL_x^3 + \nu_x L_x + \beta L_z P_y = 0$$
$$\frac{\partial F}{\partial L_z} = aL_z + bL_z^3 + \nu_z L_z + \beta L_x P_y = 0 \qquad (6.6)$$
$$\frac{\partial F}{\partial P_y} = \alpha P_y + L_x L_z = 0$$

From the last line of equation 6.6, we find that $P_y = \frac{-1}{\alpha}L_x L_z$. Replacing P_y by its expression in L_x and L_z, we find the magnetic structure observed by G. Rousse $et\ al.$ [27]:

$$L_x^2 = \frac{\frac{ab}{\alpha} + ab + b\nu_x + \nu_z}{\frac{\beta^2}{\alpha^2} - b^2}$$
$$L_z^2 = \frac{\frac{ab}{\alpha} + ab + b\nu_z + \nu_x}{\frac{\beta^2}{\alpha^2} - b^2} \qquad (6.7)$$

Magnetoelectric properties

Now that we have described the magnetic ordering, we will have a look at the possible magnetoelectric properties. In order to determine LMP coupling terms allowed by symmetry, we derive table 6.8. Table 6.8 is

	h_1	h_2	Rh_1	Rh_2
L_x	1	1	-1	-1
L_y	1	-1	-1	1
L_z	1	1	-1	-1
M_x	1	-1	-1	1
M_y	1	1	-1	-1
M_z	1	-1	-1	1
P_x	1	-1	1	-1
P_y	1	1	1	1
P_z	1	-1	1	-1

Table 6.8: *Transformation properties of the components of the different vectors of interest for the space group $P2_1 1$' associated to $\boldsymbol{k}=0$.*

similar to the table 6.6 to which we added the transformation properties of the polarization.

From table 6.8, we notice that a certain number of terms of LMP type are allowed. Keeping in mind that the magnetic structure is described by magnetic components along x and z, the terms of interest are: $L_x M_x P_x$, $L_x M_y P_y$ and $L_z M_z P_z$. Consequently, we can write a new expression for the free energy including the magnetoelectric coupling terms given in eq. 6.8. We do not include term like P^4 since we are interested here in the magnetic ordered phase.

$$
\begin{aligned}
F = & F_0 + \frac{a}{2}L^2 + \frac{b}{4}L^4 \\
& + \lambda_1 L_x M_x P_x + \lambda_2 L_x M_y P_y + \lambda_3 L_z M_z P_z \\
& + \frac{M^2}{2\chi} + \frac{P^2}{2\kappa}
\end{aligned}
\tag{6.8}
$$

Bilinear terms like $L_i M_j$ are not considered because they cannot give rise to polarization. If we minimize equation 6.8, we find:

$$\frac{\partial F}{\partial L_x} = aL_x + bL_x^3 + \lambda_1 M_x P_x + \lambda_2 M_y P_y$$

$$\frac{\partial F}{\partial L_y} = aL_y + bL_y^3$$

$$\frac{\partial F}{\partial L_z} = aL_z + bL_z^3 + \lambda_1 M_z P_z$$

$$\frac{\partial F}{\partial M_x} = \lambda_1 L_x P_x + \frac{M_x}{\chi_{xx}}$$

$$\frac{\partial F}{\partial M_y} = \lambda_2 L_x P_y + \frac{M_y}{\chi_{yy}} \tag{6.9}$$

$$\frac{\partial F}{\partial M_z} = \lambda_3 L_z P_z + \frac{M_z}{\chi_{zz}}$$

$$\frac{\partial F}{\partial P_x} = \lambda_1 L_x M_x + \frac{P_x}{\kappa_{xx}}$$

$$\frac{\partial F}{\partial P_y} = \lambda_2 L_x M_y + \frac{P_y}{\kappa_{yy}}$$

$$\frac{\partial F}{\partial P_z} = \lambda_3 L_z M_z + \frac{P_z}{\kappa_{zz}}$$

From equation 6.9, we can find two series of equalities:

$$P_x = -\kappa_{xx}\lambda_1 L_x M_x$$
$$P_y = -\kappa_{yy}\lambda_2 L_x M_y \tag{6.10}$$
$$P_z = -\kappa_{zz}\lambda_3 L_z M_z$$

and

$$M_x = -\chi_{xx}\lambda_1 L_x P_x$$
$$M_y = -\chi_{yy}\lambda_2 L_x P_y \tag{6.11}$$
$$M_z = -\chi_{zz}\lambda_3 L_z P_z$$

Using eq. 6.11 to put in eq. 6.10, we find that there is no polarization possible irrespective of the magnetic order (paramagnetic or antiferromagnetic):

$$P_x(1 - \kappa_{xx}\chi_{xx}\lambda_1^2 L_x^2) = 0$$
$$P_y(1 - \kappa_{yy}\chi_{yy}\lambda_2^2 L_x^2 = 0 \tag{6.12}$$
$$P_z(1 - \kappa_{zz}\chi_{zz}\lambda_3^2 L_z^2) = 0$$

However, we shall see that equation 6.12 is true only in the absence of a magnetic field. Let's imagine that one applies a magnetic field H on cooling

trough T_N. In this case, we can take back the equation 6.8 to which we are going to add a $\vec{M}\cdot\vec{H}$ term. This is given in eq. 6.13.

$$
\begin{aligned}
F = & F_0 + \frac{a}{2}L^2 + \frac{b}{4}L^4 \\
& + \lambda_1 L_x M_x P_x + \lambda_2 L_x M_y P_y + \lambda_3 L_z M_z P_z \\
& + \frac{M^2}{2\chi} + \frac{P^2}{2\kappa} - M.H
\end{aligned}
\tag{6.13}
$$

This time, if we minimize 6.13, we find a different expression for the minima:

$$
\begin{aligned}
\frac{\partial F}{\partial L_x} &= aL_x + bL_x^3 + \lambda_1 M_x P_x + \lambda_2 M_y P_y \\
\frac{\partial F}{\partial L_y} &= aL_y + bL_y^3 \\
\frac{\partial F}{\partial L_z} &= aL_z + bL_z^3 + \lambda_1 M_z P_z \\
\frac{\partial F}{\partial M_x} &= \lambda_1 L_x P_x + \frac{M_x}{\chi_{xx}} - H_x \\
\frac{\partial F}{\partial M_y} &= \lambda_2 L_x P_y + \frac{M_y}{\chi_{yy}} - H_y \\
\frac{\partial F}{\partial M_z} &= \lambda_3 L_z P_z + \frac{M_z}{\chi_{zz}} - H_z \\
\frac{\partial F}{\partial P_x} &= \lambda_1 L_x M_x + \frac{P_x}{\kappa_{xx}} \\
\frac{\partial F}{\partial P_y} &= \lambda_2 L_x M_y + \frac{P_y}{\kappa_{yy}} \\
\frac{\partial F}{\partial P_z} &= \lambda_3 L_z M_z + \frac{P_z}{\kappa_{zz}}
\end{aligned}
\tag{6.14}
$$

From 6.13, we get new values for the total magnetization components while the polarization components are unchanged:

$$
\begin{aligned}
P_x &= -\kappa_{xx}\lambda_1 L_x M_x \\
P_y &= -\kappa_{yy}\lambda_2 L_x M_y \\
P_z &= -\kappa_{zz}\lambda_3 L_z M_z
\end{aligned}
\tag{6.15}
$$

and

$$
\begin{aligned}
M_x &= -\chi_{xx}\lambda_1 L_x P_x + H_x \\
M_y &= -\chi_{yy}\lambda_2 L_x P_y + H_y \\
M_z &= -\chi_{zz}\lambda_3 L_z P_z + H_z
\end{aligned}
\tag{6.16}
$$

Using 6.16 to put in 6.15, we find that there is an <u>induced</u> polarization possible if a magnetic field is applied along a given direction:

$$P_x = \frac{-\kappa_{xx}\lambda_1 L_x}{1 - \kappa_{xx}\chi_{xx}\lambda_1^2 L_x^2} H_x$$

$$P_y = \frac{-\kappa_{yy}\lambda_2 L_x}{1 - \kappa_{yy}\chi_{yy}\lambda_2^2 L_x^2} H_y \qquad (6.17)$$

$$P_z = \frac{-\kappa_{zz}\lambda_3 L_z}{1 - \kappa_{zz}\chi_{zz}\lambda_3^2 L_z^2} H_z$$

From equation 6.17, we can predict the appearance of a finite polarization along the three direction of the crystal under the application of a magnetic field. This induced polarization by a magnetic field is the characteristic of linear magnetoelectricity. We develop a Landau theoretical model where we investigate the couplings of the induced polarization in the multiferroic $LiFeP_2O_7$ system below T_N=22K. Experiments are required to investigate the likely ferroelectric state at RT and study the interplay between polarization and magnetism.

6.3.3 $Sr_2CoSi_2O_7$

Introduction

During the last years, several studies investigated the $3d^2$ transition metal ions in tetrahedral environment [28]. These compounds are particularly interesting for their potential application for infrared Lasers (λ = 1-1.5 μm). In a tetrahedral coordination, the probability of radiative transition of these ions is significantly increased by the absence of crystallographic inversion center. There are several possible approaches in order to stabilize $3d^2$ ions in tetrahedral coordination. The ideal situation would be realized by a structure consisting of only tetrahedra. The melilite family with the general formula $X_2T^1T_2^2O_7$ (X = Na, Ca, Sr or Ba; T^1 = Mg, Co, Fe or Al; T^2 = Al, Si or Ge) is very close to this optimal situation ($T_2^2O_7$ dimers linked between each other by T^1O_4 tetrahedra). These compounds present particularly rich magnetic and structural properties. One of the few magnetic studies which have been carried out in this family concerns the compound $Sr_2CoSi_2O_7$. This compound crystallizes in the non polar space group P-42_1m (n°113). An antiferromagnetic order of the Co^{2+} ions appears below T_N = 7.5 K and is characterized by a magnetic wave-vector $\vec{k}$ = (0,0,0) [29]. Many models for the magnetic structure have been tested. The best model to describe the neutron data measured at 1.5 K consists of an antiferromagnetic ordering with moments along the c crystallographic axis. We

will show that the magnetoelectric effect is allowed in the proposed anti-ferromagnetic model. The crystal and magnetic structures are presented in figure 6.6
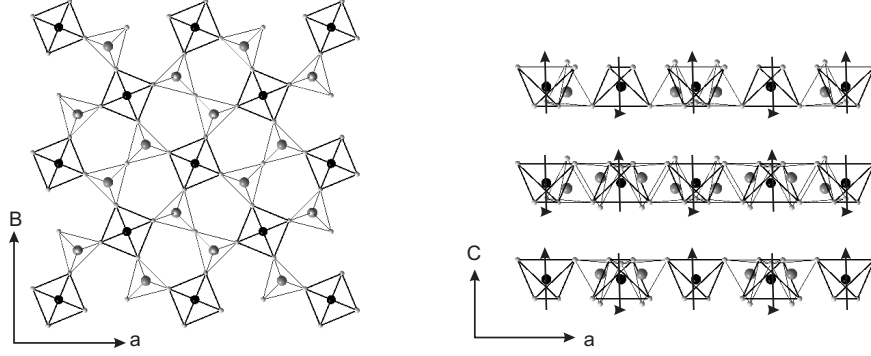

Figure 6.6: *Crystal and magnetic structures of $Sr_2CoSi_2O_7$ in the (a,b) and (a,c) planes. Arrows indicate the magnetic moments on the cobalt atoms (along the c axis). Dark grey atoms represent cobalt atoms linked by tetrahedral dimers of $Si_2O_7^{6+}$. Sr atoms are not represented for sake of clarity.*

Representation analysis of the magnetic structures

There are 2 magnetic atoms Co^{2+} per unit cell occupying the Wyckoff position 2a. There are 2 Co atoms per unit cell at $(0,0,0)$ and at $(1/2,1/2,0)$. As stated previously, below $T_N=7.5K$, the magnetic structure is characterized by $\vec{k}=\vec{0}$. In other words, the magnetic and chemical cells are identical. Consequently, the wave-vector associated with the magnetic structure $\vec{k}=\vec{0}$ has the full point group symmetry of the point group of P-42_1m. The underlying point group is -42m (D_{2d}). Table 6.9 reproduces the characters of this point group.

	E	C_2	$2S_4$	$2C_2'$	$2\sigma_d$
Γ_1	1	1	1	1	1
Γ_2	1	1	1	-1	-1
Γ_3	1	1	-1	1	-1
Γ_4	1	1	-1	-1	1
Γ_5	2	-2	0	0	0

Table 6.9: *Irreducible representations for the space group P-42_1m associated with **k**=0.*

We will first determine the directions of the spins associated with each IR. For that we need to derive the axial and permutational representations

of each symmetry element. The symmetry elements are the following of
$P\text{-}42_1\mathrm{m}$:

$$
\mathbf{1} = \begin{pmatrix} 1 & 0 & 0 & 0 \\ 0 & 1 & 0 & 0 \\ 0 & 0 & 1 & 0 \end{pmatrix}
\quad
-\mathbf{4}^+ = \begin{pmatrix} 0 & 1 & 0 & 0 \\ -1 & 0 & 0 & 0 \\ 0 & 0 & -1 & 0 \end{pmatrix}
$$

$$
\mathbf{2_{1z}} = \begin{pmatrix} -1 & 0 & 0 & 0 \\ 0 & -1 & 0 & 0 \\ 0 & 0 & 1 & 0 \end{pmatrix}
\quad
-\mathbf{4}^- = \begin{pmatrix} 0 & -1 & 0 & 0 \\ 1 & 0 & 0 & 0 \\ 0 & 0 & -1 & 0 \end{pmatrix}
$$

$$
\mathbf{m_{x\bar{y}}} = \begin{pmatrix} 0 & 1 & 0 & 1/2 \\ 1 & 0 & 0 & 1/2 \\ 0 & 0 & 1 & 0 \end{pmatrix}
\quad
\mathbf{2_{1y}} = \begin{pmatrix} -1 & 0 & 0 & 1/2 \\ 0 & 1 & 0 & 1/2 \\ 0 & 0 & -1 & 0 \end{pmatrix}
$$

$$
\mathbf{m_{xy}} = \begin{pmatrix} 0 & -1 & 0 & 1/2 \\ -1 & 0 & 0 & 1/2 \\ 0 & 0 & 1 & 0 \end{pmatrix}
\quad
\mathbf{2_{1x}} = \begin{pmatrix} 1 & 0 & 0 & 1/2 \\ 0 & -1 & 0 & 1/2 \\ 0 & 0 & -1 & 0 \end{pmatrix}
$$

We are dealing here with atoms at $(0,0,0)$(atom 1) and $(1/2,1/2,0)$ (atom
2). Consequently, all the symmetry elements having a non-zero translation
part will send atom 1 on atom 2 and vice-versa. This is not the case for
the other symmetry elements which will not exchange atoms. The permu-
tation representations $\Gamma_{perm}(h_j)$ of half of the different symmetry elements
is common. We have:

$$
\Gamma_{perm}(1) = \Gamma_{perm}(-4^+) = \Gamma_{perm}(2_{1z}) = \Gamma_{perm}(-4^+)
$$
$$
and \quad \Gamma_{perm}(m_{x\bar{y}}) = \Gamma_{perm}(m_{xy}) = \Gamma_{perm}(2_{1x}) = \Gamma_{perm}(2_{1y})
\tag{6.18}
$$

The corresponding expression for the permutation representations $\Gamma_{perm}(h_j)$
is given below:

$$
\Gamma_{perm}(1) = \begin{pmatrix} 1 & 0 \\ 0 & 1 \end{pmatrix}
\qquad and \qquad
\Gamma_{perm}(m_{x\bar{y}}) = \begin{pmatrix} 0 & 1 \\ 1 & 0 \end{pmatrix}
\tag{6.19}
$$

If g_i is a symmetry operation of a crystallographic space group G, we
can describe the action of g_i on a spin vector (axial vector) S_j as:

$$
g_i S_j = \sum_k D_{kj}(g_i) S_k
\tag{6.20}
$$

Here the matrix $D(g_i)$ is the transpose of the transformation matrix of
the spins. The set of matrices $D(g_i)$ of the crystallographic space group G
form a representation Γ of the space group G. Γ of dimension 3n is gener-
ally reducible. After reduction, we can use the technique of the projection

operators in order to determine the basis vectors of the irreducible representations $\Gamma^{(\nu)}$ according to:

$$a^{(\nu)} = d^{-1} \sum_{G_i} \chi^{\Gamma}(G_i)\chi^{(\nu)\star}(G_i) \qquad (6.21)$$

$$\Psi_{ij}^{(\nu)} = \sum_{G_i} D_{ij}^{(\nu)}(G_i)G_i\Psi \qquad (6.22)$$

Applying this approach to our case, we find:

$$\Gamma = \Gamma_1 + \Gamma_2 + 2\Gamma_5$$

One needs now to work out the base vectors of each of these IR's. Using the projector technique, we find the following P_i^j projectors associated to the Γ_i IR:

$$
\begin{aligned}
P^1 &= (\mathbf{1}) + (-\mathbf{4^+}) + (\mathbf{2_{1z}}) + (-\mathbf{4^-}) + (\mathbf{m_{x\bar{y}}}) + (\mathbf{2_{1y}}) + (\mathbf{m_{xy}}) + (\mathbf{2_{1x}}) \\
P^2 &= (\mathbf{1}) + (-\mathbf{4^+}) + (\mathbf{2_{1z}}) + (-\mathbf{4^-}) - (\mathbf{m_{x\bar{y}}}) - (\mathbf{2_{1y}}) - (\mathbf{m_{xy}}) - (\mathbf{2_{1x}}) \\
P_{11}^5 &= (\mathbf{1}) + i(-\mathbf{4^+}) - (\mathbf{2_{1z}}) - (-\mathbf{4^-}) \\
P_{12}^5 &= (\mathbf{m_{x\bar{y}}}) - i(\mathbf{2_{1y}}) - (\mathbf{m_{xy}}) + i(\mathbf{2_{1x}}) \\
P_{21}^5 &= (\mathbf{m_{x\bar{y}}}) + i(\mathbf{2_{1y}}) - (\mathbf{m_{xy}}) - i(\mathbf{2_{1x}}) \\
P_{22}^5 &= (\mathbf{1}) - i(-\mathbf{4^+}) - (\mathbf{2_{1z}}) + i(-\mathbf{4^-})
\end{aligned}
\qquad (6.23)
$$

Applying the projection operators of 6.23, we find the possible different magnetic orders. For the Γ_1 IR, we have an antiferromagnetic ordering with the magnetic components along the c axis. For the Γ_2 IR, we have a ferromagnetic ordering with the magnetic components along the c axis. And finally, the Γ_5 IR describes an antiferromagnetic ordering with the magnetic components in the ab plane. Consequently, we can say that the magnetic ordering appearing under T_N is described by the Γ_1 IR.

Knowing the IR characterizing the magnetic ordering, we need now to find out about the magnetic space group in order to determine if a linear magnetoelectric effect is possible. The space group $P\text{-}42_1\text{m}$ contains 8 symmetry elements. However, it is more convenient to consider only the generators of this space group. We have several possibilities to choose the generators. We chose the simplest ones which are the ones associated with the Hermann-Mauguin symbols: $\text{-}4^+//[001]$, $2_{1x}//[100]$ and $\text{m}//[110]$. Looking at the characters associated to the Γ_1 IR in table 6.9, we can see that the magnetic space group associated to it is $P\text{-}42_1\text{m}$. The associated magnetic point group is thus $\text{-}42_1\text{m}$. Consequently, a linear magnetoelectric effect is allowed with only two non zero components $\alpha_{11} = -\alpha_{22}$. Here, this materials is not multiferroic but simply magnetoelectric.

6.4 Inversion center breaking due to antiferromagnetic ordering

6.4.1 Introduction

Various groups looked for magnetically induced ferroelectrics. The main idea is that antiferromagnetic ordering may break the inversion center of a given structure [13]. Until very recently the magnetically induced ferroelectrics exhibited low polarization values. It has been proposed that the ferroelectric displacements should not rely on the presence of spin orbit coupling alone in order to have a significant polarization [10]. We treat here the case where the inversion center is broken by the antiferromagnetic ordering. We predict a new antiferromagnetic induced ferroelectric due to a non E type antiferromagnetism contrary to the orthorhombic $HoMnO_3$ and in $RNiO_3$ (R = rare-earth) [10].

6.4.2 Cu_2MnSnS_4

Introduction

The title compound has been studied in the search for new dilute magnetic semiconductors (DMS's). Most of the new designed DMS have been based on Mn-II-VI compositions with a zinc-blende or wurtzite crystal structure. However, the main issue in these materials in the light of application is the difficulty to align the Mn spins even with a high magnetic field. In this type of materials, it has been demonstrated that the necessity for a high magnetic field to align the spins is directly related to the amount of Mn in the structure. In order to investigate more in details the relationship between the critical field to align the spins and the structure of recent DMS's, T. Fries and coworkers investigated the magnetic structure of Cu_2MnSnS_4. This compound crystallizes in the space group I-42m (n°121) where only the manganese atoms carry a spin since the copper atoms here are Cu^+ ions. The Mn^{2+} ions occupy the Wyckoff position 2a. This compound presents an antiferromagnetic structure characterized by a propagation wave-vector $\overrightarrow{k}$ = (1/2,0,1/2) below T_N=8.8K. A representation of the magnetic structure is presented in figure 6.7.

Magnetic ordering

The little group of $\overrightarrow{k}$ describing the magnetic structure of Cu_2MnSnS_4 is identical to the one describing the magnetic structure of $LiFeP_2O_7$ (see section 6.3.2). Consequently, we can write a similar expression for the free-energy:
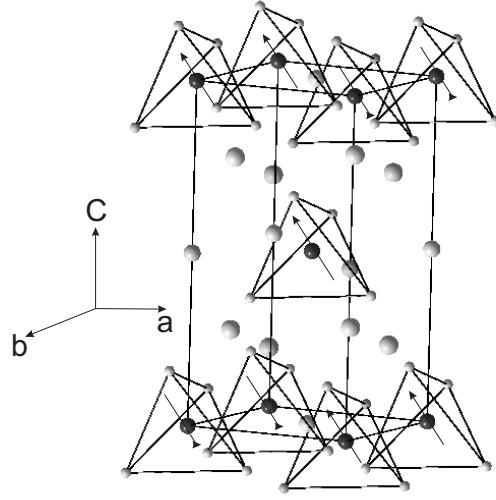
Figure 6.7: *Magnetic structure of Cu_2MnSnS_4 in the (a,c) plane. Arrows indicate the magnetic moments on the manganese atoms.*

$$
\begin{aligned}
F = F_0 &+ \frac{a}{2}L^2 + \frac{b}{4}L^4 + \frac{c}{2}M^2 + \frac{d}{4}M^4 \\
&+ \frac{1}{2}\sum_{i=x,y,z}(\nu_i L_i^2 + \beta_i M_i^2) \\
&+ \delta L_x L_z + \gamma M_x M_z \\
&+ \sigma_1 L_x M_y + \sigma_2 L_z M_y + \sigma_3 L_y M_z + \sigma_5 L_y M_x
\end{aligned}
\tag{6.24}
$$

We will not discuss here the free-energy and the different magnetic symmetries since there are the same as for $LiFeP_2O_7$. Experimentally, it has been observed that the structure orders magnetically in the magnetic structure described by 2 antiferromagnetic components (L_x and L_z). The magnetic ordering is described by the magnetic space group $P2_1$.

Magnetic ordering induces polarization

We will have a look at the possible breaking of the inversion center. In other words, can we have appearance of spontaneous polarization while the compound orders magnetically? In order to determine the extra terms susceptible to appear, we investigated the transformation properties of the different magnetic components. We present the results in table 6.10.

From table 6.10, we notice an interesting term $L_x L_z P_y$. Consequently, we can write a simplified expression for the free energy including this new term:

	h_1	h_2	Rh_1	Rh_2
L_x	1	1	-1	-1
L_y	1	-1	-1	1
L_z	1	1	-1	-1
M_x	1	-1	-1	1
M_y	1	1	-1	-1
M_z	1	-1	-1	1
P_x	1	-1	1	-1
P_y	1	1	1	1
P_z	1	-1	1	-1

Table 6.10: *Transformation properties of the components of the different vectors of interest for the magnetic space group I-42m associated to* **k**=(1/2, 0, 1/2).

$$
\begin{aligned}
F = & F_0 + \frac{a}{2}L^2 + \frac{b}{4}L^4 + \frac{\alpha}{2}P^2 \\
& + \beta L_x L_z P_y + \frac{1}{2}\sum_{i=x,y,z}\nu_i L_i^2
\end{aligned}
\tag{6.25}
$$

If we minimize 6.25, we find:

$$
\begin{aligned}
\frac{\partial F}{\partial L_x} &= aL_x + bL_x^3 + \beta L_z P_y + \nu_x L_x \\
\frac{\partial F}{\partial L_y} &= aL_y + bL_y^3 + \nu_y L_y \\
\frac{\partial F}{\partial L_z} &= aL_z + bL_z^3 + \beta L_x P_y + \nu_z L_z \\
\frac{\partial F}{\partial P_x} &= \alpha P_x \\
\frac{\partial F}{\partial P_y} &= \alpha P_y + \beta L_x L_z \\
\frac{\partial F}{\partial P_z} &= \alpha P_z
\end{aligned}
\tag{6.26}
$$

From 6.26, we can find two series of equalities:

$$P_x = P_z = 0$$

$$P_y = -\frac{\beta}{\alpha} L_x L_z$$

$$L_x = 0 \quad or \quad L_x = \frac{-(a + \nu_x + \frac{\beta^2}{\alpha} L_z^2)}{b}$$

$$L_y = 0 \quad or \quad L_y = \frac{-(a + \nu_y)}{b} \tag{6.27}$$

$$L_z = 0 \quad or \quad L_z = \frac{-(a + \nu_z + \frac{\beta^2}{\alpha} L_x^2)}{b}$$

Consequently, we have different magnetic ordering patterns possible. However, from experiment we know that we have the situation $(L_x, L_z) \neq (0,0)$. Above T_N, we have $L_x = L_z = 0$ and consequently $P_y = 0$. However, below T_N, we have (replacing the expression of L_x in L_z and vice-versa):

$$L_x = \frac{-\alpha(ab\alpha^2 + a\beta^2 + \beta^2\nu_z + \alpha\beta\nu_x)}{\alpha^2 b^2 - \beta^4}$$

$$L_z = \frac{-\alpha(ab\alpha^2 + a\beta^2 + \beta^2\nu_x + \alpha\beta\nu_z)}{\alpha^2 b^2 - \beta^4} \tag{6.28}$$

Using 6.28 to put in 6.27, we find that there is a spontaneous polarization possible while going in the magnetic ordered state:

$$P_y = -\frac{\beta}{\alpha} L_x L_z$$

$$= -\frac{\beta}{\alpha} \times \frac{-\alpha(ab\alpha^2 + a\beta^2 + \beta^2\nu_z + \alpha\beta\nu_x)}{\alpha^2 b^2 - \beta^4} \tag{6.29}$$

$$\times \frac{-\alpha(ab\alpha^2 + a\beta^2 + \beta^2\nu_x + \alpha\beta\nu_z)}{\alpha^2 b^2 - \beta^4}$$

If we assume that the relativistic components ν_j have a negligible effect on the value of the spontaneous polarization, we can rewrite 6.29 as:

$$P_y \simeq -a^2 \alpha\beta \frac{(b\alpha^2 + \beta^2)^2}{(\alpha^2 b^2 - \beta^4)^2} \tag{6.30}$$

From 6.30, we see that the *spontaneous* polarization appearing below T_N is proportional to a^2. This is the first time to our knowledge that a non-oxide material exhibits such property.

Magnetoelectric properties

We have been describing in the previous section, the spontaneous polarization susceptible to arise going trough the antiferromagnetic ordering. However, this is not the only polarization possible. We have to deal here with the same point group than in the case of LiFeP$_2$O$_7$ (see section 6.5). Consequently, under the application of a magnetic field, we will have the following polarization components which will appear:

$$
\begin{aligned}
P_x &= \frac{-\kappa_{xx}\lambda_1 L_x}{1 - \kappa_{xx}\chi_{xx}\lambda_1^2 L_x^2} H_x \\
P_y &= \frac{-\kappa_{yy}\lambda_2 L_x}{1 - \kappa_{yy}\chi_{yy}\lambda_2^2 L_x^2} H_y \\
P_z &= \frac{-\kappa_{zz}\lambda_3 L_z}{1 - \kappa_{zz}\chi_{zz}\lambda_3^2 L_z^2} H_z
\end{aligned}
\tag{6.31}
$$

From 6.31, we can predict the appearance of some polarization along the three direction of the crystal under the application of a magnetic field. This *induced* polarization by a magnetic field is the characteristic of magnetoelectricity. However, here we have to deal with a structure giving rise to some spontaneous polarization along y under T$_N$. Consequently, we will have an increase of this polarization under magnetic field by an amount of:

$$
\begin{aligned}
\Delta P_y &= -\frac{\beta}{\alpha} \times \frac{-\alpha(ab\alpha^2 + a\beta^2 + \beta^2\nu_z + \alpha\beta\nu_x)}{\alpha^2 b^2 - \beta^4} \\
&\times \frac{-\alpha(ab\alpha^2 + a\beta^2 + \beta^2\nu_x + \alpha\beta\nu_z)}{\alpha^2 b^2 - \beta^4} \\
&- \frac{-\kappa_{yy}\lambda_2 L_x}{1 - \kappa_{yy}\chi_{yy}\lambda_2^2 L_x^2} H_y \\
&\simeq -a^2\alpha\beta \frac{(b\alpha^2 + \beta^2)^2}{(\alpha^2 b^2 - \beta^4)^2} - \frac{-\kappa_{yy}\lambda_2 L_x}{1 - \kappa_{yy}\chi_{yy}\lambda_2^2 L_x^2} H_y
\end{aligned}
\tag{6.32}
$$

We show using Landau and group theory that Cu$_2$MnSnS$_4$ can be considered as a new magnetically induced ferroelectric. In addition to a spontaneous polarization, we show that a linear magnetoelectric effect is allowed. Moreover, the ferroelectric displacements are not expected to rely on the presence of spin-orbit coupling. Consequently, the polarization should be quite strong as in the predicted orthorhombic HoMnO$_3$ and in RNiO$_3$ [10]. Contrary to these compounds, the polarization should be tunable by electric and magnetic fields.

References

[1] M. Fiebig, J. Phys. D: Appl. Phys. **38** R123 (2005)

[2] W. Eerenstein, N. D. Mathur and J. F. Scott, Nature **442** 759 (2006)

[3] S.-W. Cheong and M. Mostovoy, Nature Materials **6**, 13 (2007)

[4] The Landau Theory of Phase Transitions, J.-C. Tolédano and P. Tolédano; World Scientific Publishing 1987

[5] A. B. Harris, unpublished, cond-mat/0610241)

[6] H. Katsura, N. Nagaosa and A. V. Balatsky, Phys. Rev. Lett. **95**, 057205 2005)

[7] I.A. Sergienko and E. Dagotto, Phys. Rev. B **73**, 094434 (2006)

[8] M. Mostovoy, Phys. Rev. Lett. **96**, 067601 (2006)

[9] M. Date, J. Kanamori and Y. Tachiki, J. Phys. Soc. Jpn. **16**, 2589 (1961)

[10] I. A. Sergienko, C. Sen and E. Dagotto, unpublished cond-mat/0608025

[11] G. R. Blake *et al.*, Phys. Rev. B **71**, 214402 (2005); L. C. Chapon *et al.* Phys. Rev. Lett. **93**, 177402; N. Aliouane *et al.* Phys. Rev. B **73**, 20102 (2006); T. Goto *et al.* Phys. Rev. B **72**, 220403 (2005); T. Kimura *et al.*, Nature **426**, 55 (2003); N. Hur *et al.* **429**, 392 (2004)

[12] I. E. Dzialoshinskii, Sov. Phys. JETP, **10**, 628 (1960)

[13] S. Goshen, D. Mukamel, H. Shaked and S. Shtrikman, J. Appl. Phys. **40**, 1590 (1969); S. Goshen, D. Mukamel, H. Shaked and S. Shtrikman, Phys. Rev. B **12**, 4679 (1970)

[14] G. Toulouse, Commun. Phys. **2**, 115 (1977)

[15] G. Ferey, M. Leblanc, R. de Pape and J. Pannetier, Inorganic Solid Fluorides, ed. P. Hagenmülller (Academic Press, New York, London, (1985) p. 395; M. Leblanc, G. Ferey, R. de Pape and J. Pannetier, Solid State Commun. **58** (1986) 171.; M. Leblanc, G. Ferey, Y. Calage and R. de Pape, J. Solid State Chem. **53** (1984) 360; Y. Laligant, M. Leblanc, J. Pannetier and G. Ferey, J. Phys.C **19** (1986) 1081; G. Ferey, R. de Pape and B. Boucher, Acta Cryst. B **34** (1978) 1084; G. Ferey, M. Leblanc, R. de Pape and J. Pannetier, Solid State Commun. **53** (1985) 559; G. Ferey, R. de Pape, M. Leblanc and J. Pannetier, Rev. Chim. Min. **23** (1986) 294; P. Lacorre, J. Pannetier and G. Ferey, J. Magn. Magn. Mat. **66** (1987) 213; H. Kawamura and S. Miyashita, J. Phys. Soc. Japan **53** (1984) 9; D.H. Lee, J.D. Joannopoulos and J.W. Negele, Phys. Rev. B **33** (1986) 450; S. Katsura, T. Ide and T. Morita, J.

Stat. Phys. **42** 381 (1986) ; S.E. Korshunov and GN. Uimin, J. Stat. Phys. **43** (1986) 1

[16] D. Kissel, R. Hoppe, Z.Natur. Teil B, Anorg. Chemie, Org. Chemie **42**, 135 (1987)

[17] P. Lacorre, M. Leblanc, J. Pannetier, G. Ferey, J. Magn. Magn. Mat. **94**, 337 (1991); P. Lacorre, M. Leblanc, J. Pannetier, G. Ferey, J. Magn. Magn. Mat. **66** (1987) 219-224

[18] P. Lacorre, J. Pannetier, G. Ferey, J. Magn. Magn. Mat. **94**, 331 (1991)

[19] M. C. Foster, G. R. Brown, R. M. Nielson, S. C. Abrahams, J. Appl. Cryst. **30**, 495 (1997); G. C. Miles, M. C. Stennett, D. Pickthall, C. A. Kirk, I. M. Reaney and A. R. West, Powder Diffraction **20**, 43 (2005); L. E. Cross and R. R. Neurgaonkar, J. Mat. Science **27**, 2589 (1992)

[20] E. F. Bertaut, Acta Cryst. A **24**, 217 (1968)

[21] P. Lacorre, J. Pannetier, G. Ferey, J. Magn. Magn. Mat. **66**, 213 (1987)

[22] J. Renaudin, G. Ferey, A. Kozak, M. Samouel, P. Lacorre, Solid State Commun. **65**, 185 (1988)

[23] P. Lacorre, J. Pannetier, T. Fleischer, R. Hoppe, G. Ferey, J. Solid State Chem. **93**, 37 (1991)

[24] J. Hernández-Velasco, R. Sáez-Puche, A. Hoser, J. Rodríguez-Carvajal, Physica B **276-278**, 726 (2000)

[25] A. S. Wills, Physica B **276**, 680 (2000), program available from ftp://ftp.ill.fr/pub/dif/sarah/

[26] P. G. Radaelli, L. C. Chapon; unpublished cond-mat/0609087 and L. C. Chapon, P. G. Radaelli, Y. S. Her, M. T. F. Telling, J. F. Mitchell, unpublished cond-mat/0608031

[27] G. Rousse, J. Rodríguez-Carvajal, C. Wurm, C. Masquelier, Solid State Sciences **4**, 973 (2002)

[28] M. A. Scott, T. P. J. Han, H. G. Gallagher, B. Henderson, J. of Luminescence, **72-74** 260-262 (1997).

[29] Strontium-Kobalt-Åkermanit $Sr_2CoSi_2O_7$ Materialsynthese, Kristallzchtung, Magnetismus ; Diplomarbeit, Gabriele Römer-Scheuermann aus Büdingen, Marburg, August 2001.

Appendix A

Symmetry-adapted mode analysis

The structural distortion relating the two phases in a structural phase transition can be in general decomposed into a homogeneous strain and an atomic-displacement field, $\mathbf{u}_\alpha(l, \kappa)$, representing the displacement of each atom (l,κ) in the low-symmetry structure, where l represents a unit cell of the high symmetry structure, κ an atomic label within the corresponding unit cell and α stands for the three dependent components (say x, y, z). The displacement field $\mathbf{u}_\alpha(l, \kappa)$ is calculated from the substraction of the atomic positions of the two structures, each expressed in relative units.

Using the results of group theory, it has been shown that it is possible to consider a decomposition of the total distortion in terms of components with different isotropy space groups [1]:

$$\mathbf{u}_\alpha(l, \kappa) = \sum_Z \sum_i C^Z(i) \xi_\alpha^Z(\kappa, l|i) \qquad \text{(A.1)}$$

The first sum in A.1 is over all the possible space-groups $\mathbf{Z}$, such that $\mathbf{G} \geq \mathbf{Z} \geq \mathbf{H}$ where $\mathbf{G}$ is the high symmetry structure and $\mathbf{H}$ the low symmetry. The $\xi_\alpha^{\mathbf{H}}(\kappa, l|j)$ are called the chain-adapted symmetry Z modes. $\xi_\alpha^Z(\kappa, l|j)$ depends on the Wyckoff position. However in most cases, equation A.1 can be reduced to the following expression:

$$\mathbf{u}_\alpha^0(l, \kappa) = \sum_j C^{\mathbf{H}}(j) \xi_\alpha^{\mathbf{H}}(\kappa, l|j) \qquad \text{(A.2)}$$

The expressions $\xi_\alpha^Z(\kappa, l|i)$ can be obtained from the splitting of the Wyckoff positions in the transition $\mathbf{G} \rightarrow \mathbf{H}$ (for a method see ref. [1]).

Once we obtain the different $\mathbf{u}_\alpha^0(l, \kappa)$ values along the different directions, we need to do an optimization of the origin for comparing the structures in symmetry $\mathbf{H}$ and $\mathbf{G}$. This is due to the fact that the choice of origin in the ferroelectric structure is arbitrary. Once we have derived the displacements of the different atoms within the structure based on the method proposed in [1] and with the help of the program SYMMODES [2], we have to consider

them as dependent on the origin choice. A displacement of this origin along one particular direction by a vector $\mathbf{u}_0$ with respect to the one used for the calculation of the displacements will change these displacements in the form:

$$\mathbf{u}_\alpha^0(l,\kappa)_{new} = \mathbf{u}_\alpha^0(l,\kappa) - \mathbf{u}_0 \qquad (A.3)$$

We have in general to choose $\mathbf{u}_0$ such that the displacements fulfill some reasonable criterion. We chose that all $m_i \times \mathbf{u}_\alpha^0(l,\kappa)_{new}=0$ where m_i is the mass of the different atoms in order to keep the center of mass unchanged.

[1] M. I. Aroyo and J. M. Perez-Mato, Acta Cryst. A (1998) **54**, 19-30

[2] C. Capillas, E. Kroumova, M. I. Aroyo, J. M. Perez-Mato, H. T. Stokes and D. M. Hatch, J. Appl. Cryst. **36** 953 (2003).

Summary

Transition metal oxides can exhibit a wide variety of properties which can be tuned by changing factors such as composition, magnetic field and temperature. The complex physical phenomena involved can give rise to functional materials such as magnetic field sensors or ferroelectrics. The discovery of new functional materials is a challenge for the development of smart systems. To guide this search, a clear understanding of the relationship between the physical properties and the atomic scale structure of the materials is needed. Of fundamental importance is the crystal chemistry of a given compound. Crystal chemistry refers to two aspects: symmetry and the distribution of atoms in the unit cell.

The crystal chemistry can be investigated by means of synchrotron X-ray and neutron diffraction. These techniques provide information that can be used as a starting point for a better understanding of the physical properties. The physical properties are directly related to the symmetry exhibited by the system. Thus the symmetry is an important tool to investigate materials of interest.

Chapter 1 discusses the richness of the transition metal oxides. We describe the general points of interest which have motivated our work. This thesis concentrates on two topics: orbital ordering and multiferroic / magnetoelectric materials.

In **chapter 2**, we describe the various techniques that we have used in order to investigate our materials. We take a dual approach throughout this thesis involving a combination of experimental and theoretical studies. In the first part of the chapter, we describe the main characteristics of the different techniques or equipment that we have used. In the second part, we present the main principles and techniques of group theory which enable us to make predictions about the materials under investigation.

Chapter 3 describes our work on possible orbital ordering in rare-earth titanates. We investigated the temperature dependence of the crystal structure with synchrotron radiation using crushed single crystals of $YTiO_3$ and $LaTiO_3$. We show that the crystal structure of both compounds, contrary to previous reports do not present any structural signature of a cooperative Jahn-Teller effect. Using symmetry arguments, we show that the crystal field resulting from the La ion shift does not have D_{3d} character. This D_{3d}

character was previously invoked in order to explain the distorted perovskite structure exhibited by $RTiO_3$. In addition, we show that the previously reported low magnetic moment of $LaTiO_3$ can be interpreted as the result of phenomena that do not involve an orbital ordering scheme.

In **chapter 4**, we describe a detailed investigation of the structural properties of $YMnO_3$, which is one of the most studied multiferroic materials, as a function of temperature. We grew a single crystal of $YMnO_3$ using the floating zone technique. Prior to carrying out experiments, we investigated theoretically using Landau and group theories the possible different phases and the nature of the possible phase transitions. We provide insight into the possible mechanism that gives rise to ferrielectricity using neutron and synchrotron diffraction on single crystal and powder samples. We show that an intermediate phase exists between a high temperature paraelectric phase and a room temperature ferrielectric phase. This phase is stable between two critical temperatures T_{C1} and T_{C2} and our data suggest that it is polar. The intermediate phase is characterized by competition between a ferroelectric and a ferrielectric state which is finally stabilized below T_{C1}. This interpretation provides a different explanation of the ferrielectricity in this compound to that previously assumed.

Chapter 5 deals with the experimental investigation of the interplay between magnetic and dielectric properties of multiferroic and magnetoelectric materials. In the first part, we investigat the magnetocapacitive response of an organic-inorganic hybrid. We show that below the Néel temperature T_N, the magnetodielectric coupling is enhanced by almost one order of magnitude. We can explain the decrease of the dielectric constant and the quadratic field dependence below and above T_N using a Landau approach. In the second part of the chapter, we predict a linear magnetoelectric effect in Ho_2BaNiO_5. This prediction based on symmetry arguments motivated us to performed pyroelectric current measurements on a pellet sample. We show that this system exhibits a linear magnetoelectric effect which is sensitive to the low dimensionality of the magnetic structure.

Finally, **in chapter 6**, using group theory and Landau theory we predict several new magnetoelectric and multiferroic materials. We aim to illustrate the power of symmetry analysis in the search for new compounds of interest for technological applications.

Samenvatting

Overgangsmetaaloxides vertonen diverse eigenschappen die bepaald worden door materiaalsamenstelling, magnetisch veld, temperatuur, etc. De complexe fysische verschijnselen die hierbij een rol spelen, leveren vele nuttige materialen zoals een magnetisch veld sensor of ferro-elektricum.

De zoektocht naar nieuwe functionele materialen is een uitdaging in de ontwikkeling van slimme systemen. Om aan deze zoektocht richting te geven, is een helder inzicht in het verband tussen de fysische eigenschappen en de structuur op atomaire schaal noodzakelijk. De kristalchemie van een bepaalde stof is hierbij van fundamenteel belang. De kristalchemie heeft betrekking op twee aspecten: symmetrie en de ruimtelijke verdeling van atomen in de eenheidscel.

De kristalchemie kan in kaart worden gebracht door middel van synchroton Röntgenstraling en neutronen diffractie. Dit verschaft informatie die als basis dient voor een beter begrip van de fysische eigenschappen. De fysische eigenschappen hangen nauw samen met de symmetrie die het systeem vertoont. De symmetrie is daarom een belangrijk hulpmiddel in het onderzoek naar verschillende materialen.

Hoofdstuk 1 behandelt de rijkdom van overgangsmetaal oxides. We beschrijven de belangrijkste algemene punten die als stimulans hebben gediend voor ons werk. Dit proefschrift verdiept zich in een tweetal aspecten: orbitaal ordening en multiferroische / magneto-elektrische materialen.

In hoofdstuk 2 reiken we de verschillende technieken aan die we hebben toegepast om onze materialen te bestuderen. We hebben besloten om in dit proefschrift een tweeledige benadering te nemen: een experimentele benadering naast een theoretische benadering. In het eerste gedeelte van het hoofdstuk beschrijven we de hoofdkenmerken van de verschillende technieken en gereedschappen die we hebben toegepast. In het tweede gedeelte recapituleren we de belangrijkste principes en technieken van groepentheorie die ons in staat stellen voorspellingen te doen over de materialen die onderzocht worden.

Hoofdstuk 3 beschrijft het onderzoek naar mogelijke orbitaal ordening in zeldzame aard titanaten. We hebben de kristalstructuur van verpoederde nkristallen van $YTiO_3$ en $LaTiO_3$ bij verschillende temperaturen onderzocht met behulp van synchrotronstraling. We tonen aan dat, in tegen-

stelling tot eerder gerapporteerd onderzoek, de kristalstructuur van beide stoffen geen kenmerk van een coperatief Jahn-Teller effect vertoont. Door gebruik te maken van symmetrie argumenten leveren we het bewijs dat het kristalveld, dat voortkomt uit de La verschuiving, geen D_{3d} karakter heeft. We gebruiken dit D_{3d} karakter om het vervormde karakter van de perovskiet structuur van $RTiO_3$ te verklaren. Bovendien leveren we het bewijs dat het eerder gerapporteerde kleine magnetisch moment van $LaTiO_3$ verklaard kan worden als het netto resultaat van verschillende fenomenen die niets te maken hebben met orbitaal ordening.

In hoofdstuk 4 hebben we in detail de structuur eigenschappen van $YMnO_3$, een van de meest bestudeerde multiferroische materialen, bij hoge temperaturen bestudeerd. Daartoe hebben we een nkristal van $YMnO_3$ gegroeid met behulp van een spiegeloven. Voordat een experiment werd uitgevoerd, hebben we langs theoretische weg de mogelijke verschillende fasen en ook het karakter van de faseovergangen onderzocht. We verschaffen inzicht in het mogelijke mechanisme achter ferri-elektriciteit door gebruik te maken van neutron- en synchrotonstraling op nkristal en poedermonsters. We beschrijven het bestaan van een tussenfase die grenst aan de hoge temperatuur para-elektrische fase en de kamertemperatuur ferri-elektrische fase. Deze fase is stabiel tussen T_{C1} en T_{C2}. We laten zien aan de hand van onze meetgegevens dat dit een polaire tussenfase is. Deze tussenfase wordt gekenmerkt door een competitie tussen een ferro-elektrische en een ferri-elektrische toestand die uiteindelijk stabiliseert onder T_{C1}. Deze interpretatie betekent dat deze ferri-elektriciteit door een nieuw mechanisme uitgelegd moet worden.

In Hoofdstuk 5 komt experimenteel onderzoek naar de wisselwerking tussen magnetische en dilektrische eigenschappen van multiferroische en magneto-elektrische materialen aan de orde. In het eerste gedeelte hebben we de magnetocapacitieve respons van een organisch-anorganisch hybride materiaal onderzocht. We tonen aan dat de magneto dilektrische koppeling beneden de Néel temperatuur T_N vergroot is met bijna een factor tien. We kunnen met behulp van de Landau benadering deze afname in dilektrische constante en de kwadratische afhankelijkheid met het aangelegde veld zowel boven als onder T_N verklaren. In het tweede deel van het hoofdstuk voorspellen we een lineair magneto-elektrisch effect in Ho_2BaNiO_5. Deze voorspelling is gebaseerd op symmetrie argumenten en heeft ons aangezet pyroelektrische stroom metingen te verrichten. Dit effect is gevoelig voor de lage dimensionaliteit van de magnetische structuur.

Tot slot voorspellen we in Hoofdstuk 6 gebruik makend van groepentheorie en Landau theorie verschillende magneto-elektrische en multiferroische materialen. We hebben ons ten doel gesteld de kracht van symmetrie analyse tot uitdrukking te brengen in een zoektocht naar nieuwe materialen die interessant kunnen zijn voor technologische toepassingen.

Acknowledgements

Many measurements would not have been possible without the work of Umut and Mufti. I am very thankful to them not only for their technical support but also for all our scientific and non-scientific conversations. It was great to work and interact with both of you and I hope that we will continue in a more systematic way. I am thankful also to Johan for translating the summary in Dutch. Graeme, your contribution with the English has been highly appreciated. But more importantly, I have learned a lot from you through our collaboration on $YMnO_3$ concerning data refinements and those dirty tricks concerning GSAS which could greatly facilitate my life. Thank you very much for all of that.

I would like to thank the little French and the big Romanian mafias for sharing many good moments. I am grateful to Malia, Galice, Michaël, Christophe and Claire for tarot evenings, support and having fun on a daily basis. Ajay, I will keep very good memories of our shared moments, especially when you were cooking! Many thanks also go to the Romanian mafia which is too big to mention everyone. I will not forget the parties, some particular week-ends, salată de vinete of Dana, pălinca of Dana and Alex and all my stays in Romania. Mulţumesc frumos pentru tot.

Draga mea Dulcica, îti mulţumesc pentru tot sprijinul şi dragostea pe care mi le-ai acordat. Încrederea pe care ai avut-o in mine in momentele de cumpănă m-a ajutat sa merg mai departe şi a facut să dispară toate îndoielile. Alături de tine, viaţa devine mai frumosă pe zi ce trece.